

N O T I C E

THIS DOCUMENT HAS BEEN REPRODUCED FROM
MICROFICHE. ALTHOUGH IT IS RECOGNIZED THAT
CERTAIN PORTIONS ARE ILLEGIBLE, IT IS BEING RELEASED
IN THE INTEREST OF MAKING AVAILABLE AS MUCH
INFORMATION AS POSSIBLE

(NASA-CR-164952) AIRCRAFT WING
TRAILING-EDGE NOISE (North Carolina State
Univ.) 145 p HC A07/MF A01 CSCL 01A

N82-11039

Unclassified
G3/02 01975

Center For Sound and Vibration



Department of Mechanical and Aerospace Engineering
North Carolina State University
Raleigh, North Carolina

AIRCRAFT WING TRAILING-EDGE NOISE

by

RONALD L. UNDERWOOD

THOMAS H. HODGSON

DEPARTMENT OF MECHANICAL AND AEROSPACE ENGINEERING

Center for Sound and Vibration

Raleigh

1981

ABSTRACT

Aerodynamic noise generation at the trailing-edge of an airfoil is investigated. The mechanism and sound pressure level of the trailing-edge noise for two-dimensional turbulent boundary layer flow is examined. Experiment is compared with current theory.

A NACA 0012 airfoil of 0.61 m chord and 0.46 m span was immersed in the laminar flow of a low turbulence open jet. A 2.54 cm width roughness strip was placed at 15% chord from the leading edge on both sides of the airfoil as a boundary layer "trip" so that two separate but statistically equivalent turbulent boundary layers were formed. Tests were performed with several trailing-edge geometries with the upstream velocity U_∞ ranging from a value of 30.9 m/s up to 73.4 m/s.

The mean-square sound pressure level of the trailing-edge noise was found to follow the convection velocity V to the 4.97 power, which closely follows the theoretical prediction of a 5.0 power. When scaled to full-size, two-dimensional trailing-edge noise was found to be some 15-20 dB below measured sound levels for large-bodied jumbo-jet aircraft in the aerodynamically "clean" configuration. This lower sound level for the trailing-edge noise is shown to be in agreement with trailing-edge noise theory applying the mathematical "Kutta" condition.

Properties of the boundary layer for the airfoil and pressure fluctuations in the vicinity of the trailing-edge are examined. A scattered pressure field due to the presence of the trailing-edge is observed and is suggested as a possible sound producing mechanism for the trailing-edge noise.

BIOGRAPHY

Ronald Lynn Underwood was born in Sanford, N. C., on May 31, 1956. He was reared near Sanford in Lee County and graduated from Broadway High School in 1974.

In August 1974 the author enrolled as a full-time student at North Carolina State University at Raleigh. He received a Bachelor of Science degree with a major in Physics in May 1978.

The author subsequently enrolled as a full-time graduate level student in the Department of Mechanical Engineering at North Carolina State University. His studies were concentrated on acoustics and vibrations.

The author is married to the former Pamela Christine Currin. Mrs. Underwood graduated from East Carolina University in May 1978 with a Bachelor of Science degree in Nursing.

ACKNOWLEDGEMENTS

The author wishes to express his appreciation and thanks to the many people who have contributed to the completion of his graduate studies at North Carolina State University and have made his stay most enjoyable. He would like to extend special thanks and his deepest admiration to Dr. Thomas H. Hodgson, his Advisory Committee Chairman and mentor. Sincere appreciation and gratitude are also extended to the other members of his Advisory Committee: Dr. Franklin D. Hart and Dr. J. A. Marlin. Very special thanks are extended to Dr. Thomas F. Brooks at NASA Langley, Hampton, Virginia, who has been most helpful in providing the materials and financing for this study under NASA Contract No. GI377 and to Mr. Mark B. Manley for his invaluable stimulating and enlightening discussions covering the broad spectrum of academic subjects.

Finally, the author wishes to express his deepest gratitude and appreciation to his wife Pamela Currin Underwood and to his parents Jacob Afton Underwood and Mary Smith Underwood for their constant support and encouragement.

TABLE OF CONTENTS

	Page
LIST OF TABLES	vi
LIST OF FIGURES.	vii
LIST OF SYMBOLS.	xiv
1. GENERAL INTRODUCTION.	1
2. THEORY.	3
2.1 Introduction	3
2.2 Physical View of the Trailing-edge Noise Phenomenon	6
2.3 The Formulation of Ffowcs Williams and Hall.	9
2.4 Alternative Formulations	16
2.5 Green's Functions Used in Various Formulations of the Trailing-edge Noise Problem	20
2.6 The Kutta Condition.	22
3. EXPERIMENTAL DESCRIPTION	27
4. BOUNDARY LAYER MEASUREMENTS AND RESULTS	34
4.1 Boundary Layer Rake Measurements	34
4.2 Boundary Layer Preston Tube Measurements	40
4.3 Comparison of the Mean-pressure Distribution Around the Airfoil with Previous Data.	42
5. THE ACOUSTIC FARFIELD AND SOUND POWER LAW	46
5.1 Farfield Spectrum and Phase and the Power Law.	46
5.2 The Effect of the Kutta Condition Result on the Absolute Level of the Mean-square Sound Pressure	53
5.3 Scaling.	56
5.4 Directivity.	62
6. THE SURFACE PRESSURE FIELD.	67
6.1 Spectrum of the Surface Pressure Field	67
6.2 Phase of the Surface Pressures at the Trailing-edge.	71
6.3 The Scattered Pressure Field	74
7. WAKE CONVECTION SPEED AND COMPARISON WITH THEORY.	78

	Page
8. DISCUSSION OF THE "CAUSALITY" APPROACH TO SOURCE IDENTIFICATION	81
9. CONCLUSIONS.	83
10. LIST OF REFERENCES	86
11. APPENDICES	88
11.1 Results of Boundary Layer Rake Measurements.	88
11.2 Results of Boundary Layer Preston Tube Measurements	113
11.3 Sound Power Law for a 0.9525 cm Diameter Rod	126

LIST OF TABLES

	Page
Table 4.1 Boundary layer parameters for the NACA 0012 airfoil at 0° angle-of-attack from boundary layer rake measurements at 0.238 cm from trailing-edge and 2.54 cm from airfoil centerline	39
Table 4.2 Boundary layer parameters for the NACA 0012 airfoil at 0° angle-of-attack obtained from Preston tube measurements at 0.238 cm from the trailing-edge on the airfoil centerline.	41
Table 11.1 Boundary layer parameters for the NACA 0012 airfoil at 0° angle-of-attack from boundary layer rake measurements at 0.238 cm from trailing-edge and 2.54 cm from airfoil centerline	89
Table 11.2 Boundary layer parameters for the NACA 0012 airfoil at 5° angle-of-attack from boundary layer rake measurements at 0.238 cm from trailing-edge and 2.54 cm from airfoil centerline	97
Table 11.3 Boundary layer parameters for the NACA 0012 airfoil at 10° angle-of-attack from boundary layer rake measurements at 0.238 cm from trailing-edge and 2.54 cm from airfoil centerline	105
Table 11.4 Boundary line parameters for the NACA 0012 airfoil at 0° angle-of-attack obtained from Preston tube measurements at 0.238 cm from the trailing-edge on the airfoil centerline.	114
Table 11.5 Boundary layer parameters for the NACA 0012 airfoil at 0° angle-of-attack obtained from Preston tube measurements at 2.54 cm from the trailing-edge on the airfoil centerline.	118
Table 11.6 Boundary layer parameters for the NACA 0012 airfoil at 0° angle-of-attack obtained from Preston tube measurements at 22.86 cm from the trailing-edge on the airfoil centerline.	122

LIST OF FIGURES

	Page	
Figure 2.1	Trailing-edge noise problem (a) modeled physically as the interaction of low Mach-number two-dimensional turbulent flow with the edge of a semi-infinite thin rigid plate (b).	4
Figure 2.2	Trailing-edge noise model.	5
Figure 2.3	(after Howe ¹⁶) Observer coordinates R , $\bar{\theta}$, and α shown in relation to the plate and a rectangular coordinate system.	7
Figure 2.4	(after Howe ¹⁶) Illustration of the angle β between the flow velocity V and an extension (x_1) to the half-plane	7
Figure 2.5	The $\sin^2(\bar{\theta}/2)$ directivity pattern predicted for the mean-square sound pressure variation with observer angle $\bar{\theta}$	8
Figure 2.6	Plate reflections.	10
Figure 2.7	The semi-infinite plate model.	11
Figure 2.8	Physical interpretation of equations 2.3 and 2.4.	14
Figure 2.9	(after Ffowcs Williams and Hall ⁸) Geometry for the McDonald ¹⁹ Green's function for a semi-infinite plane.	15
Figure 2.10	An eddy is seen to radiate strongly as it is altered or "scattered" by the edge of a semi-infinite plate.	19
Figure 2.11	(after Howe ¹⁰) The Kutta condition	24
Figure 2.12	Eddy-edge interaction.	26
Figure 3.1	The basic microphone and airfoil geometry and the trailing-edge Kulite placement	28
Figure 3.2	Trailing-edge geometries used in the experiment	30

	Page
Figure 3.3 Picture of Kulite surface pressure transducer designed for the experiment. ¹⁸	31
Figure 3.4 Amplitude and phase response for a typical Kulite transducer used in the experiment	32
Figure 4.1 A typical boundary layer profile just upstream of trailing-edge obtained by plotting local convection velocity U normalized on U at the edge of the boundary layer (U_1) against distance y from the plate normalized on y at the edge of the boundary layer (y_1)	35
Figure 4.2 A nomogram of the log law (equation 4.2) for different values of c_f	37
Figure 4.3 The pressure distribution about a NACA 0012 airfoil from the NACA Wartime Report. ²⁴	38
Figure 4.4 Demonstration of two-dimensional flow.	43
Figure 4.5 Airfoil pressure distribution.	44
Figure 5.1 A typical spectrum and phase plot of the trailing-edge noise sound field as obtained by cross-spectrum techniques	47
Figure 5.2 Sharp trailing-edge spectra at various upstream velocities U_∞ are shown along with the additional hump in the spectra resulting from the addition of bluntness to the edge.	48
Figure 5.3 The variation in the overall sound pressure level (SPL) with upstream velocity U_∞	50
Figure 5.4 Spectral collapse.	51
Figure 5.5 Opposing trailing-edge surface pressure signals.	57
Figure 5.6 Sound pressure levels (SPL) for various aircraft normalized on the parameter $\delta b/r^2$ by Fink, ⁹ where δ is the boundary layer thickness, b is span length, and r is the observer distance.	60

Page

Figure 5.7	The observer angles $\bar{\theta}$ of Ffowcs Williams and Hall ⁸ and θ of Goldstein ¹² are shown	63
Figure 5.8	The variation in the measured mean-square sound pressure with observer angle θ (or $\pi-\theta$) for the sharp trailing-edge along with the prediction of both Ffowcs Williams and Hall and Goldstein	65
Figure 6.1	A typical trailing-edge surface pressure spectrum for the blunt trailing-edge case ($U_\infty = 69.5$ m/s)	69
Figure 6.2	Mean-square surface pressure normalized on U^2 plotted against the reduced frequency parameter wv/U^2 along with the Bull ¹ infinite resolution curve for determination of high frequency response	70
Figure 6.3	Surface pressure phase	72
Figure 6.4	The frequency parameter $f\xi$, where f is a boundary frequency between any of the three frequency regions of in-phase, 180° out-of-phase, and non-correlated, is plotted against distances from the trailing-edge for various trailing-edge geometries	73
Figure 6.5	Variation of phase ϕ_{xy} and cross-spectrum level $ S_{xy} $ for various combinations of trailing-edge surface transducers x and y used to determine eddy convection speed.	75
Figure 6.6	A four pressure transducer cross-spectrum plot resulting from the cross-spectrum between a surface pressure difference signal (resulting from the simultaneous subtraction of two opposing Kulite surface pressure signals) and a farfield sound difference signal (resulting from the simultaneous subtraction of two opposing microphone sound pressure signals)	77

- Figure 7.1 A plot of wake convection velocity W normalized on upstream velocity U_∞ as a function of distance x from the trailing-edge as determined from a trailing-edge Kulite surface pressure transducer and a hotwire probe positioned in the wake 79
- Figure 11.1 Local convection velocity at the edge of the boundary layer, U_1 , versus upstream velocity, U_∞ , from rake measurements at 0.238 cm from trailing-edge and 2.54 cm from airfoil centerline with airfoil at 0° angle-of-attack. 90
- Figure 11.2 Skin friction coefficient, c_f , versus upstream velocity, U_∞ , from rake measurements at 0.238 cm from trailing-edge and 2.54 cm from airfoil centerline with airfoil at 0° angle-of-attack. 91
- Figure 11.3 Friction velocity, U^* , versus upstream velocity, U_∞ , from rake measurements at 0.238 cm from trailing-edge and 2.54 cm from airfoil centerline with airfoil at 0° angle-of-attack. 92
- Figure 11.4 Wall stress, τ_w , versus upstream velocity, U_∞ , from rake measurements at 0.238 cm from trailing-edge and 2.54 cm from airfoil centerline with airfoil at 0° angle-of-attack. 93
- Figure 11.5 Displacement thickness, δ^* , versus upstream velocity, U_∞ , from rake measurements at 0.238 cm from trailing-edge and 2.54 cm from airfoil centerline with airfoil at 0° angle-of-attack. 94
- Figure 11.6 Momentum thickness, θ , versus upstream velocity, U_∞ , from rake measurements at 0.238 cm from trailing-edge and 2.54 cm from airfoil centerline with airfoil at 0° angle-of-attack. 95
- Figure 11.7 Form factor, H , versus upstream velocity, U_∞ , from rake measurements at 0.238 cm from trailing-edge and 2.54 cm from airfoil centerline with airfoil at 0° angle-of-attack. . 96

	Page
Figure 11.8 Local convection velocity at the edge of the boundary layer, U_1 , versus upstream velocity, U_∞ , from rake measurements at 0.238 cm from trailing-edge and 2.54 cm from airfoil centerline with airfoil at 5° angle-of-attack.	98
Figure 11.9 Skin friction coefficient, c_f , versus upstream velocity, U_∞ , from rake measurements at 0.238 cm from trailing-edge and 2.54 cm from airfoil centerline with airfoil at 5° angle-of-attack.	99
Figure 11.10 Friction velocity, U^* , versus upstream velocity, U_∞ , from rake measurements at 0.238 cm from trailing-edge and 2.54 cm from airfoil centerline with airfoil at 5° angle-of-attack.	100
Figure 11.11 Wall stress, τ_w , versus upstream velocity, U_∞ , from rake measurements at 0.238 cm from trailing-edge and 2.54 cm from airfoil centerline with airfoil at 5° angle-of-attack.	101
Figure 11.12 Displacement thickness, δ^* , versus upstream velocity, U_∞ , from rake measurements at 0.238 cm from trailing-edge and 2.54 cm from airfoil centerline with airfoil at 5° angle-of-attack.	102
Figure 11.13 Momentum thickness, θ , versus upstream velocity, U_∞ , from rake measurements at 0.238 cm from trailing-edge and 2.54 cm from airfoil centerline with airfoil at 5° angle-of-attack.	103
Figure 11.14 Form factor, H , versus upstream velocity, U_∞ , from rake measurements at 0.238 cm from trailing-edge and 2.54 cm from airfoil centerline with airfoil at 5° angle-of-attack.	104
Figure 11.15 Local convection velocity at the edge of the boundary layer, U_1 , versus upstream velocity, U_∞ , from rake measurements at 0.238 cm from trailing-edge and 2.54 cm from airfoil centerline with airfoil at 10° angle-of-attack.	106

	Page
Figure 11.16 Skin friction coefficient, c_f , versus upstream velocity, U_∞ , from rake measurements at 0.238 cm from trailing-edge and 2.54 cm from airfoil centerline with airfoil at 10° angle-of-attack	107
Figure 11.17 Friction velocity, U^* , versus upstream velocity, U_∞ , from rake measurements at 0.238 cm from trailing-edge and 2.54 cm from airfoil centerline with airfoil at 10° angle-of-attack	108
Figure 11.18 Wall stress, τ_w , versus upstream velocity, U_∞ , from rake measurements at 0.238 cm from trailing-edge and 2.54 cm from airfoil centerline with airfoil at 10° angle-of-attack	109
Figure 11.19 Displacement thickness, δ^* , versus upstream velocity, U_∞ , from rake measurements at 0.238 cm from trailing-edge and 2.54 cm from airfoil centerline with airfoil at 10° angle-of-attack	110
Figure 11.20 Momentum thickness, θ , versus upstream velocity, U_∞ , from rake measurements at 0.238 cm from trailing-edge and 2.54 cm from airfoil centerline with airfoil at 10° angle-of-attack.	111
Figure 11.21 Form factor, H , versus upstream velocity, U_∞ , from rake measurements at 0.238 cm from trailing-edge and 2.54 cm from airfoil centerline with airfoil at 10° angle-of-attack.	112
Figure 11.22 Wall stress, τ_w , versus upstream velocity, U_∞ , from Preston tube measurements at 0.238 cm from trailing-edge on airfoil centerline with airfoil at 0° angle-of-attack	115
Figure 11.23 Friction velocity, U^* , versus upstream velocity, U_∞ , from Preston tube measurements at 0.238 cm from trailing-edge on airfoil centerline with airfoil at 0° angle-of-attack	116

	Page
Figure 11.24 Skin friction coefficient, c_f , versus upstream velocity, U_∞ , from Preston tube measurements at 0.238 cm from trailing-edge on airfoil centerline with airfoil at 0° angle-of-attack	117
Figure 11.25 Wall stress, τ_w , versus upstream velocity, U_∞ , from Preston tube measurements at 2.54 cm from trailing-edge on airfoil centerline with airfoil at 0° angle-of-attack.	119
Figure 11.26 Friction velocity, U^* , versus upstream velocity, U_∞ , from Preston tube measurements at 2.54 cm from trailing-edge on airfoil centerline with airfoil at 0° angle-of-attack	120
Figure 11.27 Skin friction coefficient, c_f , versus upstream velocity, U_∞ , from Preston tube measurements at 2.54 cm from trailing-edge on airfoil centerline with airfoil at 0° angle-of-attack.	121
Figure 11.28 Wall stress, τ_w , versus upstream velocity, U_∞ , from Preston tube measurements at 22.86 cm from trailing-edge on airfoil centerline with airfoil at 0° angle-of-attack	123
Figure 11.29 Friction velocity, U^* , versus upstream velocity, U_∞ , from Preston tube measurements at 22.86 cm from trailing-edge on airfoil centerline with airfoil at 0° angle-of-attack.	124
Figure 11.30 Skin friction coefficient, c_f , versus upstream velocity, U_∞ , from Preston tube measurements at 22.86 cm from trailing-edge on airfoil centerline with airfoil at 0° angle-of-attack	125
Figure 11.31 Variation in the overall sound pressure level (SPL) with upstream velocity, U_∞ , for a 0.9525 cm diameter rod	127

LIST OF SYMBOLS

a_o	speed of sound
AOA	angle of attack
b	span length
c	chord length; speed of sound
c_f	local skin friction coefficient
c_o	speed of sound
d	transducer diameter
D	distance
f	frequency
f_i	fluctuating surface force; local resultant stress (at each point y on the surface)
G	Green's function
$ G_{xy} $	cross-spectrum magnitude
H	form factor
k	wavenumber
K	constant
l	spanwise turbulence scale
L	span
M_o	Mach-number based on U_∞
M_v	Mach-number based on v
n	velocity exponent; surface normal
p	farfield sound pressure; pressure at a distance y from the surface of the airfoil
p_s	static pressure; surface pressure
$\langle p^2 \rangle$	mean-square sound pressure
p_{ij}	compressive stress tensor

r	distance of observer from source point
r_o	distance of source point from trailing-edge
R	distance of observer from source point
R'	distance of observer from image point
s	chordwise position
S	pressure coefficient; surface; wing area
SPL	sound pressure level
t	time
t'	retarded time
TBL	turbulent boundary layer
TE	trailing-edge
T_{ij}	Lighthill stress tensor
U	local fluid flow convection velocity; Fresnel integral limit
U_1	convection velocity at the edge of the boundary layer
U_∞	upstream velocity
v	fluctuating velocity
$v_{i,j}$	components of fluid velocity
V	flow convection speed; volume
\bar{V}	flow velocity
W	wake eddy convection velocity
x	observer position
$x_{i,j}$	observer coordinates
y	distance from surface of airfoil; surface coordinate
$y_{i,j}$	source coordinates

α	angle between observer and edge of plate; airfoil angle of incidence
β	angle between flow and plate
γ	vortex
Γ	vortex
δ	boundary layer thickness
δ^*	displacement thickness
δ_{ij}	Kronecker delta
Δp	pressure loading
θ	Momentum thickness; flyover angular position of observer
θ_o	source point angle with plane of plate
$\bar{\theta}$	flyover angular position of observer
μ	viscosity
ν	kinematic viscosity
ξ	distance of surface pressure measurement position from the trailing-edge
ρ	fluctuating fluid density
ρ_o	mean fluid density
τ_w	wall stress
ϕ_{xy}	phase
ψ	potential lines
ω	angular frequency

1. GENERAL INTRODUCTION

Aircraft related noise has been a topic of considerable research interest for more than two decades, with the first landmark theoretical paper on the subject - "On Sound Generated Aerodynamically. I." - being published in 1952 by M. J. Lighthill,¹⁷ and known as the acoustic analogy method. Much of the early work, both theoretical and experimental, concentrated on the understanding of jet noise. The contribution of aircraft body noise, which at that time was relatively small, was ignored. However, the advent of large aircraft such as jumbo-jets with their much larger surface areas coupled with the considerable success that has been achieved in the reduction of jet noise has led to an increased examination of the noise generated by aircraft body surfaces. Indeed, body noise may eventually present a new noise floor, i.e. a lower bound, to further reductions that might occur if jet engine noise reductions of order 10dB are achieved in the next decade, and thus may be of primary importance during aircraft landing approaches when the engines are throttled.⁴ It may be postulated, moreover, that this noise floor cannot be lowered below an absolute lower bound that would be set by two-dimensional flow over an optimally designed wing of large aspect ratio. Effects of flaps, slats and three-dimensional effects would be expected to increase this lower bound level.

The interest in this lower bound which is set by two-dimensional flow over an airfoil has provided the impetus for the present investigation. From theoretical results it can be anticipated that a

major source of body noise for two-dimensional flow will result from the flow in the vicinity of the trailing-edge of the wing. Thus experimental measurements of trailing-edge noise radiated by the two-dimensional flow over an airfoil will be compared with predicted results from theoretical considerations.

2. THEORY

2.1 Introduction

In an effort to reduce the full-scale trailing-edge noise problem to its simplest form, the problem is modeled physically as the interaction of low Mach-number two-dimensional turbulent flow with the edge of a semi-infinite thin rigid plate (see figure 2.1). Howe¹⁶ has given a comprehensive review of various mathematical theories developed to treat this problem using some form of vortex or "eddy" passing the edge of a rigid semi-infinite flat plate (see figure 2.2). These theories were divided by Howe into three categories, namely those based on (1) the Lighthill acoustic analogy,¹⁷ (2) the linearized hydroacoustic equations, and (3) ad hoc models. Howe demonstrated that the various approaches to the trailing-edge problem all lead essentially to the same basic parametric dependencies for the mean-square sound pressure $\langle p^2 \rangle$ as was described by the acoustic analogy result of Ffowcs Williams and Hall⁸ namely

$$\langle p^2 \rangle = \rho_0^2 v^2 M_v^2 \left(\frac{L}{R} \right)^2 \sin \alpha \sin^2 \left(\frac{\theta}{2} \right) \cos^3 \beta \quad (2.1)$$

where ρ_0 is the density of the fluid, v is the fluctuating velocity, V is the flow convection speed, M_v is the Mach-number based on V , L is the span length of the plate, ξ is a spanwise turbulence scale, R is the distance of the observer from the trailing-edge, α is the angle

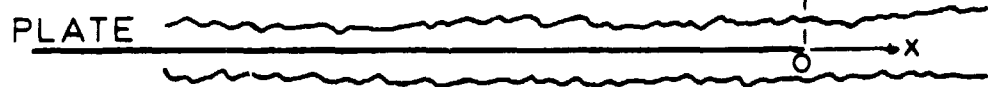
4

FLOW →



(a)

FLOW →



(b)

Figure 2.1 Trailing-edge noise problem (a) modeled physically as the interaction of low Mach-number two-dimensional turbulent flow with the edge of a semi-infinite thin rigid plate (b).

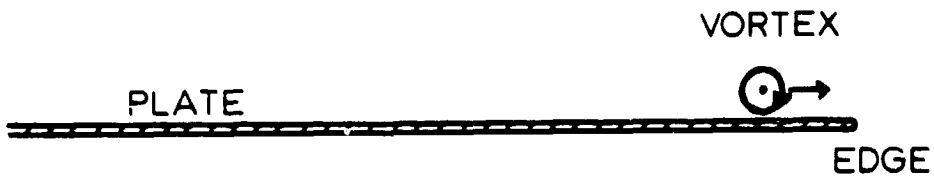


Figure 2.2 Trailing-edge noise model. Various mathematical theories treat the trailing-edge noise problem using some form of vortex model passing the edge of a semi-infinite flat plate as shown.

between the observer and the edge of the plate, $\bar{\theta}$ is the "flyover" angular position of the observer, and β is the angle the flow makes with an extension to the plane of the plate (see Figures 2.3, 2.4). Thus all the theories reviewed by Howe lead to the dependence of $\langle p^2 \rangle$ on the following important parameters: (1) the fifth power of the flow velocity since $v^2 V^2 M_\infty \sim V^5$, (2) the "scale factors," span length L , and spanwise turbulence scale ℓ , and (3) the observer coordinates R and $\bar{\theta}$, giving rise to the usual R^{-2} acoustic fall-off in the mean-square sound pressure with distance and a $\sin^2(\bar{\theta}/2)$ directivity pattern (see figure 2.5). (Note: The appearance of the modulus of the angle, $\bar{\theta}$, is of importance in the complex plane transformation in the theory.)

The various theoretical treatments leading to the basic result of equation 2.1 will now be examined in more detail, beginning with a physical description of the phenomenon involved in the production of the trailing-edge noise. This is followed by discussions of the various analytical approaches to the trailing-edge noise problem.

2.2 Physical View of the Trailing-edge Noise Phenomenon

The local surface pressure field of the boundary layer on a flat rigid plate can be viewed physically as a distribution of nearly statistically independent point forces over the rigid plate which fluctuate in time and space. Such a fluctuating force phenomenon might be viewed in the light of simple acoustic radiation theory as indicative of a distribution of point dipole sources of sound over the

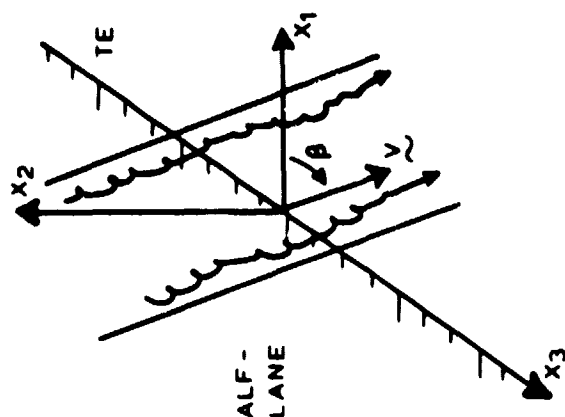


Figure 2.4 (after Howe^[6])
Illustration of the angle
 β between the flow velocity
 v and an extension (x_1) to
the half-plane

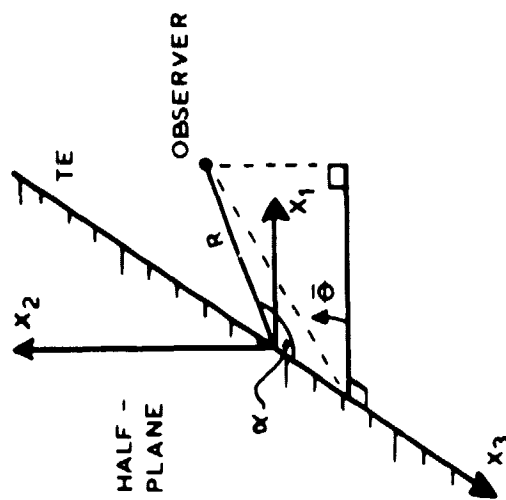


Figure 2.3 (after Howe^[6])
Observer coordinates
 R , $\bar{\theta}$, and $\bar{\alpha}$ shown
in relation to the plate
and a rectangular
coordinate system

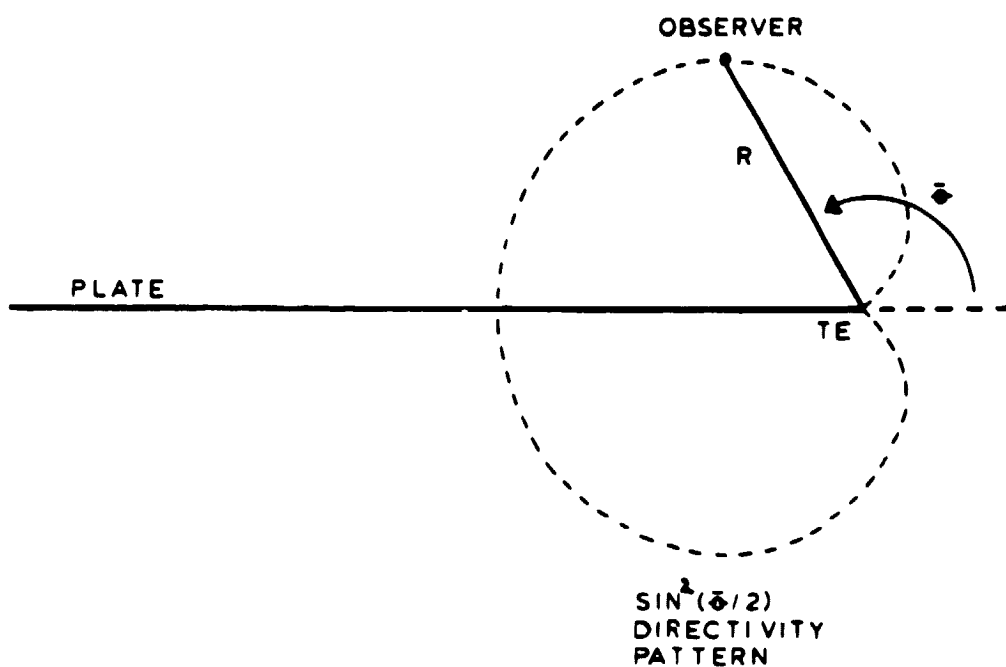


Figure 2.5 The $\sin^2(\theta/2)$ directivity pattern predicted for the mean-square sound pressure variation with observer angle θ .

surface of the plate. However, far upstream from the edge of a semi-infinite plate, reflections of the point dipoles at the plate boundary produce an almost complete cancellation to form quadrupoles. That is, the reflection of the dipoles results in the effective formation of a quadrupole source distribution and its characteristic decreased efficiency of radiation (see figure 2.6). However, as the individual centers of turbulence or eddies approach the edge of the semi-infinite plate, the reflective cancellation must end. Such a time rate of change in events - effectively a time rate of change in boundary conditions as seen by the turbulent eddies - is characteristic of another sound producing phenomenon (see figure 2.7). This then suggests that the trailing-edge alters the character or "scatters" the turbulence incident upon it from upstream and that sound is generated as a result of this scattering.

With this physical picture of the trailing-edge noise phenomenon in mind, a more analytical approach to the problem will now be considered.

2.3 The Formulation of Ffowcs Williams and Hall

Ffowcs Williams and Hall⁶ approached the problem of noise production resulting from flow interactions with the trailing-edge of a semi-infinite plate by direct use of Lighthill's form of the acoustic wave equation¹⁷ for the fluctuating density ρ , that is

$$\nabla^2 \rho - \frac{1}{c^2} \frac{\partial^2 \rho}{\partial t^2} = -\frac{1}{c^2} \frac{\partial^2}{\partial y_i \partial y_j} (\rho v_i v_j + p_{ij} - c^2 \rho \delta_{ij}) \quad (2.2)$$

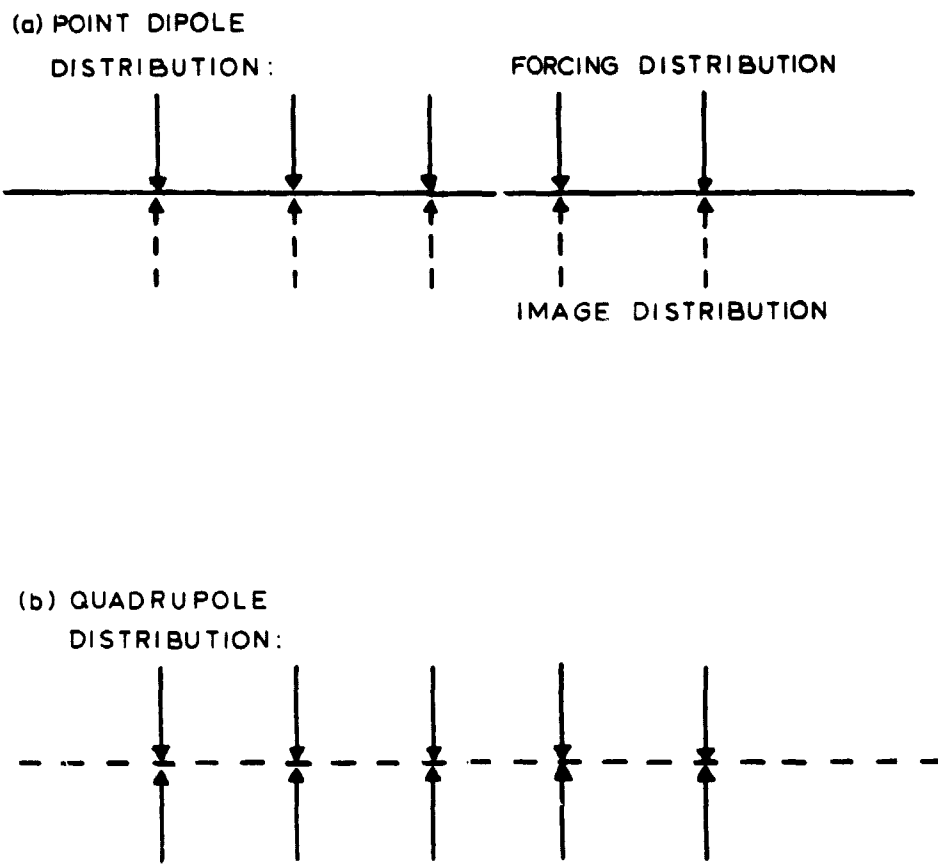


Figure 2.6 Plate reflections. Far upstream from the edge of a semi-infinite plate, reflection of a point dipole distribution of sound sources (a) at the plate boundary produces an almost complete cancellation to form a quadrupole distribution of sound sources (b).

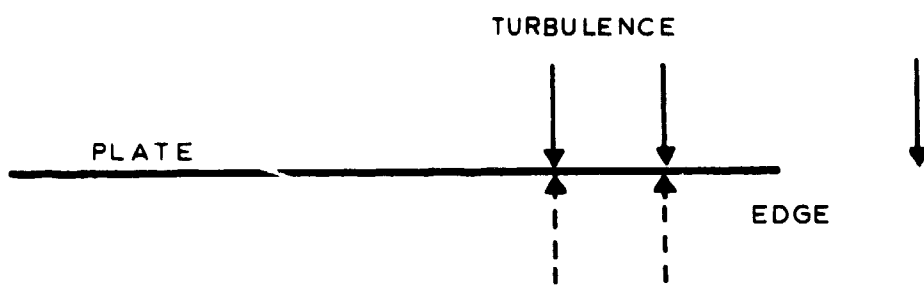


Figure 2.7 The semi-infinite plate model. As turbulence approaches the edge of a semi-infinite plate, reflective cancellation of the sound sources must end. This time rate of change in boundary conditions as seen by the turbulent eddies results in the production of sound.

where c is the speed of sound propagation in the fluid, y_i and y_j are source coordinates, v_i and v_j are components of the fluid velocity, p_{ij} is the compressive stress tensor, and where the Kronecker delta δ_{ij} equals unity when $i = j$, and is zero otherwise. Ffowcs Williams and Hall then showed that the solution of the acoustic wave equation 2.2 for the case of the semi-infinite thin rigid plate could be written to obtain the acoustic pressure $p(x; \omega)$ at frequency ω as

$$p(x, \omega) = \frac{1}{4\pi} \int_V \left(\frac{\partial^2 \rho v_i v_j}{\partial y_i \partial y_j} \right) G dv + \frac{1}{4\pi} \int_S \frac{\partial p_s}{\partial n} G ds. \quad (2.3)$$

This solution implies that the farfield sound pressure p with angular frequency ω at observer position x results from sound sources, which may be represented by a quadrupole distribution related to the quantity $\rho v_i v_j$ within the volume V of the turbulence and by a surface distribution of dipoles over the surface S dependent upon the surface pressure p_s , by means of a Green's function G appropriate for the case of a source near the edge of a semi-infinite plate (see later). Ffowcs Williams and Hall then rewrote the solution 2.3 in terms of volume quadrupole sources only, as

$$p(x, \omega) = \frac{1}{4\pi} \int_V (\rho v_i v_j) \frac{\partial^2 G}{\partial y_i \partial y_j} dv. \quad (2.4)$$

The physical significance of equation 2.4 is that it describes a uniquely quadrupole volume source type of acoustic radiation and

results conceptually from the effective reflection of the surface dipole sources represented by the surface integral in equation 2.3 by the plate and the incorporation of these new volume quadrupole components with those already represented in equation 2.3 (see figure 2.8.).

Ffowcs Williams and Hall then made use of the Green's function of McDonald¹⁹, which is appropriate for the case of a source near a diffracting semi-infinite plate, namely

$$G = \frac{e^{iw/4}}{\pi^{1/2}} \left[\frac{e^{-ikR}}{R} \int_{-\infty}^{U_R} e^{-iu^2} du + \frac{e^{-ikR'}}{R'} \int_{-\infty}^{U_{R'}} e^{-iu'^2} du \right] \quad (2.5)$$

where

$$U_R = 2 \left(\frac{krr_o}{D+R} \right)^{1/2} \cos \frac{\theta-\theta_o}{2} = \pm [k(D-R)]^{1/2}$$

and

$$U_{R'} = 2 \left(\frac{krr_o}{D+R'} \right)^{1/2} \cos \frac{\theta+\theta_o}{2} = \pm [k(D-R')]^{1/2},$$

and where D is the shortest distance between the source and field points via the edge and where the wavenumber k equals ω/c , see Figure 2.9 for geometry. Physically, this Green's function incorporates the reflective influence of the plate, where $(e^{-ikR'})/R'$ is the mirror image of the free-space Green's function $(e^{ikR})/R$, and the diffractive influence of the edge which is embodied in the Fresnel

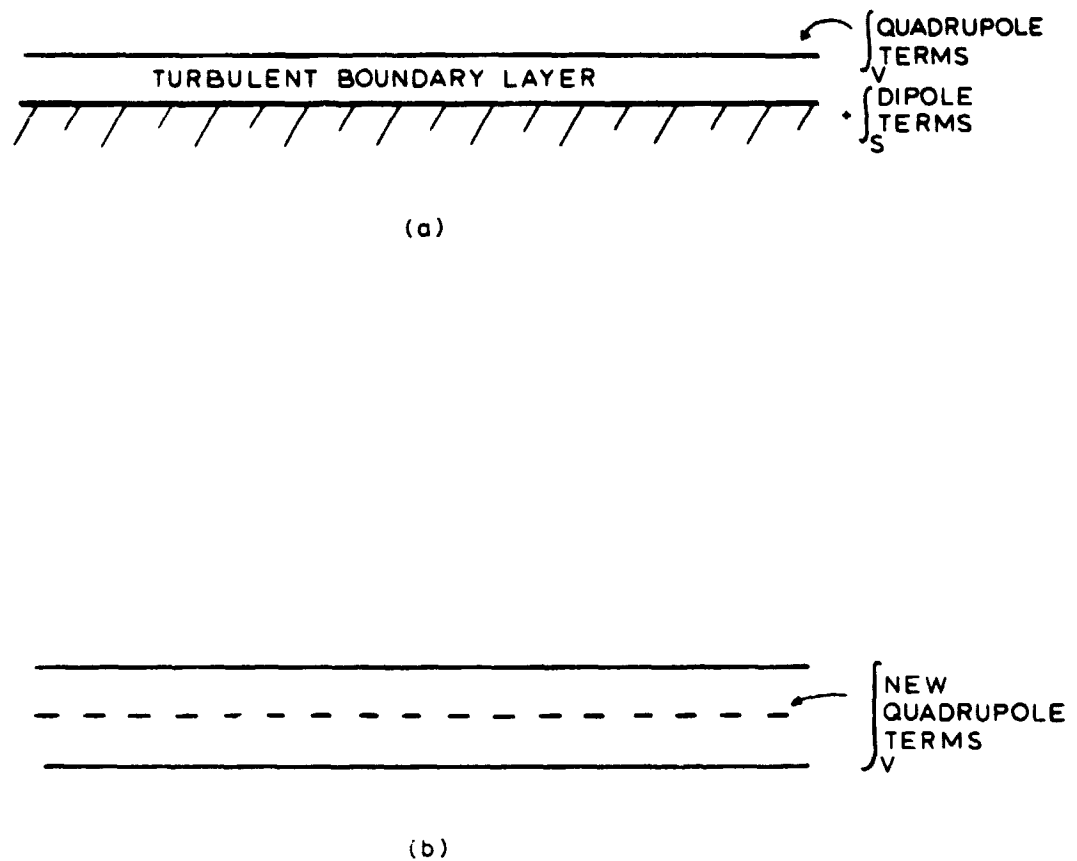


Figure 2.8 Physical interpretation of equations 2.3 and 2.4. Equation 2.3 describes a sound source distribution using both quadrupole and dipole terms (a) whereas equation 2.4 accounts for the reflective influence of the plate by describing the source distribution completely with quadrupole terms (b).

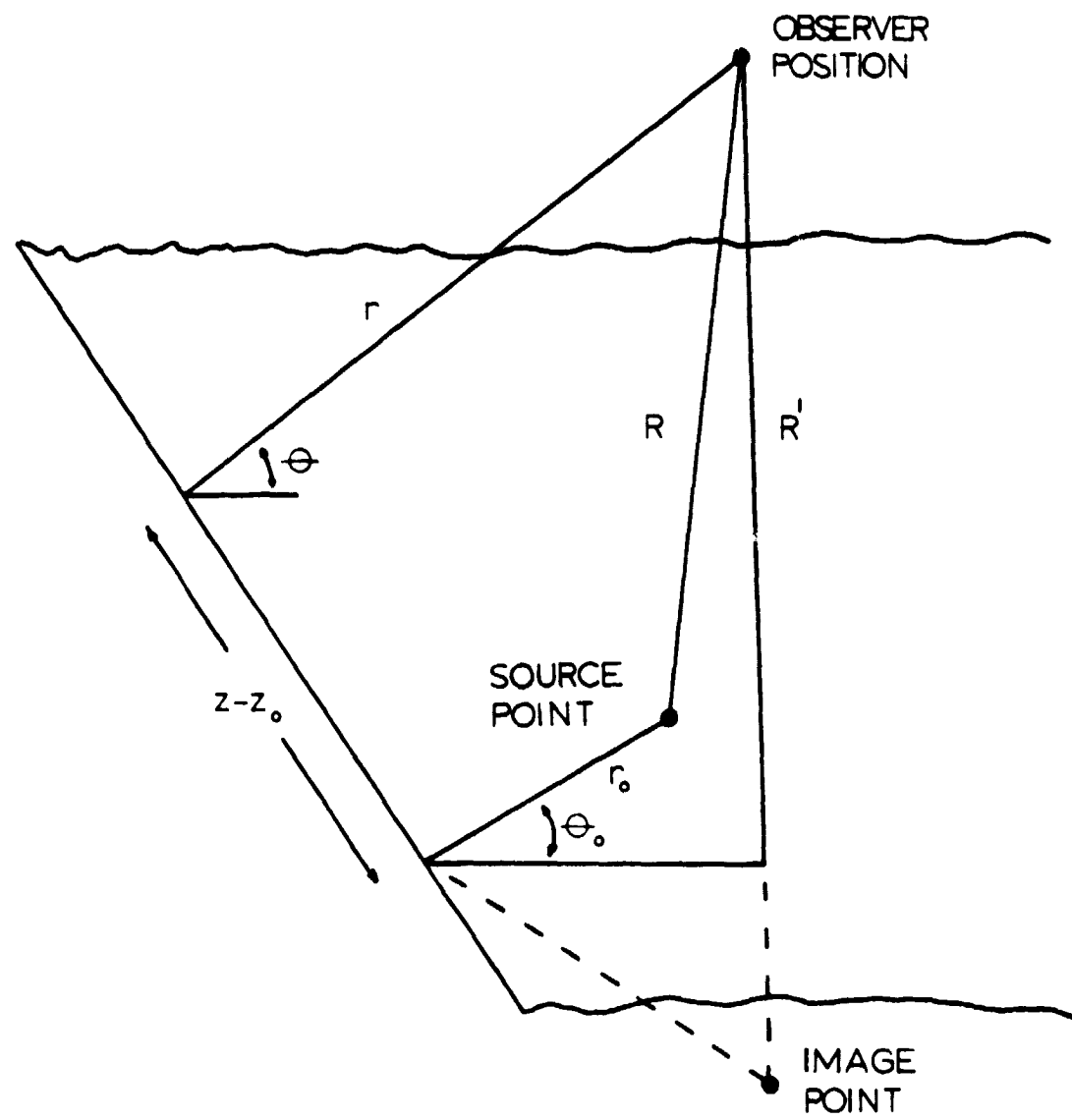


Figure 2.9 (after Ffowcs Williams and Hall⁸) Geometry for the McDonald¹⁹ Green's function for a semi-infinite plane.

integrals $\int e^{-iU^2} dU$. Ffowcs Williams and Hall pointed out that (1) any enhancement of the sound from a semi-infinite plate over that of an infinite plate results from derivatives of these Fresnel integrals, since the Fresnel integrals themselves are limited to values between zero and one and that (2) these derivatives contain $(D-R)^{-1}$ and $(D-R')^{-1}$ terms which become infinite as the source point approaches the edge since R and R' equal D when the source is at the edge, so that the mathematics which result in enhancement of the sound field also result in the introduction of a mathematical singularity into the problem.

By incorporating the Green's function of equation 2.5 into equation 2.4 for the case of a turbulent eddy at a distance r_0 upstream but near the edge so that $2kr_0 \ll 1$, where k is the wavenumber, then an expression of the form of equation 2.1 was obtained for the mean-square sound pressure.

2.4 Alternative Formulations

In an alternative formulation, Crighton⁵ modeled the edge-noise problem as the approach of a line vortex toward the edge of a semi-infinite plate under the influence of a potential field. The pertinent mathematical techniques involved the matching of a wave field in "outer" coordinates to an incompressible field in "inner" coordinates. Howe^{15,16} reformulated the approaching line vortex problem by direct use of the Lighthill acoustic analogy which resulted in an expression relating the radiated sound field to the rate at which vortices cross potential lines. Besides resulting in an expression

for the mean-square pressure of the radiated sound in agreement with the Ffowcs Williams and Hall equation 2.1, this method has great merit in presenting a clear, physical interpretation of the effect of application of the mathematical technique called the "Kutta condition," as discussed later.

In an effort to avoid consideration of the Lighthill volume source term - a term considered unmeasurable in practice because it contains products of derivatives of the fluctuating velocities - as a noise generation mechanism in the presence of a sharp edge, Chase³ developed a model based exclusively on integration of the surface pressure terms. This approach was termed a "linearized hydroacoustic approach" by Howe,¹⁶ since it uses an assumed form of the nearfield pressure spectrum to predict the farfield radiated sound pressure spectrum. The resulting sound field, when integrated over the entire frequency spectrum, scales as the fifth power of a characteristic flow velocity - concurring with the velocity dependency result of Ffowcs Williams and Hall, equation 2.1.

In another "linearized hydroacoustic" approach to the trailing-edge noise problem Chandiramani² developed a model which employed, by means of a free-space Green's function, both surface pressure and volume source terms. This approach, like that of Chase, required a detailed knowledge of the surface pressure distribution. Despite this difficulty, however, Chandiramani's formulation again resulted in a fifth power dependency of the mean-square sound pressure on the flow velocity as in the Ffowcs Williams and Hall equation 2.1. Also, this formulation further illustrated the scattering effect of the

trailing-edge as depicted in Figure 2.10, where an eddy is seen to radiate strongly as it is altered or scattered (diffracted) by the edge of a semi-infinite plate. Of course in the airfoil case there are two boundary layers, on the upper and lower surfaces, and so there will be contributions to the scattered field from both sides.

In an "ad hoc" approach, Hayden, Fox and Chanaud¹⁴ developed a dipole model of the edge noise problem which indicated that noise is generated as the result of rapid acceleration of the fluid medium upon encountering the trailing-edge. A source dipole strength was calculated and taken to be the major contributor to the farfield sound. However, in their derivation of an expression relating the farfield sound to flow velocity, Hayden et al. failed to take into account the fact that the contribution to the sound field made by a source near the edge "decreases very slowly as a function of distance" from the edge.¹⁶ Howe reworked the problem to include this decay in source contribution with distance from the trailing-edge. The resulting expression relating the farfield sound field to flow velocity is in essential agreement with the Ffowcs Williams and Hall result 2.1. Thus all of the various approaches to the trailing-edge noise problem discussed above lead to parametric dependencies for the mean-square pressure of the radiated sound in substantial agreement with the Ffowcs Williams and Hall result 2.1. With these different analytical approaches to the trailing-edge problem now in mind, it will be instructive to consider the basic differences in approach, which involves the selection of an appropriate Green's function, presented by some of the various theories.

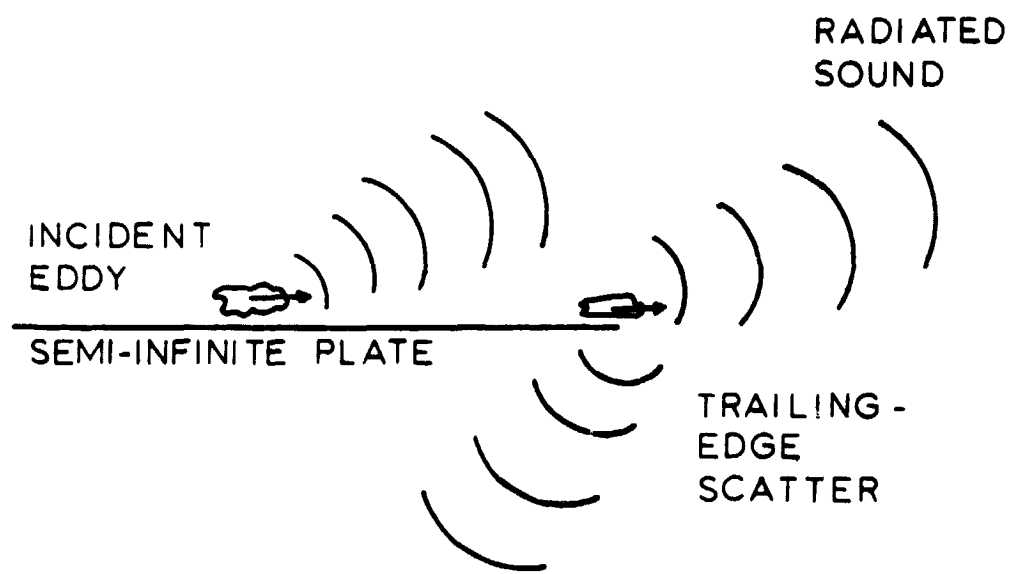


Figure 2.10 An eddy is seen to radiate strongly as it is altered or "scattered" by the edge of a semi-infinite plate.

2.5 Green's Functions Used in Various Formulations of the
Trailing-edge Noise Problem

A thorough examination of the various formulations of the trailing-edge noise problem reveals the use, in some of these formulations, of at least three different Green's functions to satisfy the same basic equation, that is, a Curle⁶ type equation for the fluctuating density ρ :

$$\rho = \frac{1}{c_0^2} \int_{-t}^t \int_V \frac{\partial^2 G}{\partial y_i \partial y_j} T_{ij} dv dt + \frac{1}{c_0^2} \int_{-t}^t \int_S \frac{\partial G}{\partial y_i} f_i ds dt^{11} \quad (2.6)$$

where c_0 is the speed of propagation of sound in the fluid, t is time, y_i and y_j are source coordinates, and where the sound sources are represented by a quadrupole distribution related to the Lighthill stress tensor T_{ij} within the volume V and by a surface distribution of dipoles over S dependent upon the fluctuating surface force f_i by means of some appropriate Green's function G . The equation 2.6 may be solved for the sound using either a free-space Green's function or a Green's function "tailored" to the specifics of the given problem. The use of the free-space Green's function may, however, lead to erroneous results unless the surface dipole terms are known with extreme precision - a tenet often unrealizable in problems involving bodies of large spatial extent within turbulent flows.¹¹ This difficulty can, however, be avoided by the use of a "problem tailored" Green's function contrived to minimize the surface dipole

terms. On the other hand, if there is a need for a more detailed knowledge of the nearfield-farfield pressure interactions, it will be necessary to suppress the volume source integral in favor of the surface source integral with an appropriately "tailored" Green's function.

Thus three basic Green's function formulations for the trailing-edge problem have arisen: (1) the Green's function of Ffowcs Williams and Hall "tailored" to remove the surface integral, (2) the Green's function of Chase "tailored" to remove the volume integral, and (3) the free-space Green's function used by Chandiramani. Although approaches (2) and (3) require a more detailed knowledge of the surface pressure field, a more intricate relationship between properties of the flow and the resulting radiated sound can theoretically be obtained than with approach (1). Thus the selection of a Green's function for the solution of equation 2.6 involves a trade-off between ease of solution and detail of knowledge of the nearfield-farfield pressure interactions.

Again, despite their diversity of approach to the problem, the various trailing-edge noise theories lead to predictions for the mean-squared pressure of the radiated sound in essential agreement with the Ffowcs Williams and Hall result 2.1. However, these theories have all modeled the trailing-edge noise problem based on an assumption of negligible viscosity. Therefore, the mathematical step in potential flow, that is inviscid, problems used to closely model the real situation of viscosity will now be considered along with the resulting

effect on the level of the mean-square sound pressure predicted by equation 2.1.

2.6 The Kutta Condition

The various formulations of the trailing-edge noise problem have chiefly ignored the quantitative effect of real flow viscosity. However, the predicted level of the radiated sound is greatly affected by the inclusion of a mathematical requirement that the flow, to avoid producing a mathematical singularity, leave any surface tangentially,²⁰ a requirement which closely models the real flow situation where no singularity occurs because of the "softening" effect of viscosity.¹⁶ This mathematical requirement in potential flow, that is inviscid, problems is called the Kutta condition.

Accordingly, the Ffowcs Williams and Hall trailing-edge noise result expressed by equation 2.1 "essentially rests on the potential field singularity of the diffraction problem at the edge and would be substantially modified if any type of "Kutta" condition were invoked to limit its effect."⁸ That is, the same mathematical technique which results in an enhancement of the sound field also introduces a singularity into the formulation. Thus any softening of that singularity results in a lessening of the enhancement effect and a lowering of the predicted value of the mean-square pressure of the radiated sound. Similarly, the application of the Kutta condition to the other trailing-edge noise models would also be expected to result in a lowering of the predicted mean-square sound pressure levels.

A result of Howe,¹⁶ namely that the

$$p = \frac{\rho_0 \sin(\bar{\theta}/2)}{\pi R^{1/2}} [\Gamma (\frac{dy}{dt}) + \gamma (\frac{dy}{dt})] \quad (2.7)$$

where ρ_0 is the density of the fluid and where R and $\bar{\theta}$ are observer coordinates (see Figure 2.11), connects the radiated sound pressure p to the rate at which vortices Γ and γ cross potential lines y . Here the Kutta condition is applied by having a second vortex γ of equal strength to the incident vortex Γ leaving the trailing-edge so that the flow is tangential and the sound produced by the two eddies tends to cancel. Howe connected this effect of application of the Kutta condition to the Ffowcs Williams and Hall no-Kutta prediction equation 2.1 as a reduction in the predicted mean-square pressures of the radiated sound by a factor of $(1-W/V)^2$, where W is the wake eddy convection velocity and V is the eddy convection velocity upstream of the wake and near the surface of the plate.

It should be realized, however, that the Howe two-eddy model for application of the Kutta condition is not observed in practice for the complex case of an airfoil wetted on both sides with turbulent boundary layers. Of course, in practice a wake will form near and downstream of the trailing-edge. From geometrical considerations, then, it might be argued that in the presence of a vortex sheet representing the wake, the eddy would not be subject to a boundary condition change at the trailing-edge and it would be seen that the sound radiation would be zero (see Figure 2.12). Therefore it would be expected that in

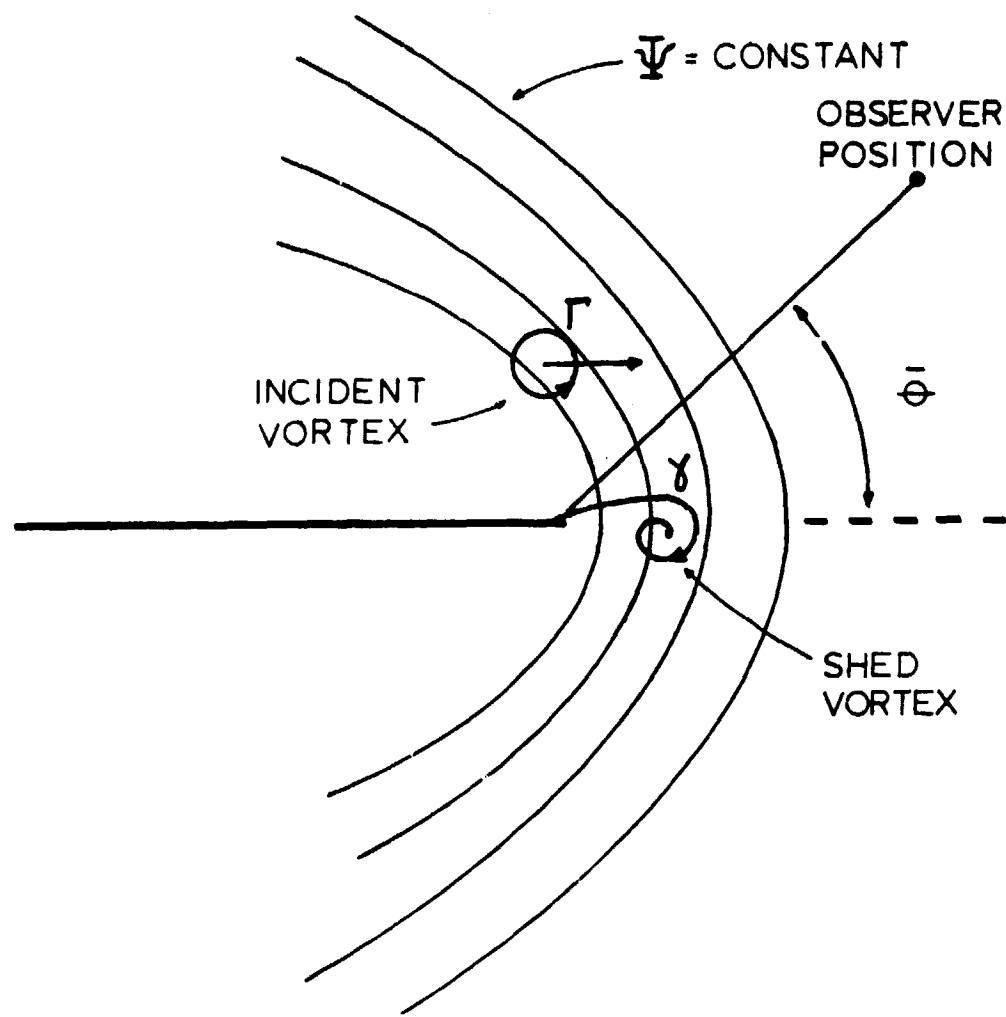


Figure 2.11 (after Howe¹⁰) The Kutta condition. The Kutta condition is applied here by having a second vortex γ of equal strength to the incident vortex Γ leave the trailing-edge such that the sound field produced by the two vortices (vortices) crossing lines of constant potential Ψ tends to cancel.

practice the trailing-edge noise would be less than the no-Kutta condition theoretical prediction.

Thus it was realized, like other workers,⁸ that an exacting experiment needed to be performed to measure the trailing-edge noise per unit span for two-dimensional flow over an airfoil in order to establish this lower bound noise level and to compare it with predicted theoretical results as well as full-scale flyover data for aircraft in the "clean" configuration (that is, in the cruise configuration with flaps and landing gear retracted).

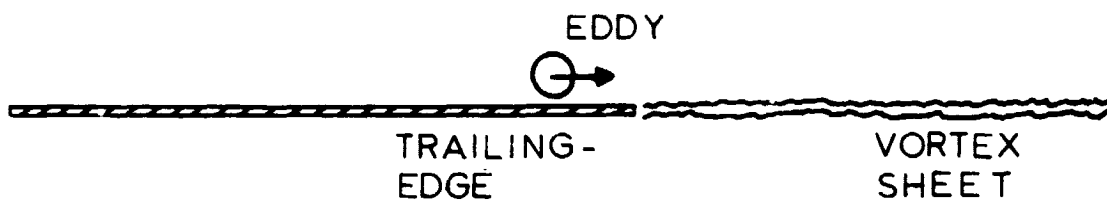


Figure 2.12 Eddy-edge interaction. In the real flow situation where a wake forms behind the airfoil (represented here by a vortex sheet) an eddy approaching the trailing-edge may see no boundary condition change with time and may not therefore produce trailing-edge noise.

3. EXPERIMENTAL DESCRIPTION

In order to perform the desired trailing-edge noise measurements, tests were conducted in the quiet-flow anechoic facilities at the NASA Langley Acoustics and Noise Reduction Laboratory (ANRL). The airfoil, flow conditions, and signal transducers for the experiment are described below.

An aluminum NACA 0012 airfoil of 0.61 m chord and 0.46 m span was supported by two reinforced sideplates designed to maintain two-dimensional flow over the airfoil (see Figure 3.1) and was immersed completely within the potential core, that is laminar, region of a 0.3 m x 0.46 m low turbulence jet in such a manner as to insure that laminar flow was maintained in the free-stream up to and past the trailing edge of the airfoil. As can be seen in Figure 3.1, the sideplates were covered with porous foam at their rear edges to reduce extraneous edge noise. A 2.54 cm width roughness strip was placed at 15% chord from the leading edge on both sides of the airfoil as a boundary layer "trip" so that two separate but statistically equivalent turbulent boundary layers were formed. Tests were performed with the upstream velocity U_∞ ranging from a value of 30.9 m/s up to 73.4 m/s with the NACA 0012 airfoil at angles of incidence $\alpha = 0^\circ$, 5° , and 10° . However, the case of $\alpha = 0^\circ$ is chiefly reported since the angle of incidence seemed to have a negligible effect on the results. Several trailing-edge geometries, in addition to the standard "blunt" geometry of the NACA 0012 (see Manley¹⁸ for details), were achieved by

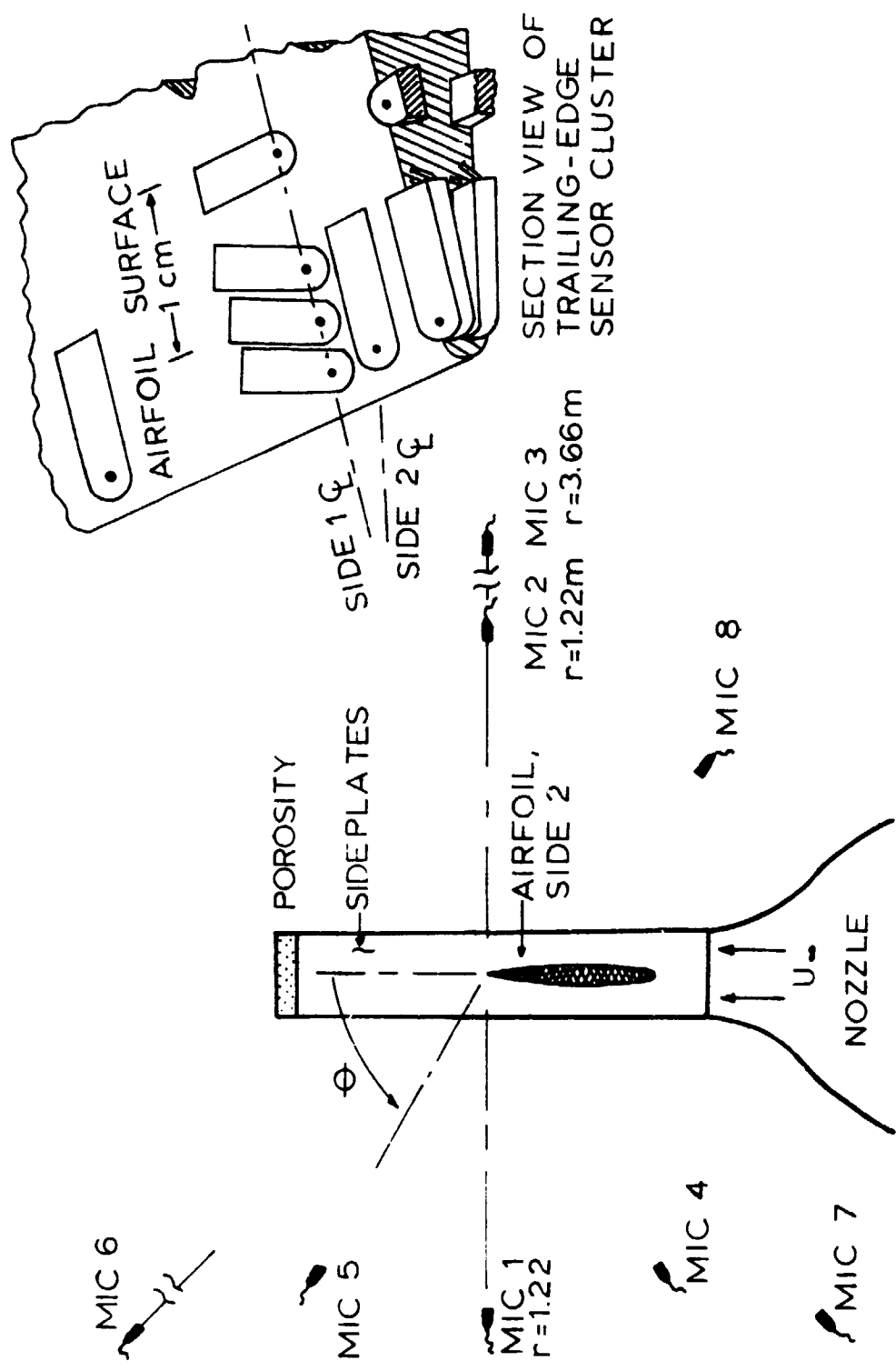


Figure 3.1 The basic microphone and airfoil geometry and the trailing-edge Kulite placement.

contouring wooden trailing-edge extensions, see Figure 3.2. Most of the data analysis, however, involved the standard "blunt" trailing-edge and the "sharp" trailing-edge geometries depicted in Figure 3.2.

The radiated noise was measured by using eight 1.27 cm Brüel and Kjaer type 4133 condenser microphones positioned around the airfoil as shown in Figure 3.1. Noise spectra were determined using the cross-spectra between microphones on opposite sides of the airfoil. Sound pressures at these "opposing" positions were 180° out of phase over the frequency range corresponding to the measured trailing-edge noise.

Measurements of surface pressure fluctuations were accomplished with 32 Kulite pressure transducers of special development and design (see Figure 3.1 for the placement of trailing-edge Kulites and Figure 3.3 for a photograph of an unmounted Kulite transducer) with a Helmholtz resonance of 63 kHz¹⁸ and with extremely flat amplitude and phase response to 20 kHz (see Figure 3.4) as checked in a specially developed pressure coupler. (For details of the design, calibration, and installation of the Kulite pressure transducers, including the design and operation of the pressure coupler, see Manley.¹⁸)

In the boundary layer, a boundary layer "rake," a series of small pressure sensitive Pitot tubes arranged side-by-side in a linear array, was used to measure the velocity distribution in the boundary layer close to the airfoil as a function of distance from the surface. Pressure measurements were also taken next to the surface of the airfoil by the use of a 0.127 cm diameter Preston tube at various spanwise and chordwise positions.

TRAILING-EDGE GEOMETRY

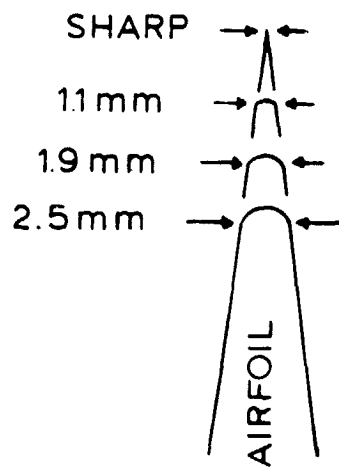


Figure 3.2 Trailing-edge geometries used in the experiment. Note especially the "sharp" and the 2.5 mm "blunt" geometries.

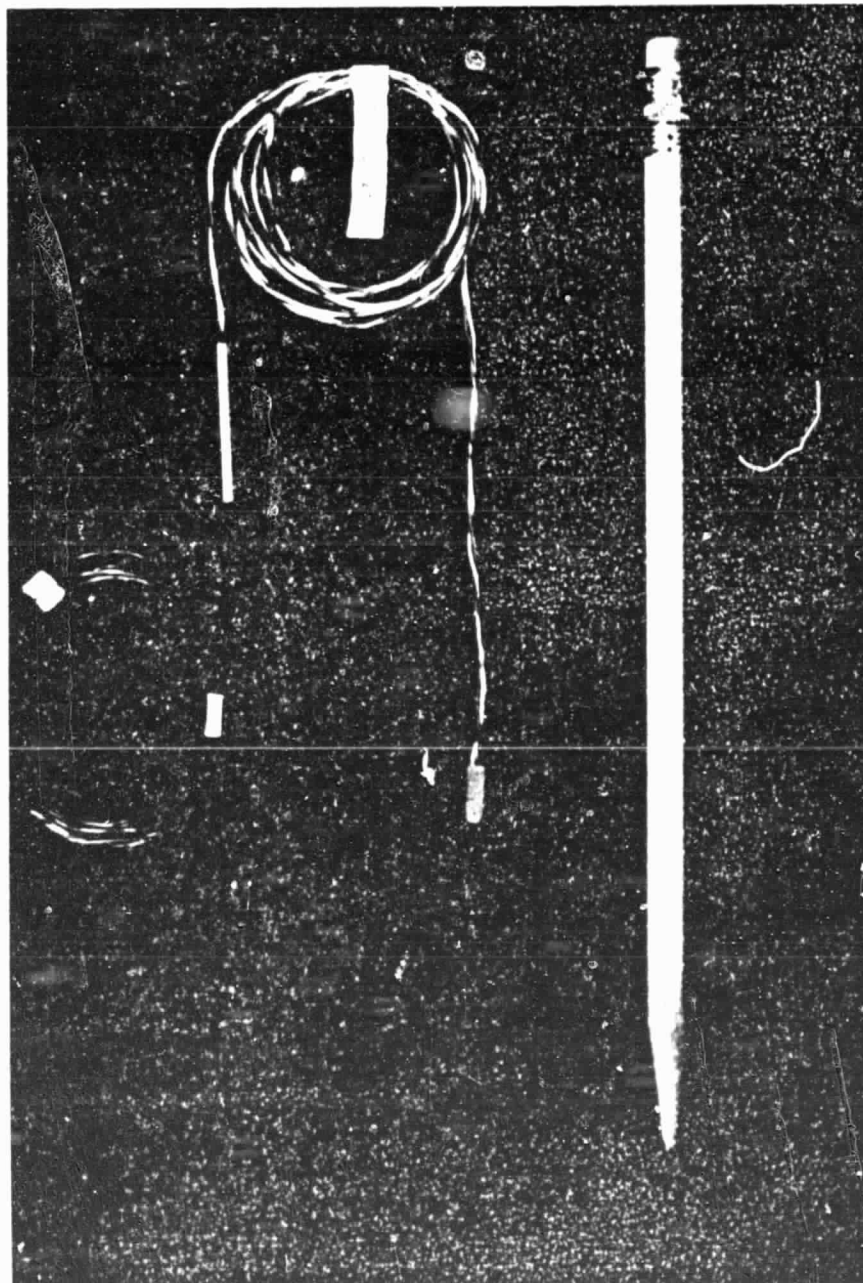


Figure 3.3 Picture of Kulite surface pressure transducer designed for the experiment.¹⁸

ORIGINAL PAGE IS
OF POOR QUALITY

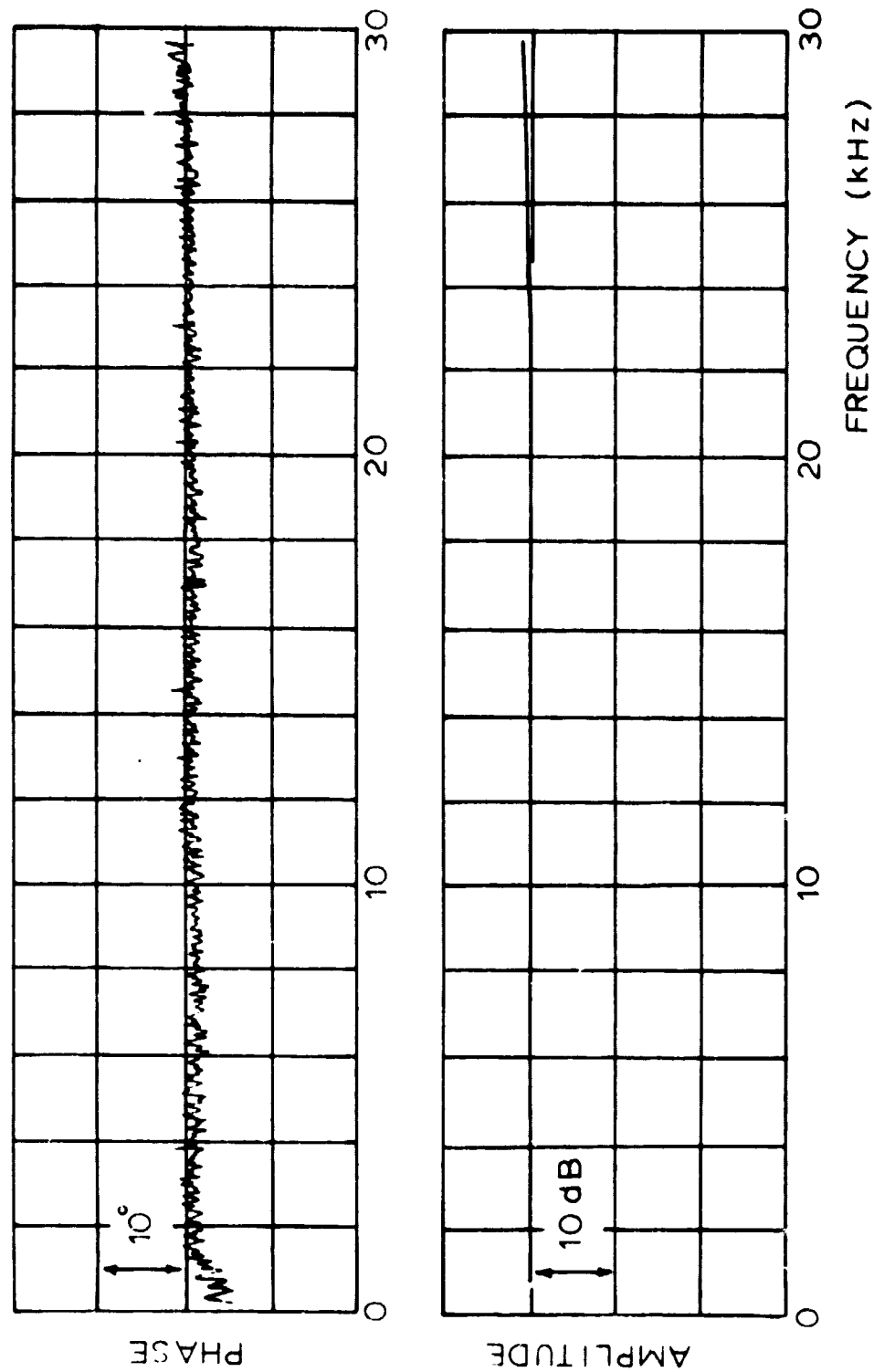


Figure 3.4 Amplitude and phase response for a typical Kulite transducer used in the experiment. Note the unusually flat response of the transducer.

Measurements of the wake mean velocity and fluctuating velocity behind the airfoil were accomplished by means of a two channel linearized hotwire anemometer manufactured by Thermosystems and using a cross-wire probe with 0.00381 mm diameter tungsten wires.

Analogue data signals obtained from these transducers were recorded magnetically (FM) for later analysis which used both commercially available real-time spectrum analyzers as well as Fourier transform software by digital computer. For a complete discussion of the data collection procedures and the signal conditioning and processing techniques involved, see Manley.¹⁸

With the above described airfoil, flow conditions, and signal transducers, tests for the measurement of the trailing-edge noise were performed. The results of these tests with comparison to theory and full-scale data follow.

4. BOUNDARY LAYER MEASUREMENTS AND RESULTS

4.1 Boundary Layer Rake Measurements

From equation 2.1 it was anticipated that the boundary layer thickness δ proportional to the spanwise turbulence scale ℓ would need to be determined in the experiment in order to correctly scale the model results to full-size. Also the amplitude of the pressure fluctuations in the turbulent boundary layer on the two surfaces of the airfoil was known to depend on the local skin friction coefficient c_f . Hence a thorough investigation of these parameters was performed.

With this purpose in mind, a boundary layer rake consisting of a series of small pressure sensitive Pitot tubes was employed to directly measure the velocity distribution in the boundary layer of the airfoil as a function of distance from the surface of the airfoil. The local fluid flow velocity U within the boundary layer at various distances y from the surface of the airfoil was then determined from Bernoulli's equation as

$$U(y) = \left[\frac{2(p - p_s)}{\rho} \right]^{1/2} \quad (4.1)$$

where p is the pressure measured at a particular distance y from the airfoil surface, p_s is the "static pressure" which corresponds to the pressure on the surface of the airfoil, and ρ is the fluid density. From the boundary layer profile U versus y , (see figure 4.1 for a plot

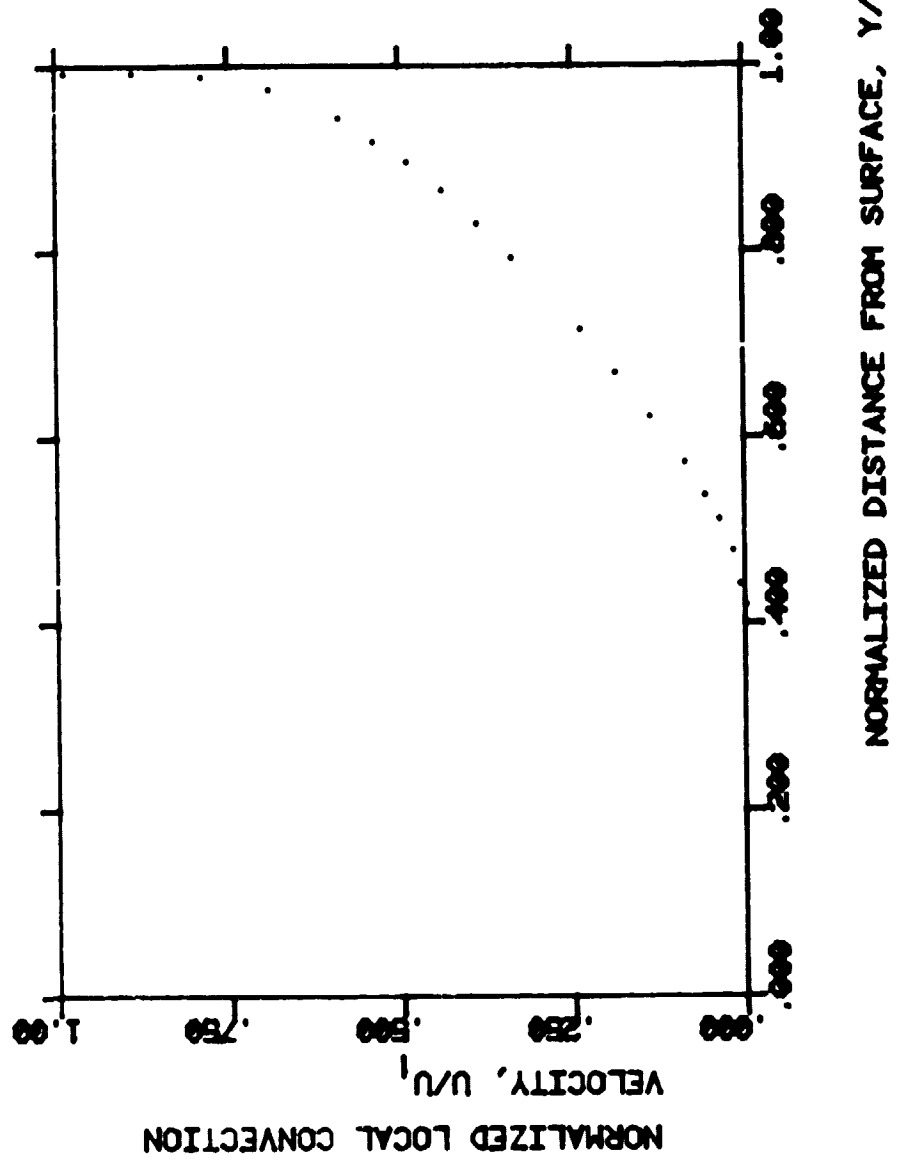


Figure 4.1 A typical boundary layer profile just upstream of trailing-edge obtained by plotting local convection velocity U normalized on U_1 at the edge of the boundary layer (U_1) against distance y from the plate normalized on y at the edge of the boundary layer (y_1).

of a typical boundary layer profile), the parameters local velocity U_1 at the edge of the boundary layer, displacement thickness $\delta^* = \int_0^\infty (1-U/U_1) dy$, momentum thickness $\theta = \int_0^\infty U/U_1 (1-U/U_1) dy$, and form factor $H = \delta^*/\theta$ were then obtained.

The skin friction coefficient $c_f = \tau_w/(1/2\rho U_1^2)$, where $\tau_w = \mu(\partial U/\partial y)_{wall}$ is the shear stress at the wall, was then obtained by using the universal similarity law for the logarithmic part of the viscous region²¹ in the form

$$\log_{10} \left(\frac{U}{U_1} \right) = 4.9 \log_{10} \left(\frac{U_1 y}{v} \right) + 5.9, \quad (4.21)$$

see Figure 4.2 for a nomogram with different values of c_f . (The constants "4.9" and "5.9" in the equation 4.2 are those due to Bradshaw for a flat plate boundary layer.⁷) Although the boundary layer on a NACA 0012 airfoil near the trailing-edge is in an adverse pressure gradient (see Figure 4.3²⁴) it is nevertheless felt that the use of the flat plate (zero pressure gradient) formulation will give consistent values of c_f for the range of Reynolds numbers of the tests. From c_f the wall friction velocity $U^* = (\tau_w/\rho)^{1/2}$ could then be obtained.

The above boundary layer parameters are tabulated in Table 4.1 for various values of the upstream velocity U_∞ with the airfoil at 0° angle-of-attack. Appendix 11.1 contains extensive tabulations and

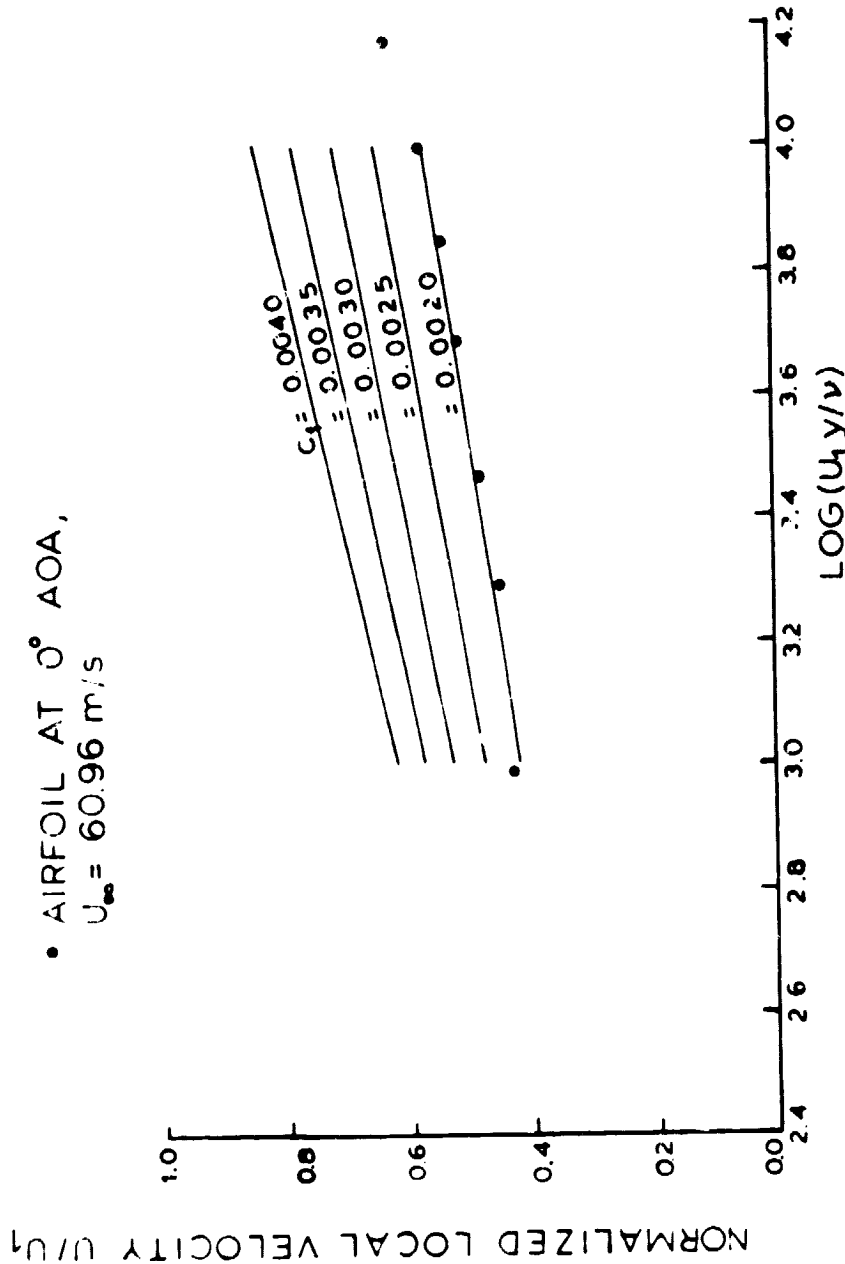


Figure 4.2 A nomogram of the log law (equation 4.2) for different values of c_f . (Here U is the local velocity, U_1 is the local velocity at the edge of the boundary layer, y is the distance from the plate and v is the kinematic viscosity.)

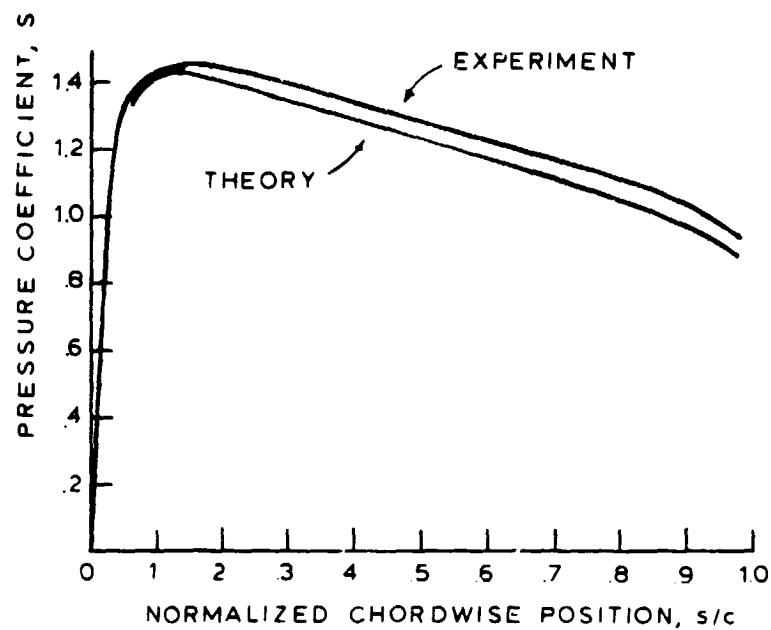


Figure 4.3 The pressure distribution about a NACA 0012 airfoil from the NACA Wartime Report.²⁴ The quantity S as defined in the text is proportional to the static pressure at a given chordwise position s (normalized on total chord length c).

Table 4.1 Boundary layer parameters for the NACA 0012 airfoil at 0° angle-of-attack from boundary layer rake measurements. Rake at 0.238 cm from trailing-edge and 2.54 cm from airfoil centerline.

U_∞ m/s	V_1 m/s	c_f	U^* m/s	τ_w N/m ²	δ^* cm	θ cm	H
22.86	21.06	0.00225	0.7064	0.5964	0.4274	0.2748	1.566
38.10	35.45	0.00215	1.1623	1.6146	0.4003	0.2641	1.516
45.72	42.79	0.00200	1.3533	2.1890	0.4063	0.2702	1.503
53.34	50.14	0.00200	1.5855	3.0051	0.4079	0.2730	1.498
60.96	57.45	0.00200	1.8169	3.9457	0.4005	0.2678	1.496

plots of these boundary layer parameters for 0°, 5°, and 10° angle-of-attack.

4.2 Boundary Layer Preston Tube Measurements

As a further check on the "log law" determination of c_f , pressure measurements were taken on the surface of the airfoil by use of a Preston tube of 0.127 cm diameter. The empirical law for the wall stress τ_w corresponding to the equation 4.2 takes the form

$$\log_{10} \frac{\tau_w d^2}{4\rho v^2} = -1.353 + 0.875 \left[\frac{(p - p_s)d}{4\rho v^2} \right] \quad (4.3)$$

where d is the diameter of the Preston tube, ρ is the fluid density, v is the kinematic viscosity, and where the static pressure p_s corresponds to the pressure on the surface of the airfoil. The parameters wall stress τ_w , friction velocity U^* , and skin friction coefficient c_f are tabulated in Table 4.2 for various values of the upstream velocity U_∞ for the particular case of the Preston tube at midspan, 0.238 cm from the trailing-edge. (A more complete tabulation with plots for chordwise positions of 0.238 cm, 2.54 cm, and 22.86 cm occurs in Appendix 11.2). These results are in close agreement with the measurements of c_f determined from the "log law" and velocity profiles.

In addition, it is known that the uniformity with span of the skin friction coefficient is a good check on the closeness to two-dimensionality of the flow. Thus Preston tubes were attached at

Table 4.2 Boundary layer parameters for the NACA 0012 airfoil at 0° angle-of-attack obtained from Preston tube measurements at 0.238 cm from the trailing-edge on the airfoil centerline.

U_∞ m/s	τ_w N/m ²	U^* m/s	c_f
22.86	0.7371	0.7803	0.0027
38.10	1.8667	1.2418	0.0024
53.34	3.5277	1.7069	0.0023
68.58	5.5380	2.1388	0.0022

spanwise positions at 0.238 cm from the trailing-edge. Plots of Preston tube readings for 0°, 5°, and 10° angle-of-attack are shown in Figure 4.4 where it is seen that the flow is reasonably two-dimensional over the entire region of the span where measurements were taken, except close to the sideplates where the sideplate boundary layers are present.

4.3 Comparison of the Mean-pressure Distribution Around the Airfoil with Previous Data

The measurement of the boundary layer properties included the determination of the local velocity U_1 at the edge of the boundary layer. This allowed for the coefficient $S = (U_1/U_\infty)^2$ proportional to the value of the static pressure on the surface of the airfoil to be determined for the station 0.238 cm upstream of the trailing-edge and compared with previous results²⁴ at much higher Reynolds number. The close agreement for this station on the airfoil centerline can be seen in Figure 4.5. It is felt that this comparison and agreement is very important in view of the geometry of the experiment in which an airfoil was immersed in a rectangular jet in a large, but still finite-sized room. The agreement demonstrates that the static pressure in the vicinity of the trailing-edge was indeed established by the airfoil static pressure distribution arising from the flow around the airfoil and not by any confinement effects due to the room. The physical inference from this result is that any unsteady trailing-edge condition described by the measurements described in this work are not influenced

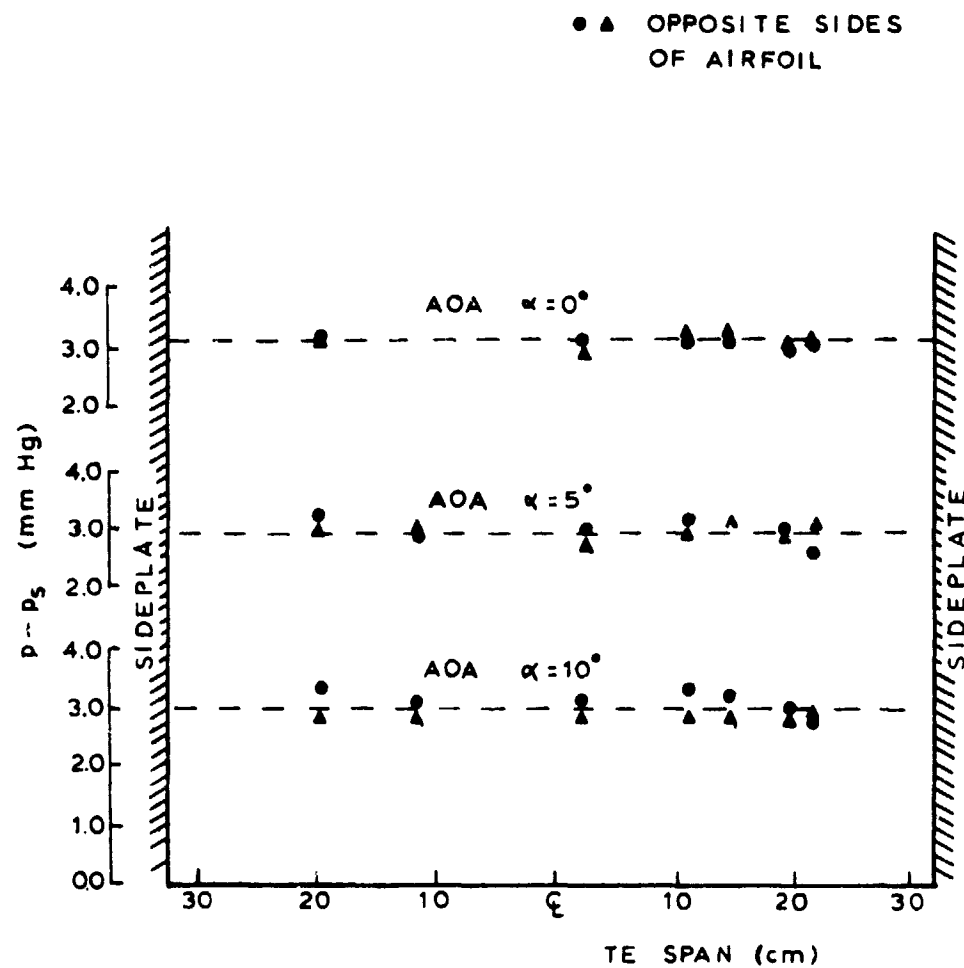


Figure 4.4 Demonstrator of two-dimensional flow. The two-dimensionality of the flow near the trailing-edge is demonstrated here by the reasonable uniformity of the pressure quantity ($p - p_s$) across the span. Here p is the Preston tube pressure at 0.238 cm from the trailing-edge and p_s is the static pressure on the surface of the airfoil. Two-dimensionality is demonstrated for angles-of-attack (AOA) $\alpha = 0^\circ, 5^\circ, 10^\circ$.

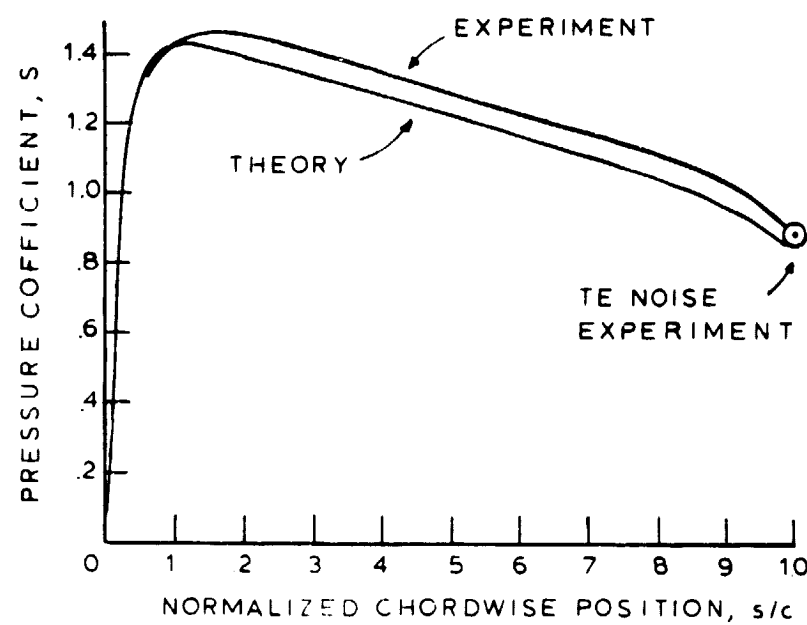


Figure 4.5 Airfoil pressure distribution. The close agreement between the predicted static pressure distribution for the airfoil²⁴ and the value determined from the experiment \odot can be seen in this plot of the pressure proportional quantity S against chordwise position s (normalized on total chord length c).

by any confinement effects of the room through some back effect on the trailing-edge by the wake flow.

5. THE ACOUSTIC FARFIELD AND SOUND POWER LAW

5.1 Farfield Spectrum and Phase and the Power Law

In a detailed examination of the properties of the sound field of the trailing-edge noise phenomenon, both the spectrum and phase characteristics of the farfield pressure fluctuations were examined. In addition, the variation of the mean-square sound pressure with upstream velocity U_∞ was examined and then compared to the fifth power prediction of equation 2.1.

Typical spectrum and phase plot of the sound field, obtained by the cross-spectrum technique described earlier, are presented in Figure 5.1. It should be noted that the sound pressures on opposite sides of the airfoil are 180° out-of-phase over the frequency region corresponding to the trailing-edge noise. As seen in Figure 5.2, the addition of bluntness to the sharp trailing-edge configuration results in an additional "hump" in the spectra which can be attributed to discrete Strouhal-type vortex shedding. Also the effect of increasing the upstream velocity U_∞ which increases the level of the sound spectrum of the trailing-edge noise may be observed.

A quantitative measure of this effect of the flow velocity upon the mean-square sound pressure levels results from a summation of the levels in all the frequency bands corresponding to the trailing-edge noise. These overall sound pressure levels (SPL) are plotted against upstream velocity U_∞ for both the sharp and the blunt trailing-edge case in Figure 5.3, for the measurement position of $r = 1.22$ m and

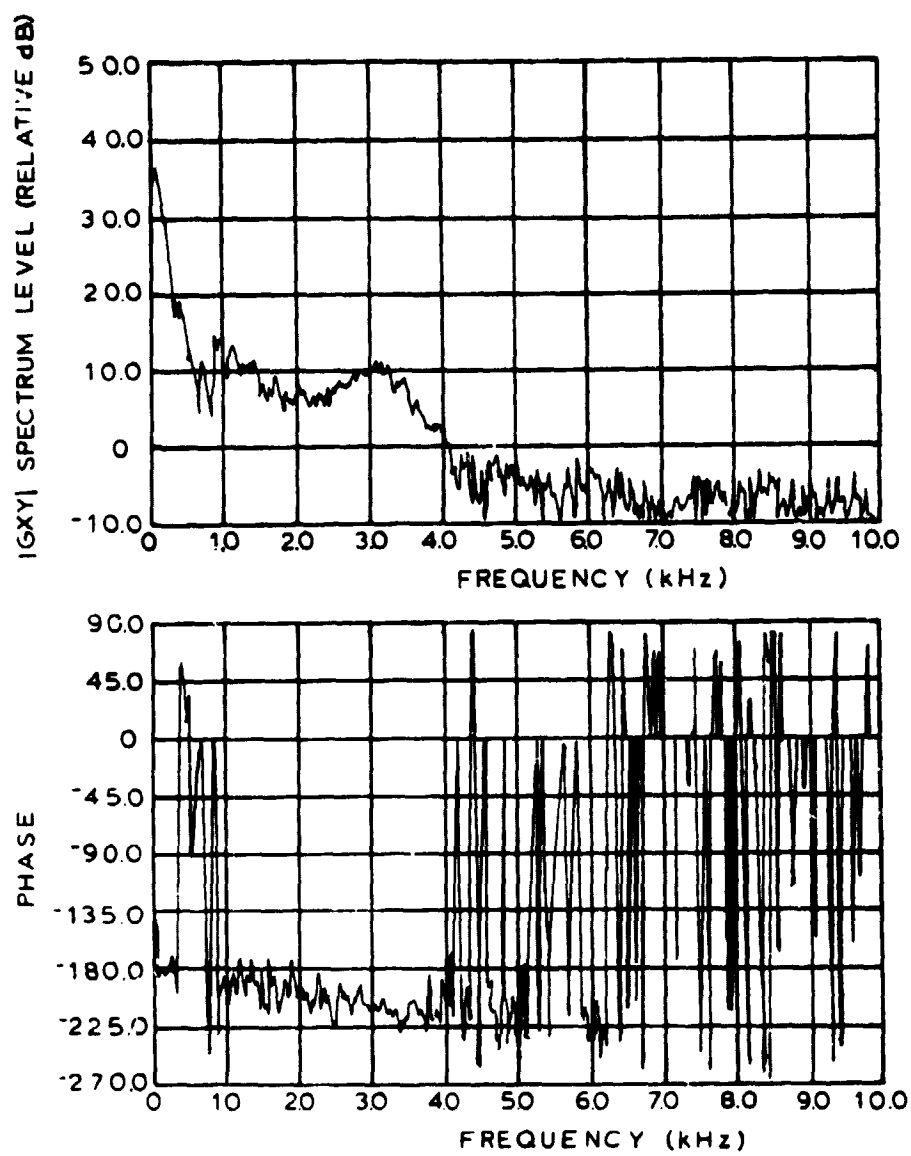


Figure 5.1 A typical spectrum and phase plot of the trailing-edge noise sound field as obtained by cross-spectrum techniques (shown here for the blunt trailing-edge case).

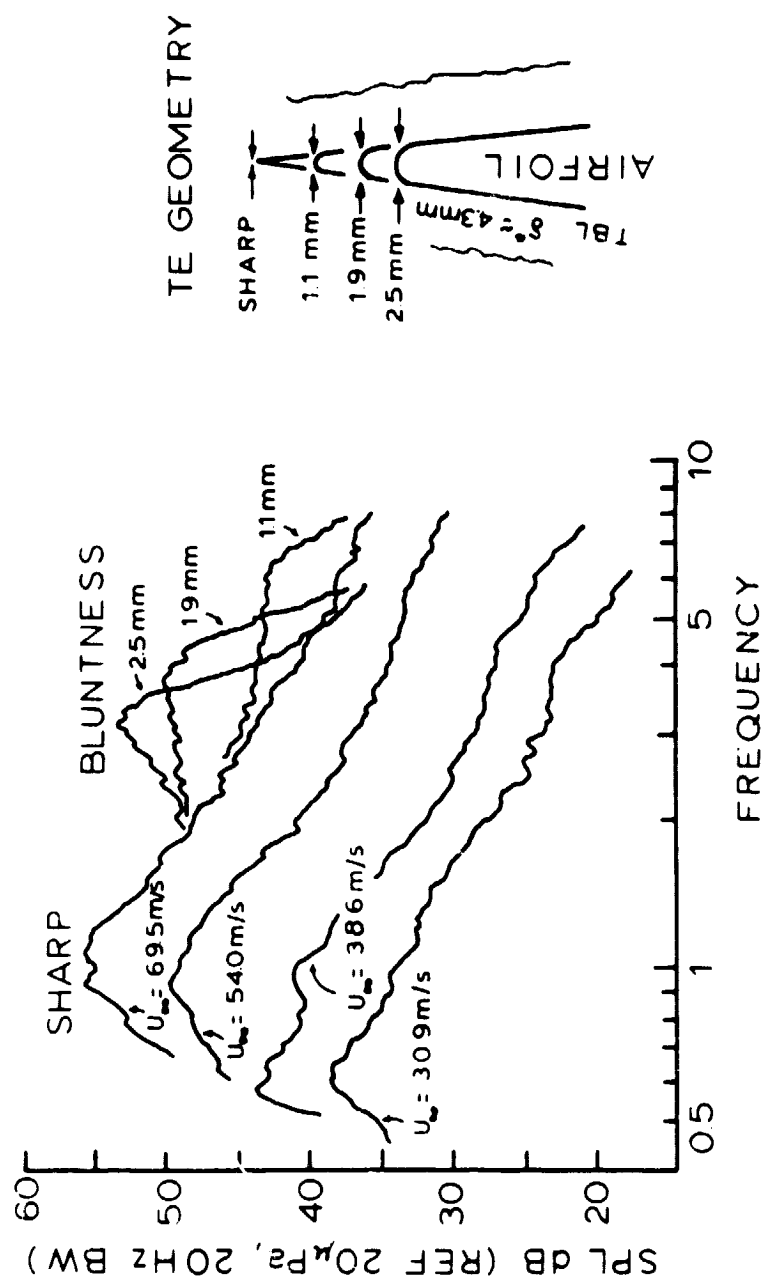


Figure 5.2 Sharp trailing-edge spectra at various upstream velocities U_{∞} are shown along with the additional hints in the spectra resulting from the addition of bluntness to the edge.

angle $\bar{\theta} = 90^\circ$ (for geometry, see Figure 3.1). As shown, the mean-square sound pressure varies as $U_\infty^{5.3}$ for the blunt and $U_\infty^{5.07}$ for the sharp case (where the exponent is determined by the slope of the logarithmic plot). Note that the higher power dependency of the blunt trailing-edge over that of the sharp trailing-edge can be attributed to the contribution from the Strouhal shedding which follows a $U_\infty^{6.0}$ power dependency characteristic of a point source radiator such as a circular cylinder.

The spectral "collapse" of Figure 5.4 provides a check of the validity of the power law, shown here for the particular case of the blunt trailing-edge. The spectral values of the sound pressure have been normalized by dividing by $U_\infty^{5.3}$. As can be seen, these values roughly coalesce, as they should if the 5.3 power law is indeed valid.

The above power law determinations inherently neglect Reynolds number effects and assume a constant relationship between convection velocity V of the eddies at the trailing-edge and the upstream velocity U_∞ . To incorporate both of these effects in the power dependencies resulting from this simplified view, the Ffowcs Williams and Hall equation 2.1 for the mean-square sound pressure $\langle p^2 \rangle$ may be rewritten (without explicit reference to angular dependencies) as

$$\langle p^2 \rangle = \rho_0^2 v^2 V^2 M_v \left(\frac{L_f}{R} \right)^2 = \left(\frac{\rho_0}{a_0} \right) \left(\frac{v}{U_\infty} \right)^2 \left(\frac{U_\infty}{U} \right)^2 U_\infty^2 v^3 \left(\frac{L_f}{R} \right)^2$$

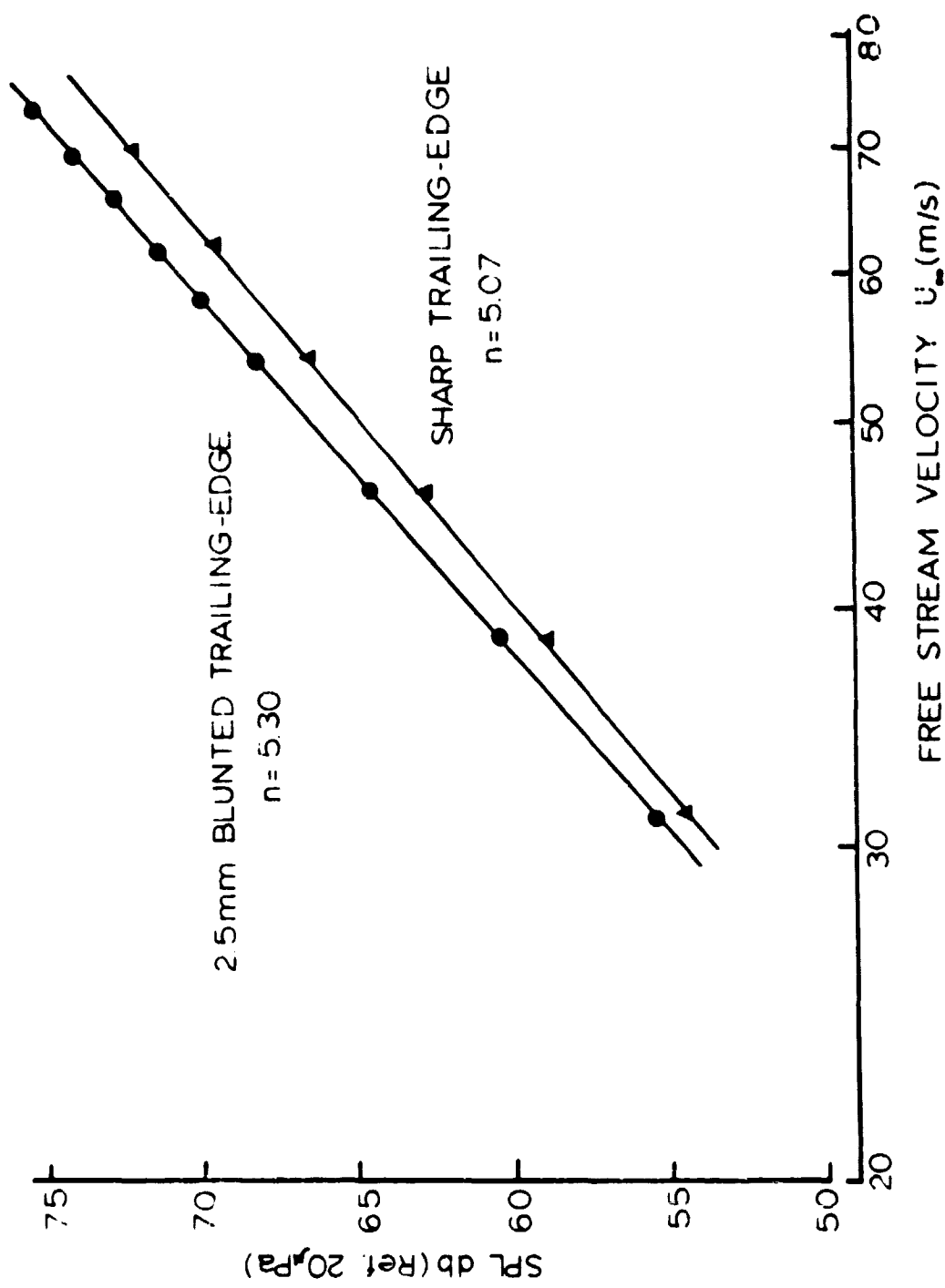


Figure 5.3 The variation in the overall sound pressure level (SPL) with upstream velocity U_{∞} . The mean-square sound pressure varies as U_{∞}^n where $n = 5.07$ for the sharp case and $n = 5.30$ for the blunt case.

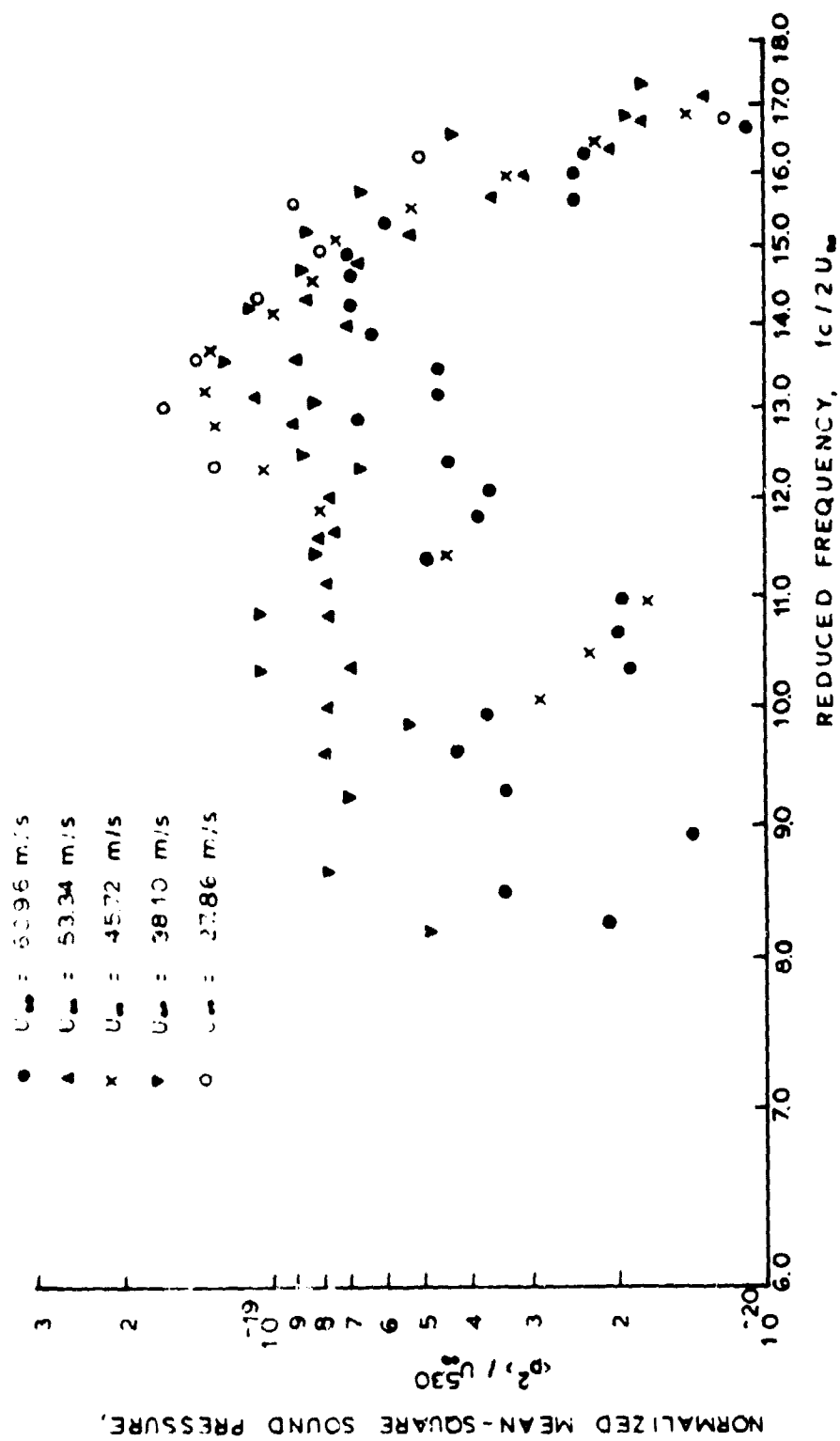


Figure 5.4 Spectral collapse. A spectral collapse obtained by plotting mean-square sound pressure $\langle p^2 \rangle$, normalized on upstream velocity U_∞ to the 5.3 power demonstrates the validity of the 5.3 power law as a function of "reduced" frequency $f_c/(2U_\infty)$ where c is the chord length.

$$= \left(\frac{\rho_0}{a_0} \right)^2 \left(\frac{v}{U^*} \right)^2 \left(\frac{U^*}{V_\infty} \right)^2 \left(\frac{U_\infty}{V} \right)^2 \left(\frac{L_t}{R} \right)^2 v^n \quad (5.1)$$

where ρ_0 is the fluid density, a_0 is the speed of sound, v is the fluctuating turbulent velocity, U^* is the friction velocity, U_∞ is the upstream velocity, L is the span length of the airfoil, t is a spanwise turbulence scale, R is the distance of the observer from the trailing-edge, and the exponent $n = 5$. Here the fluctuating velocity v normal to the surface and nondimensionalized by the friction velocity U^* is known to be relatively constant for a wide range of Reynolds numbers.²¹ Now by incorporating the range of measured values of U^*/U_∞ for the tests from Table 4.1, the power law dependence on the eddy convection speed can be calculated.

These calculations showed that the small change in U^* for the range of the experiment would increase the exponent n of equation 5.1 by 0.23 while the small change in measured convection velocity V would reduce n by 0.33. The net change in the exponent n would therefore be $\Delta n = 0.23 - 0.33 = -0.10$, so that the mean-square sound pressure scales on the convection velocity V following from equation 5.1 as $V^{4.97}$ for the sharp case and as $V^{5.2}$ for the blunt case. Thus there would seem to be excellent agreement between theory and experiment for the sharp case where the corrected experimental value of $n = 4.97$ is extremely close to the predicted value of $n = 5.0$.

As a calibration check on the methodology and accuracy of the above sound pressure level measurements and power law determinations, an independent check was made using a rod of 0.9525 cm diameter spanning

the rectangular jet in place of the airfoil. The acoustic emission of the rod is a pure tone with a frequency corresponding to the Strouhal number of the periodic shedding of the separated flow. Also, because of its small diameter relative to the sound wavelength, the rod behaves very nearly as a point dipole source. The measured mean-square sound pressure was found to depend upon the 6.0 power of the flow velocity (see Appendix 10.3) which is indeed in agreement with theory⁶ for such a source.

5.2 The Effect of the Kutta Condition Result on the Absolute Level of the Mean-square Sound Pressure

Turning to the absolute level of the mean-square sound pressure, a comparison may be made between the no-Kutta result of equation 2.1 and the measured levels of the experiment. The relationship between the mean-square sound pressure $\langle p^2 \rangle$ (at $r = 1.22$ m and $\bar{\theta} = 90^\circ$) and the upstream velocity U_∞ may be written for the experiment as

$$\langle p^2 \rangle = K U_\infty^n \quad (5.2)$$

where n has been shown to equal 5.07 for the sharp trailing-edge and where K is determined for this case from Figure 5.3 as
 $K = \langle p^2 \rangle / U_\infty^{5.07} = 2.9 \times 10^{-12}$ so that equation 5.2 becomes

$$\langle p^2 \rangle = 2.9 \times 10^{-12} U_\infty^{5.07} \quad (5.3)$$

in SI units. This relationship may then be compared with the no-Kutta expression 2.1, namely

$$\langle p^2 \rangle = \rho_0^2 v^2 V^2 M_v (\frac{L\ell}{R})^2 \quad (5.4)$$

where ρ_0 is the density of the fluid, v is the fluctuating velocity, V is the flow convection speed, M_v is the Mach-number based on V , L is the span length of the plate, ℓ is a spanwise turbulence scale, and R is the distance of the observer from the trailing-edge. Now equation 5.4 can be rewritten as

$$\langle p^2 \rangle \approx (0.55)^3 \frac{\rho_0^2}{a_0} \left(\frac{v}{U_\infty}\right)^2 \left(\frac{L\ell}{R}\right) U_\infty^5 = K U_\infty^5 \quad (5.5)$$

where $K = 1.5 \times 10^{-9}$ using typical turbulence levels (that is, $v/U_\infty = 0.04$ for a flat plate²¹), $\ell \sim \delta^*$, and $v = 0.55 U_\infty$ so that equation 5.5 becomes

$$\langle p^2 \rangle \approx 1.5 \times 10^{-9} U_\infty^5 \quad (5.6)$$

at $R = 1.22$ and $\bar{\theta} = 90^\circ$. Thus the experimental result for $\langle p^2 \rangle$ of equation 5.3 has an absolute value which is 1.9×10^{-3} times the theoretical prediction of equation 5.6. This much lower measured value is presumably due to the real viscous conditions at the trailing-edge unaccounted for in the no-Kutta prediction formula. It should be noted that this much lower measured result is in qualitative agreement with

the prediction of the two-eddy model of Howe whereby a Kutta condition is incorporated as a $(1-W/V)^2$ factor of reduction in the no-Kutta prediction. As shown later, this model would indeed suggest a lower predicted level of the radiated sound when the quantities wake convection velocity W and convection velocity V on the surface of the airfoil are supplied. (Strictly, however, in the real experimental situation with two wetted surfaces it could be argued that the interpretation of the experimental values of V and W are not directly related to the two-eddy model of Howe.)

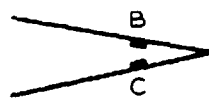
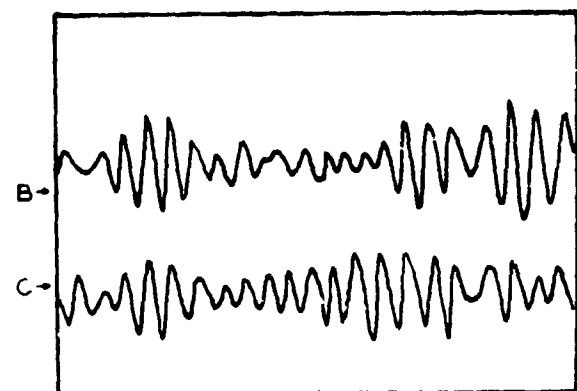
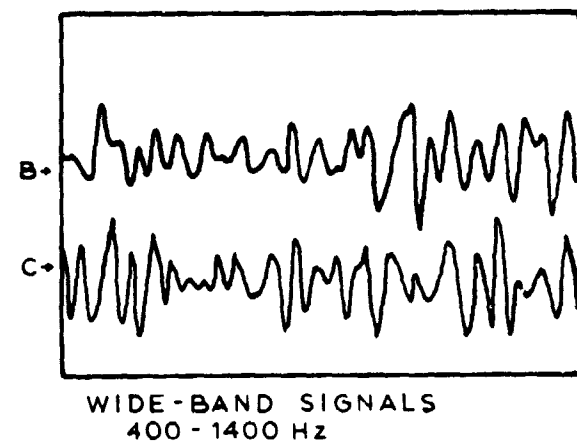
Of course, basic to any application of theoretical Kutta condition prediction schemes is an understanding and detection of the actual phenomenon involved. While understanding that the Kutta condition is a mathematical step to remove a singularity in potential flow theory which does not occur in real flows because of the presence of viscosity is straightforward, the physical connection between the Kutta condition and the viscous case in unsteady flows is, however, less readily understood. It is often proposed in the literature that a measurement of a zero pressure differential at the trailing-edge constitutes a physical detection of the phenomenon. (It should be noted here that the use of the description Kutta condition seems to have "crept" into the physical description of the real flow. From hereon it is proposed that the description trailing-edge condition be used when referring to the real viscous flow case.) See for example Fleeter,¹⁰ where the condition of zero pressure differential at the trailing-edge and satisfaction of the Kutta condition are equated. Such a condition has no real significance for a sharp trailing-edge, however, since it

surely must be the case that in the limit as a single point in space is approached from two directions, the pressure differential there is identically zero in the absence of a finite width wake. For this experiment, simultaneous surface pressure time signatures have been captured for measurement positions near the edge of the sharp trailing-edge airfoil (see Figure 5.5) which indicate that the upper and lower pressures there do indeed appear to tend toward the same value (that is, one function of time) as the edge is approached. However, to interpret this as an indication of satisfaction of the Kutta condition is misleading since zero pressure differential is an altogether necessary requirement for the flow at a sharp trailing-edge in the absence of a wake of finite width.

Thus the Kutta condition must be considered as a mathematical tool for removing singularities in potential flow formulations and not as a "requirement" to be met by real flows.

5.3 Scaling

The level of the measured trailing-edge noise when scaled to compare with jumbo-jet aircraft such as the Boeing 747, in the "clean" configuration with flaps and landing gear retracted in flyover is of extreme practical importance in noise reduction efforts since the trailing-edge noise is likely to be quite important when the wingspan is very large. Two approaches can be taken in an effort to scale the model results: (1) scaling on wing area as suggested by Shaw²² and (2)



B AND C : PRESSURE SENSOR LOCATIONS, 2 mm FROM TRAILING-EDGE.

Figure 5.5 Opposing trailing-edge surface pressure signals. Instantaneous wide band (a) and narrow band (b) signals from surface pressure transducers on opposite sides of the airfoil near the trailing-edge indicate that upper and lower pressures tend to one value at the edge ($U_{\infty} = 69.5 \text{ m/s}$).

scaling on the wingspan L and displacement thickness δ^* proportional to the spanwise turbulence scale ℓ as suggested by equation 2.1.

To scale on wing area, the mean-square sound pressure $\langle p^2 \rangle$ for the model from equation 5.3 may be normalized on wing area S and separation distance r as

$$\langle p^2 \rangle = 2.9 \times 10^{-12} \times \frac{S_{747}}{S_{\text{model}}} \times \left(\frac{r_{\text{model}}}{r_{747}} \right)^2 \times U_{\infty}^{5.07} \quad (5.7)$$

in SI units.

Therefore the mean-square sound pressure for the model of 0.2787 m^2 total surface area at a distance $r = 1.22 \text{ m}$, when scaled to a Boeing 747 of 658.4 m^2 total wing area at $r = 152 \text{ m}$ traveling at 100 m/s , becomes $\langle p^2 \rangle = 6.0 \times 10^{-3} (\text{Pa})^2 \approx 71.7 \text{ dB}$.

In a similar manner, the experimental trailing-edge noise level of the model may be scaled on wingspan L and displacement thickness δ^* to the Boeing 747 by rewriting equation 5.3 in the form

$$\langle p^2 \rangle = 2.9 \times 10^{-12} \times \frac{(L \times \delta^*)_{747}}{(L \times \delta^*)_{\text{model}}} \left(\frac{r_{\text{model}}}{r_{747}} \right)^2 \times U_{\infty}^{5.07}. \quad (5.8)$$

If a 1/7th power law is assumed for the turbulent boundary layer growth²¹ over the wing, then $\delta = 0.37 R_N^{-1/5} x$. Since the Reynolds number of the Boeing 747 wing is 7.54×10^7 based on chord length $x = 10.92 \text{ m}$ at a flight speed of 100 m/s , this gives $\delta = 10.74 \text{ cm}$ and $\delta^* \approx \delta/8 = 1.34 \text{ cm}$. Therefore the mean-square sound pressure of the model at a distance $r = 1.22 \text{ m}$ with $\delta^* = 0.396 \text{ cm}$ and

$L = 0.457 \text{ m}$ scales to the Boeing 747 traveling at 100 m/s at $r = 152 \text{ m}$ with $\delta^* = 1.34 \text{ cm}$ and $L = 59.64 \text{ m}$ by equation 5.8 to give $\langle p^2 \rangle = 1.14 \times 10^{-3} (\text{Pa})^2 \approx 64.6 \text{ dB}$.

Thus trailing-edge noise levels of 71.7 and 64.6 dB are predicted at a distance of 152 m from a Boeing 747 traveling at a flight speed of 100 m/s in "clean" flyover configuration (flaps and landing gear retracted) when the mean-square sound pressure levels of the model are scaled on wing area and $L \times \delta^*$, respectively. This contrasts with full-scale data of Hardin¹³ for the Boeing 747 in the "clean" flyover configuration with engines throttled giving a level of 85 dB at this flyover speed and distance. It can therefore be seen that trailing-edge noise falls some 15-20 dB below the total body noise from jumbo-jet aircraft and thus it would appear that other effects, such as three-dimensional flow effects, are more significant contributors to the total airframe body noise from these aircraft.

This much lower result for the trailing-edge noise is also demonstrated by the use of a composite curve of body noise levels compiled for "clean" aircraft (flaps and landing gear retracted) and normalized on the parameter $\delta b/r^2$ by Fink⁹ where δ is the boundary layer thickness, b is the span length, and r is the observer distance. On this plot,⁹ see Figure 5.6, there are two data points for the trailing-edge noise experiment. One data point () results from normalization of the measured level of the mean-square sound pressure on the measured value of $\delta = 2.29 \text{ cm}$ obtained from the boundary layer profile in Appendix 11.1 for upstream velocity $U_\infty = 69.5 \text{ m/s}$. At this value of upstream velocity (equivalent to 135.1 Knotts) the

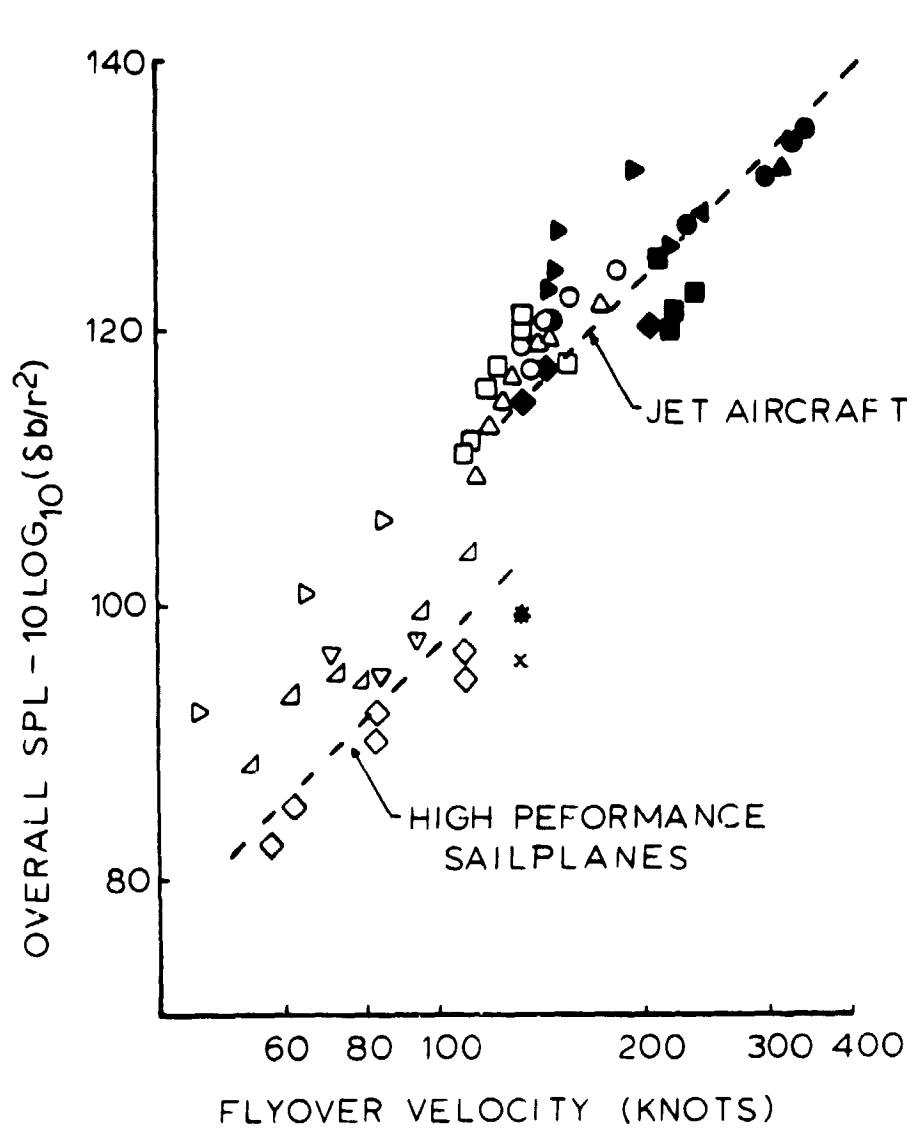


Figure 5.6 Sound pressure levels (SPL) for various aircraft normalized on the parameter $\delta b/r^2$ by Fink,⁹ where δ is the boundary layer thickness, b is span length, and r is the observer distance. Trailing-edge noise levels for the experiment, when plotted on either a measured value of δ (x) or a calculated value of δ (\bullet), fall well below the line corresponding to jet noise, but near sailplane data.

trailing-edge noise sound pressure level (SPL) was 72.2 dB (from Figure 5.3) at a distance r of 1.22 m for a span b of 0.4572 m, which gave $SPL - 10 \log_{10} (\delta b/r^2)$ equal to 95.9 dB.

A second data point () in Figure 5.6 results from the normalization of the measured level of the mean-square sound pressure on a calculated value of the boundary layer thickness $\delta = 1.27$ cm. With respect to this calculated value of δ , it should be noted that the data compiled by Fink used a flat-plate boundary layer calculation for δ based on the 1/7th power law for the velocity distribution according to the formula (equation 21.8, Schlichting²¹)

$$\delta = 0.37 \left(\frac{S}{b}\right) \left(\frac{U_\infty}{v}\right)^{-0.2} \quad (5.9)$$

where the ratio of the wing area S to the span b is the mean geometric chord. Using equation 5.9 the boundary layer thickness is calculated to have the value $\delta = 1.27$ cm for the upstream velocity $U_\infty = 69.5$ m/s which, proceeding as before, gives the sound pressure level $SPL - 10 \log_{10} (\delta b/r^2)$ equal to 99.7 dB in Figure 5.6. (Note that 3 dB has been added to the measured data in order to compare with the full-scale data where the measuring microphone incorporated a 3 dB ground reflection effect.)

Thus it can be seen in Figure 5.6 that trailing-edge noise, using either the measured or the calculated value of δ , falls well below the line corresponding to jet aircraft, in agreement with earlier results. This then suggests that two-dimensional trailing-edge noise is not a dominant factor in present noise reduction efforts related to these

large-bodied aircraft. However, two-dimensional trailing-edge noise scales near the measured sailplane data of Figure 5.6 which would be expected for such high aspect ratio (high span to chord length ratio) aerodynamically clean aircraft. Thus a lower bound has been established, set by two-dimensional flow conditions, which does establish an ultimate limit to noise reduction efforts related to jumbo-jet aircraft.

5.4 Directivity

A determination of the character of the directivity pattern of the measured trailing-edge noise is important for comparison with and confirmation of theory, but it is also of great practical importance in determining the actual annoyance effects of the radiated sound upon airport environments.

The theoretical relationship for the mean-square sound pressure variation with "flyover" angular position $\bar{\theta}$ (see Figure 5.7) of the observer as described before is generally taken to be the $\sin^2(\bar{\theta}/2)$ law of Ffowcs Williams and Hall.⁸ However, Goldstein,¹² in an alternative derivation which incorporated the effects of a sheared mean flow, predicted the variation in mean-square sound pressure $\langle p^2 \rangle$ with angular observer position $\theta = \pi - \bar{\theta}$ (see Figure 5.7) as

$$\langle p^2 \rangle \sim \frac{\cos^2(\theta/2)}{[1 - M_V(\cos \theta)(1 - M_O \cos \theta)]^2} \quad (5.10)$$

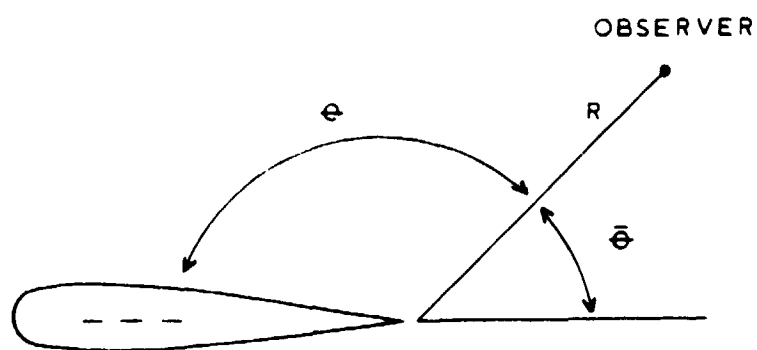


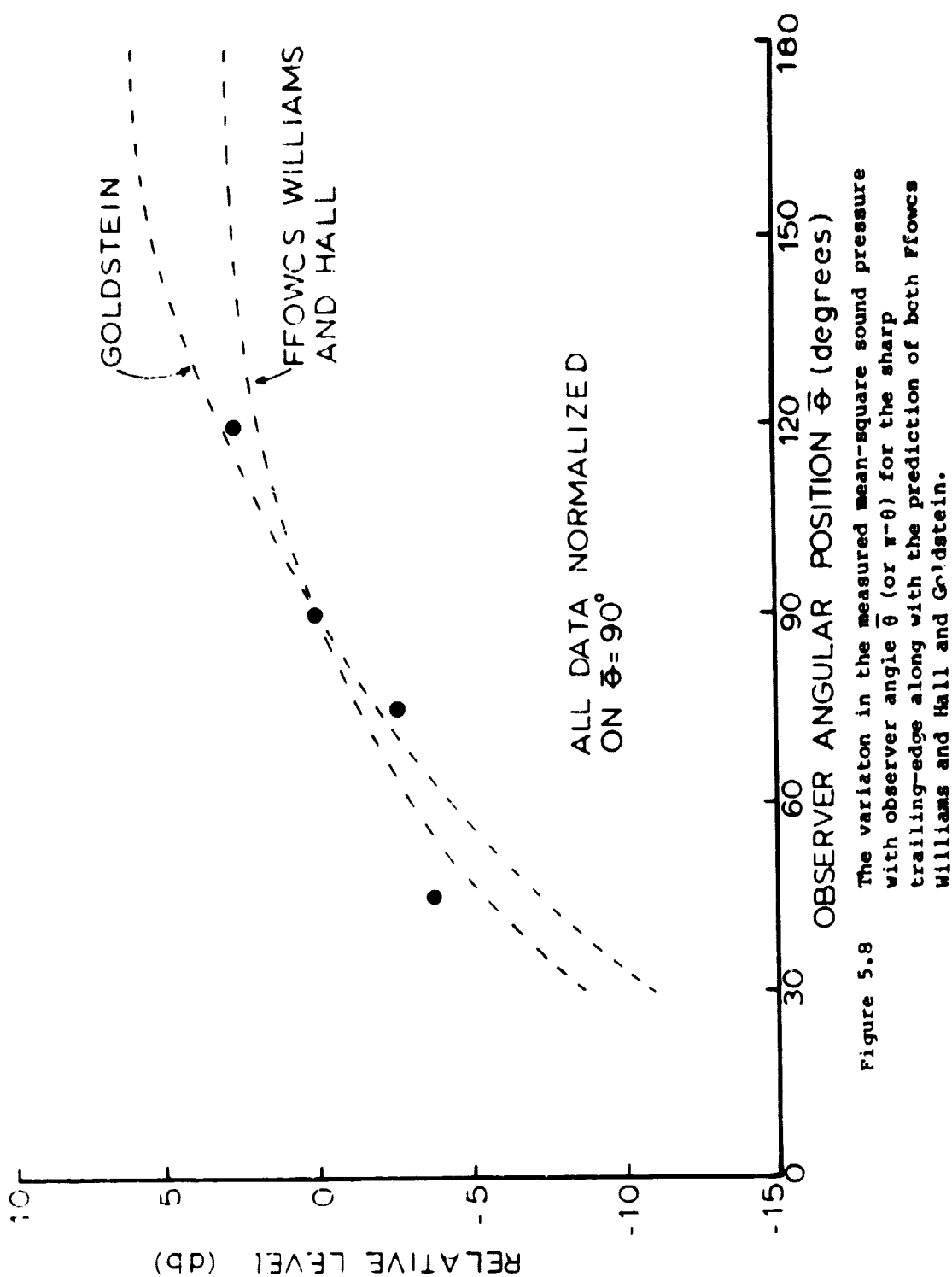
Figure 5.7 The observer angles $\bar{\theta}$ of Ffowcs Williams and Hall⁸ and θ of Goldstein¹² are shown. ($\theta = \pi - \bar{\theta}$).

where M_v is the Mach number based on the convection velocity V and M_o is the Mach number based on upstream velocity U_∞ . Then at the upstream velocity of 69.5 m/s equation 5.10 gives the angular dependence as

$$\langle p^2 \rangle \sim \frac{\cos^2(\theta/2)}{[(1-0.111 \cos \theta)(1-0.202 \cos \theta)]^2} \quad (5.11)$$

where again $\theta = \pi - \bar{\theta}$. However, it should be noted that at low Mach numbers the result 5.11 tends to a $\cos^2(\theta/2)$ dependence upon the angle θ which is identically equivalent to the Ffowcs Williams and Hall $\sin^2(\bar{\theta}/2)$ dependence upon the angle $\bar{\theta}$, since $\theta = \pi - \bar{\theta}$. Thus the two formulations reduce to the same $\sin^2(\bar{\theta}/2)$ law at sufficiently low Mach numbers.

For comparison with these theoretical predictions, the directivity pattern of the mean-square sound pressure was determined for the case of the upstream velocity $U_\infty = 69.5$ m/s by again using the cross-spectra technique described earlier. The edge-noise levels are normalized on the level at $\bar{\theta} = \theta = 90^\circ$ and are plotted as a function of angular position $\bar{\theta}$ (equal to $\pi - \theta$) in Figure 5.8 for the sharp trailing-edge. Also plotted are the angular variations in noise levels predicted by both the Ffowcs Williams and Hall and the Goldstein formulations. An inspection of Figure 5.8 reveals that the measured data falls close to the predicted results of both formulations -- "both" formulations since for this low Mach number (0.2) case the two theories



ORIGINAL PAGE IS
OF POOR QUALITY

never differ by more than approximately 1 dB for the range of angles of the experiment.

Therefore the mean-square sound pressure of the trailing-edge noise can be said to follow a $\sin^2(\theta/2)$ directivity law for the low Mach numbers of the experiment and thus equation 2.1 is again seen to provide an accurate description of the trailing-edge noise sound field.

6. THE SURFACE PRESSURE FIELD

6.1 Spectrum of the Surface Pressure Field

Since the source of the trailing-edge noise arises from the changes in time of the unsteady surface pressure field as the turbulent boundary layer flow approaches the trailing-edge, a detailed study of the surface pressure field in the vicinity of the trailing-edge is in order.

As mentioned earlier the surface pressure was measured with specially designed Kulite pressure transducers. Due to the finite diameter of the pressure sensitive area of the transducer there is a limit to the high-frequency response. It is now well known that for large values of the transducer diameter d the ratio of d to the displacement thickness δ^* is important. In this case the surface pressure spectra may be plotted on the Stouhal number $\omega\delta^*/U_1$, where ω is the angular frequency and U_1 is the local mean velocity at the edge of the boundary layer. But it is also known for relatively small transducer diameters, namely $d \ll$ boundary layer thickness δ , that the upper limit on resolution occurs for turbulent pressure fluctuations arising from the wall similarity region of the boundary layer close to the wall. The properties of this region scale on the parameter v/U^* where U^* is the friction velocity and v is the kinematic viscosity. Thus the ratio of d to v/U^* is a measure of the high frequency resolution of the transducer. A curve corresponding to a zero value of the parameter $d(U^*/v)$ has been given by Bull¹ for this high frequency

part of the surface pressure spectrum in terms of a wall frequency Strouhal number $(\omega/U^*)(v/U^*) = (\omega v)/U^{*2}$. The value of the parameter $d(U^*/v)$ for the Kulite transducer with $d = 0.0254$ cm can be obtained from Table 4.1 for U^* and ranged over values of 12 to 32 for the mean velocity range of the tests. From Bull's results¹ (taken for zero pressure gradient), at the worst case of $d(U^*/v) = 32$ for the upper frequency limit of 20 kHz corresponding to $(\omega v)/U^{*2} = 0.55$ the transducer would read some 2 dB too low. However it should be noted that the dominant energy of the pressure field and acoustic field is in the 1-4 kHz range, see Figures 6.1 and 5.1, where the error from Bull's curve corresponding to frequency $(\omega v)/U^{*2} = 0.055$ ($f = 2$ kHz, say) would be negligible.

It should be noted that the absolute value of the measured pressure levels are higher than the zero pressure gradient case (see Figure 6.2) possibly due to the influence of the adverse pressure gradient. However the trend of the curves for this experiment follows that of the zero pressure gradient results so that it would seem that the Kulite transducer was indeed capable of detecting high-frequency pressure fluctuations with excellent resolution.

Thus measurements of the fluctuating surface pressure at the trailing-edge of the airfoil were obtained for both the "blunt" and "sharp" trailing-edge geometries (see Figure 6.1 for a typical spectrum taken for the "blunt" case). It should be recalled that the trailing-edge noise theories predict that the far-field sound results from these pressure fluctuations near the edge of the airfoil. Therefore a more thorough characterization of the surface pressure

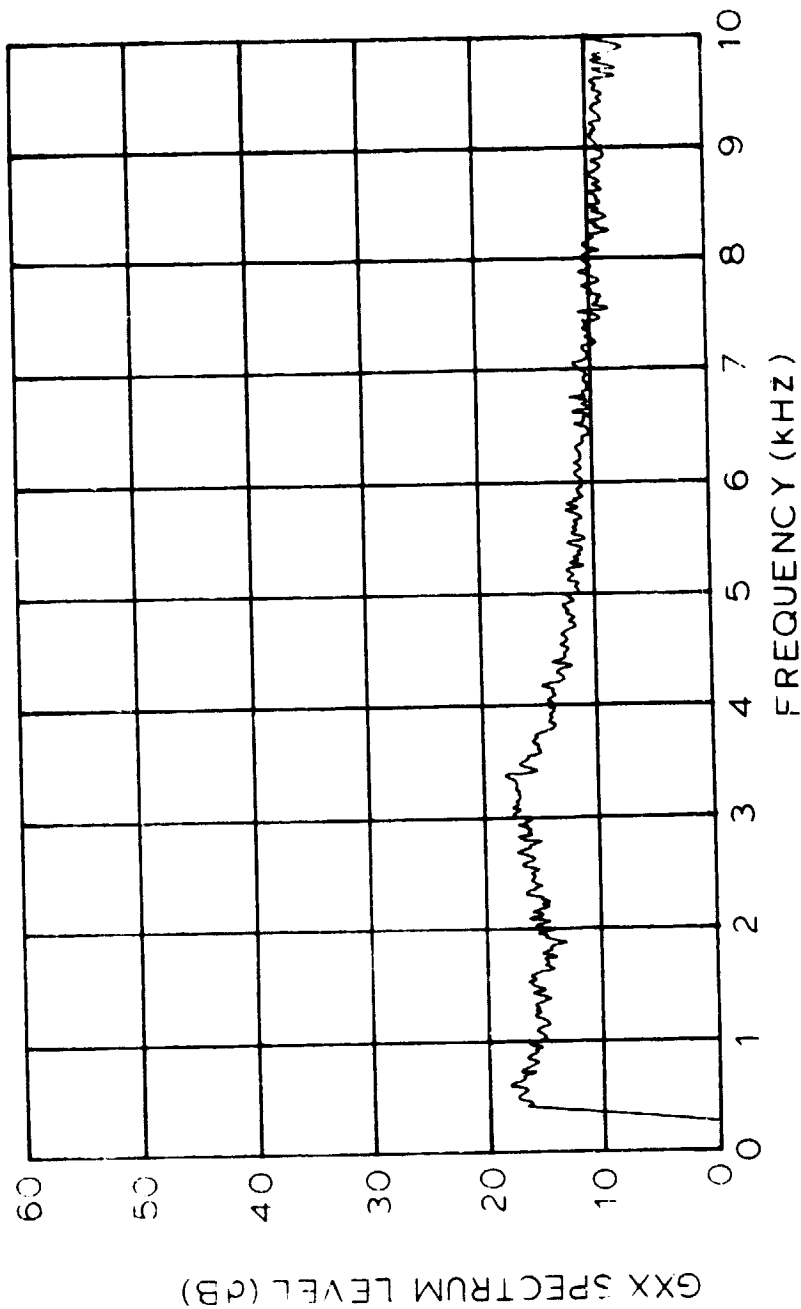


Figure 5.1 A typical trailing-edge surface pressure spectrum for the blunt trailing-edge case ($U_\infty = 69.5 \text{ m/s}$).

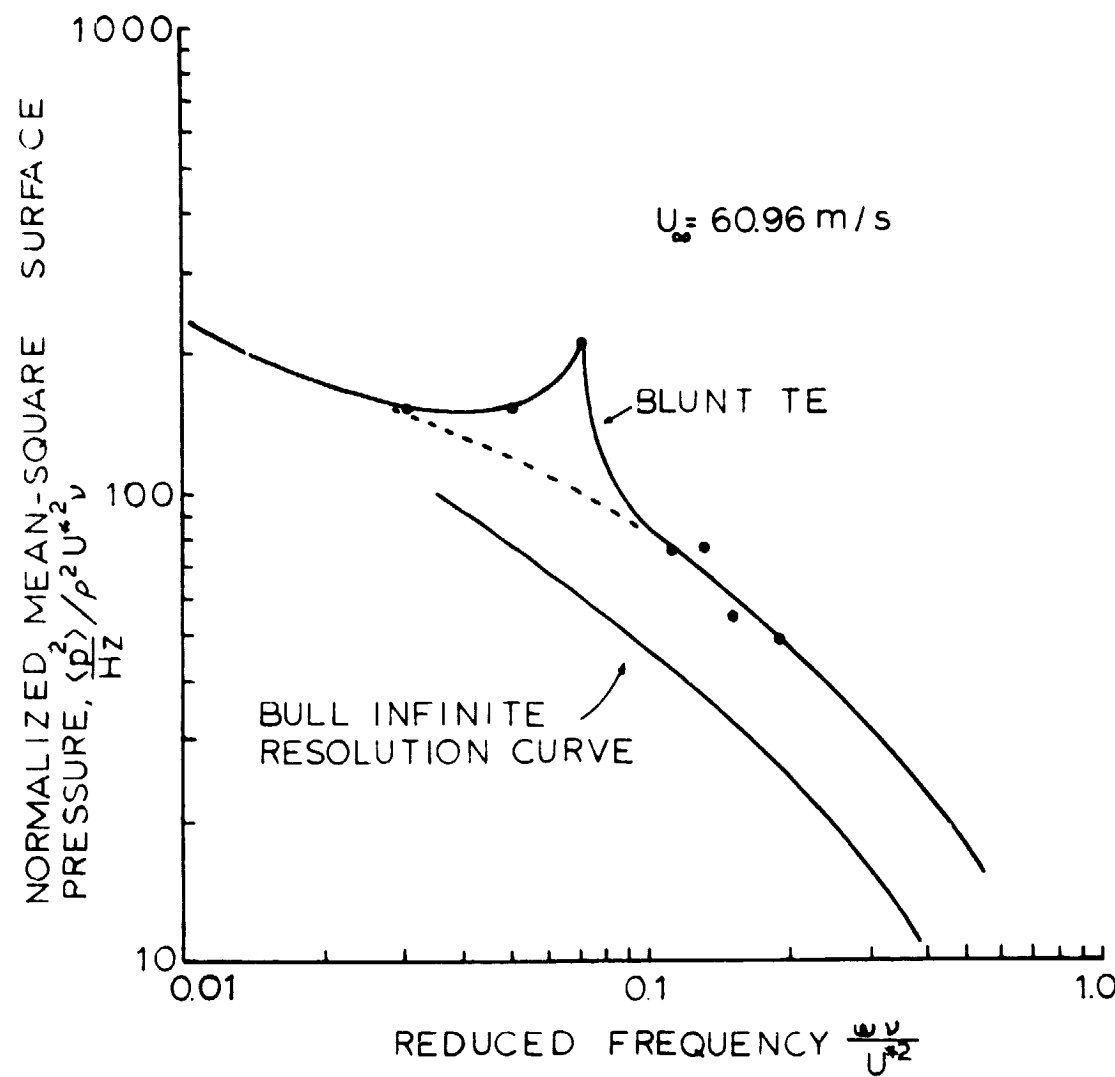


Figure 6.2 Mean-square surface pressure normalized on U^{*2} plotted against the reduced frequency parameter wv/U^{*2} along with the Bull's infinite resolution curve for determination of high frequency response (U^* is the friction velocity).

field, including phase properties of the field and changes that occur in the field as it approaches the trailing-edge, should result in a better understanding of the mechanism of trailing-edge noise production especially with respect to the "scattering" mechanism mentioned earlier.

6.2 Phase of the Surface Pressures at the Trailing-edge

From simultaneous measurements of the fluctuating pressure by the Kulite transducers in the proximity of the trailing-edge the phase angle between pressure transducers on opposite sides of the airfoil was found to exhibit three phase regions: in-phase, 180° out-of-phase, and non-correlated (for example, see Figure 6.3 for the blunt case). When the parameter $f\xi$, where f is a boundary frequency between any two of the frequency regions and ξ is the distance of the surface pressure measurement position from the trailing-edge, is plotted against ξ , Figure 6.4 results. This plot indicates that the value of $f\xi$ at the boundary between in-phase and out-of-phase regions remains close to a finite value, namely 7 Hz-m for all ξ near the edge. Therefore as the trailing-edge is approached, that is $\xi \rightarrow 0$, then the presence of this dividing boundary is such that $f \rightarrow \infty$ which implies that the surface pressures on opposite sides of the airfoil are in-phase at the trailing-edge ($\xi=0$) for all frequencies of interest, in concurrence with earlier results of section 5.2 (see Figure 5.5). Thus the pressure loading Δp is such that $\Delta p \rightarrow 0$ as the trailing edge is approached.

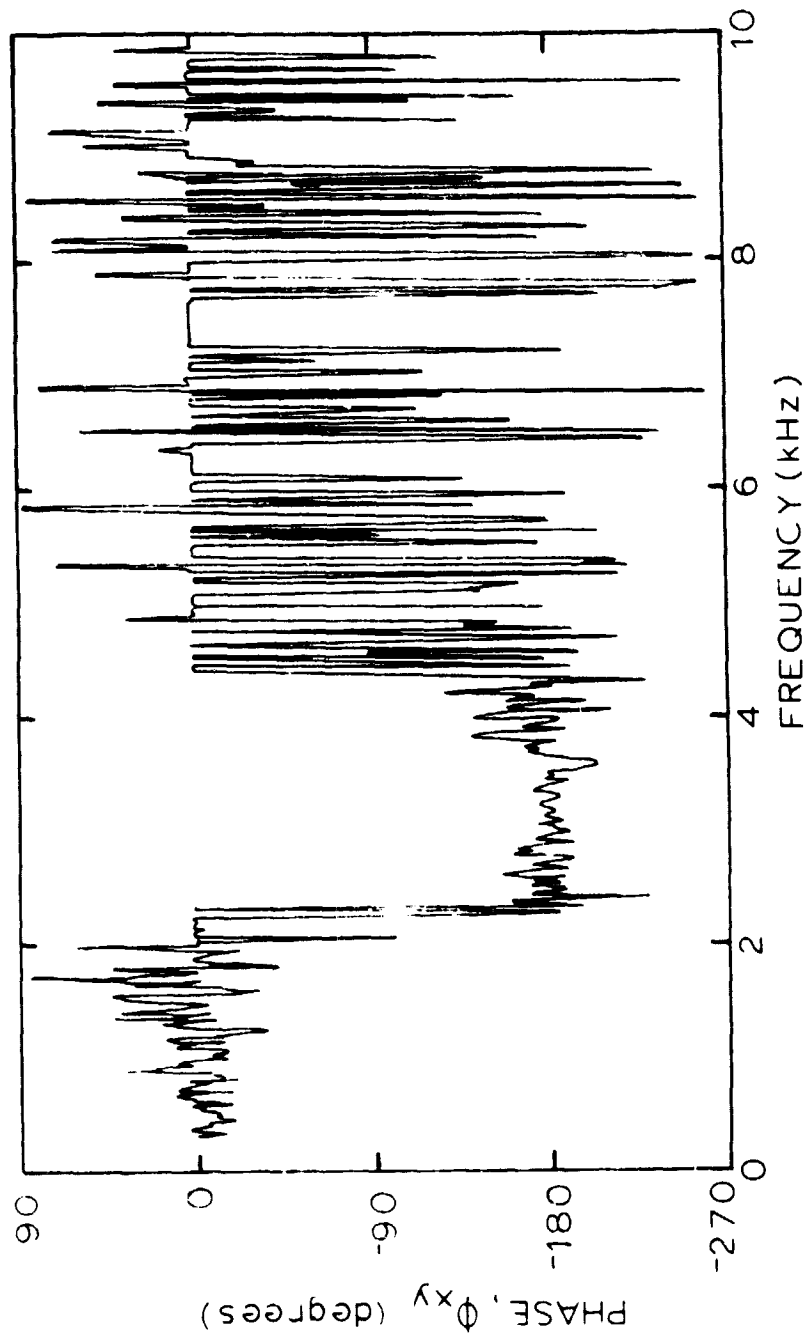


Figure 6.3 Surface pressure phase. This example of the phase between surface pressure transducers on opposite sides of the airfoil exhibits the three phase regions found at the trailing-edge: in-phase, 180° out-of-phase, and non-correlated.

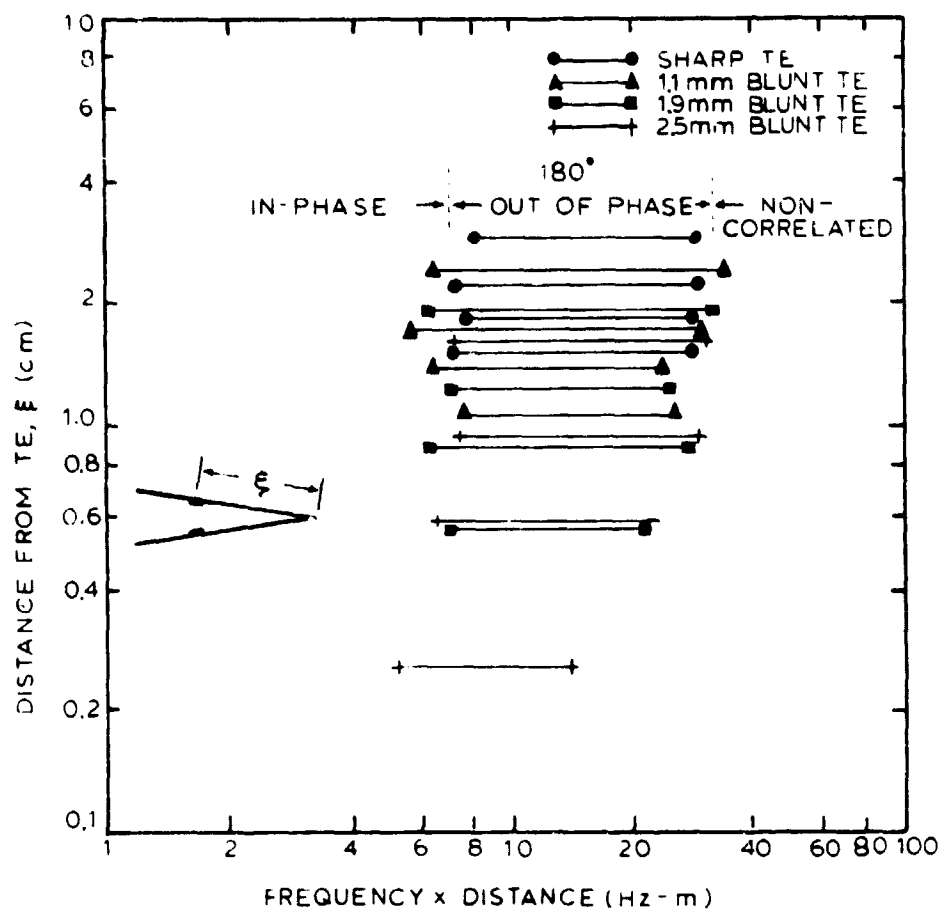


Figure 6.4 The frequency parameter $f\xi$, where f is a boundary frequency between any of the three frequency regions of in-phase, 180° out-of-phase, and non-correlated, is plotted against distances from the trailing-edge for various trailing-edge geometries. The in-phase $f\xi$ boundary remains constant as a function of ξ , which indicates that $f \rightarrow \infty$ as $\xi \rightarrow 0$.

6.3 The Scattered Pressure Field

The fact that the phase ϕ_{xy} plots in Figure 6.5 for the sharp trailing edge are approximately linear with frequency implies a pure time shift, so that the slope $\frac{d\phi_{xy}}{df}$ is a measure of the convection speed of the pressure disturbances. This convection speed information was used to detect the scattered field mentioned earlier as follows.

The line ϕ_{BA} has a lower slope than ϕ_{CA} and ϕ_{DA} (the latter slopes being almost equal) with a slope approximately equal to the local field convection speed V . The much higher slopes of ϕ_{CA} and ϕ_{DA} and the fact $\phi_{CA} \approx \phi_{DA}$ can be associated with a very fast convection between points A and C and between points A and D, namely at sonic speed.

Thus a disturbance passing the upstream point A on the upper side, say, sweeps downstream to B at V of order U_∞ , but there is also a component of the field at A, the sound field created by the disturbance, which travels at sonic speed. This sound field travels around the trailing-edge and upstream on the lower side passing by C and D. Thus components of the "scattered" field of the trailing-edge noise have been detected for the sharp trailing-edge case in agreement with the predictions of theory. (Also the decaying nature of this field is demonstrated by the falling values of $|G_{xy}|$ in Figure 6.5.)

In the case of the blunt trailing-edge, however, this "scatter" phenomenon may be masked by an additive local pressure field resulting from the structured Strouhal vortex shedding mentioned earlier.

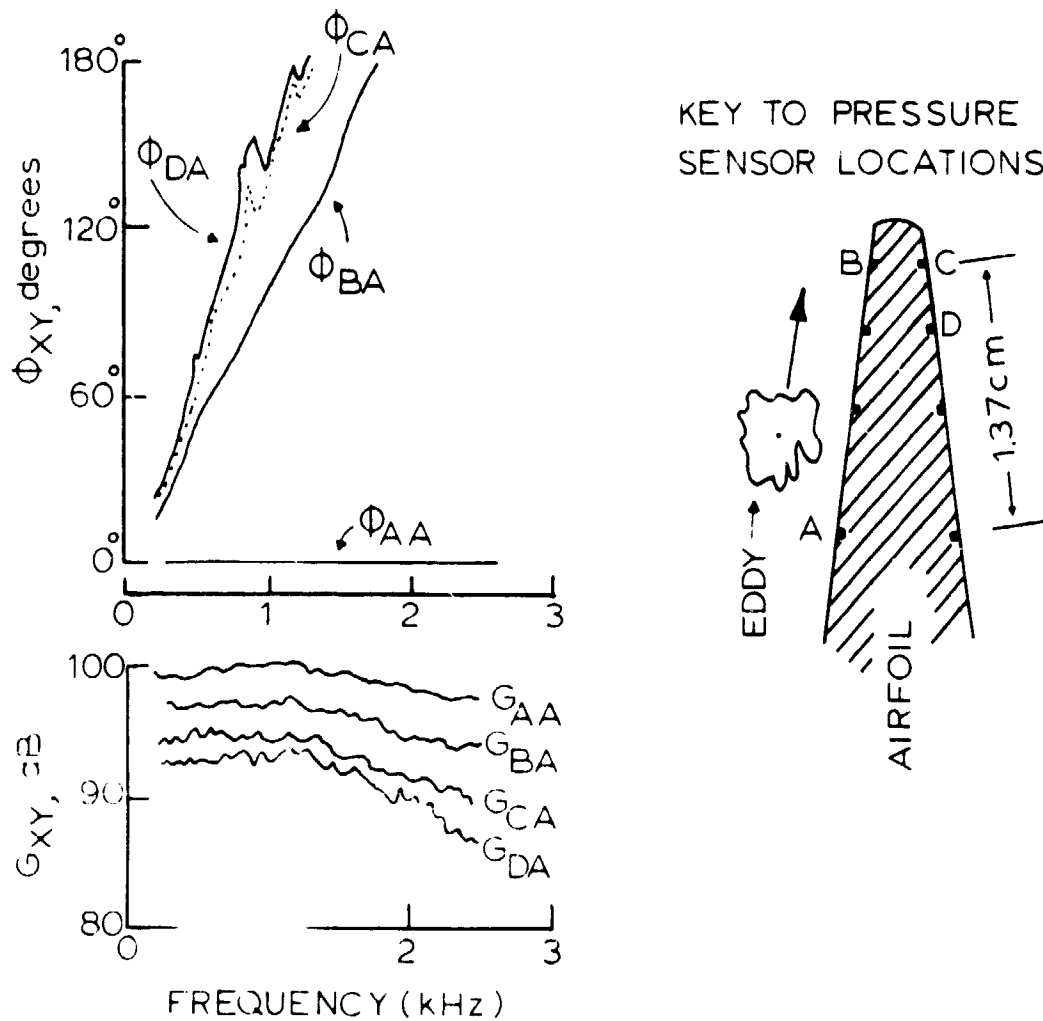


Figure 6.5 Variation of phase ϕ_{xy} and cross-spectrum level $|G_{xy}|$ for various combinations of trailing-edge surface transducers x and y used to determine eddy convection speed.

Evidence that this additional pressure field is indeed due to a Strouhal type phenomenon is provided by Figure 6.6. Here the signals from four pressure transducers, two Kulite surface pressure transducers at the trailing-edge of the airfoil and two microphones on opposite sides of the airfoil at the 90° position (see diagram in Figure 6.6), have been used to obtain the cross-spectrum between a surface pressure difference signal resulting from the simultaneous subtraction of the two Kulite surface pressure signals and a farfield sound difference signal resulting from the simultaneous subtraction of the two microphone sound pressure signals. Thus this simultaneous subtraction of both surface pressures and sound pressures produced an enhancing additive effect, which suggests that the surface pressures and sound pressures were 180° out-of-phase on opposite sides of the airfoil, as is typical of structured Strouhal vortex shedding.

It seems, therefore, that the sound field of the blunt trailing-edge results from both the structured Strouhal vortex shedding and the trailing-edge noise "scatter" mechanism measured for the sharp trailing-edge. This is in agreement with the results of Section 5.1 (Figure 5.2).

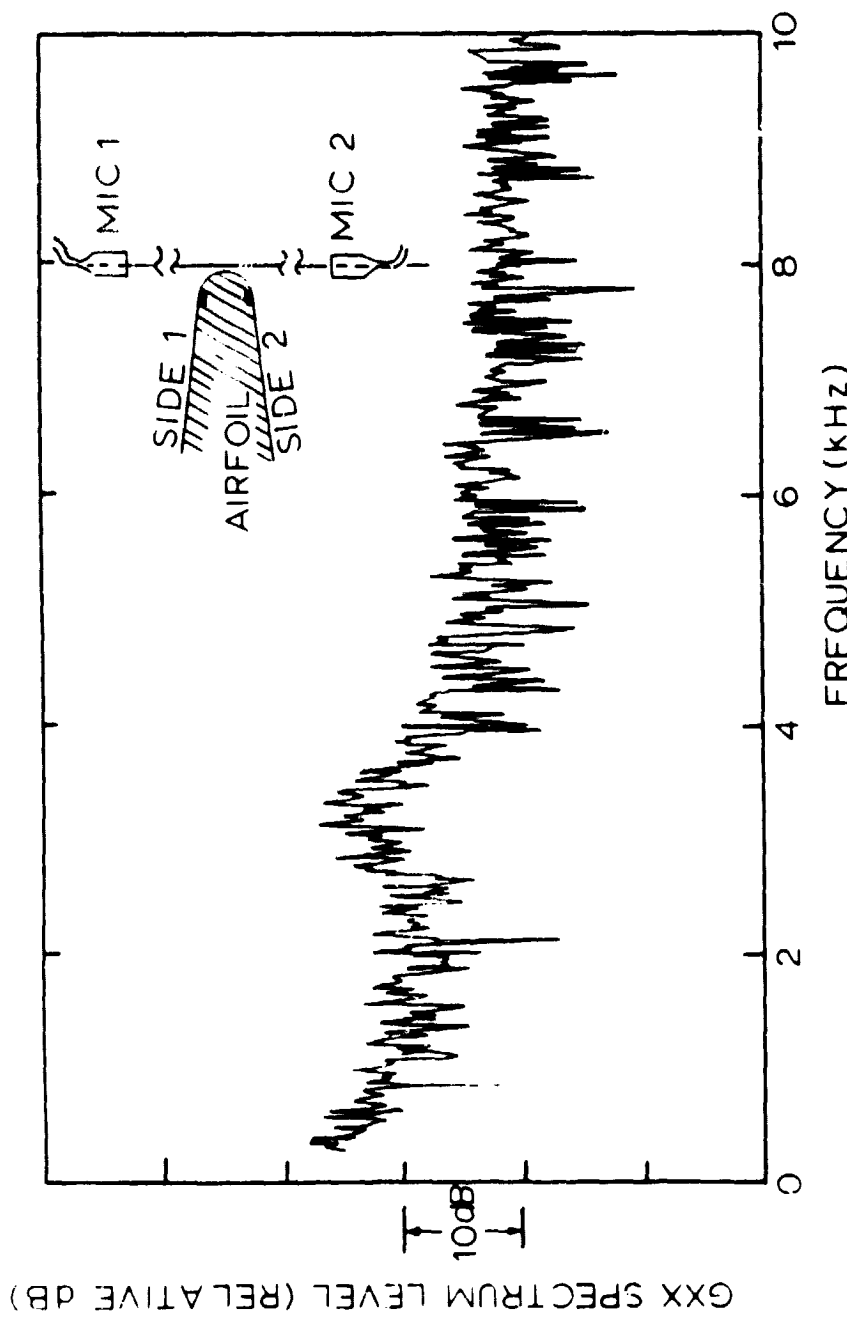


Figure 5.6 A four pressure transducer cross-spectrum plot resulting from the cross-spectrum between a surface pressure difference signal (resulting from the simultaneous subtraction of two opposing Kulite surface pressure signals) and a farfield sound difference signal (resulting from the simultaneous subtraction of two opposing microphone sound pressure signals).

7. WAKE CONVECTION SPEED AND COMPARISON WITH THEORY

Since the Howe two-eddy model for application of the Kutta condition predicts a value of mean-square sound pressure reduced with respect to the no-Kutta equation 2.1 by a factor of $(1-W/V)^2$, it was important to measure the convection velocity V on the surface of the airfoil and W in the wake.

As described earlier (section 6.3), convection speed measurements of the local pressure field on the airfoil were obtained from the phase data ϕ_{xy} . Near the edge of the airfoil the convection velocity V determined in this manner was found to be approximately 0.55 times the upstream velocity U_∞ .

For similar determinations of the wake convection velocity W , a hotwire probe as described earlier with DC signal proportional to the mean velocity in the wake was employed. Thus phase measurements between a trailing-edge Kulite surface pressure transducer and the hotwire were obtained. A plot of the wake convection velocity determined from these phase plots is seen in Figure 7.1 as a function of distance in the wake past the trailing-edge. With these values of wake convection velocity W and surface convection velocity V at hand, some comments concerning the $(1-W/V)^2$ factor may now be made.

With respect to this $(1-W/V)^2$ factor, mention has already been made of the much more complicated structure of a two-sided boundary layer flow in the vicinity of the trailing-edge as compared with the simple one-sided single or double eddy model of Howe and other workers.

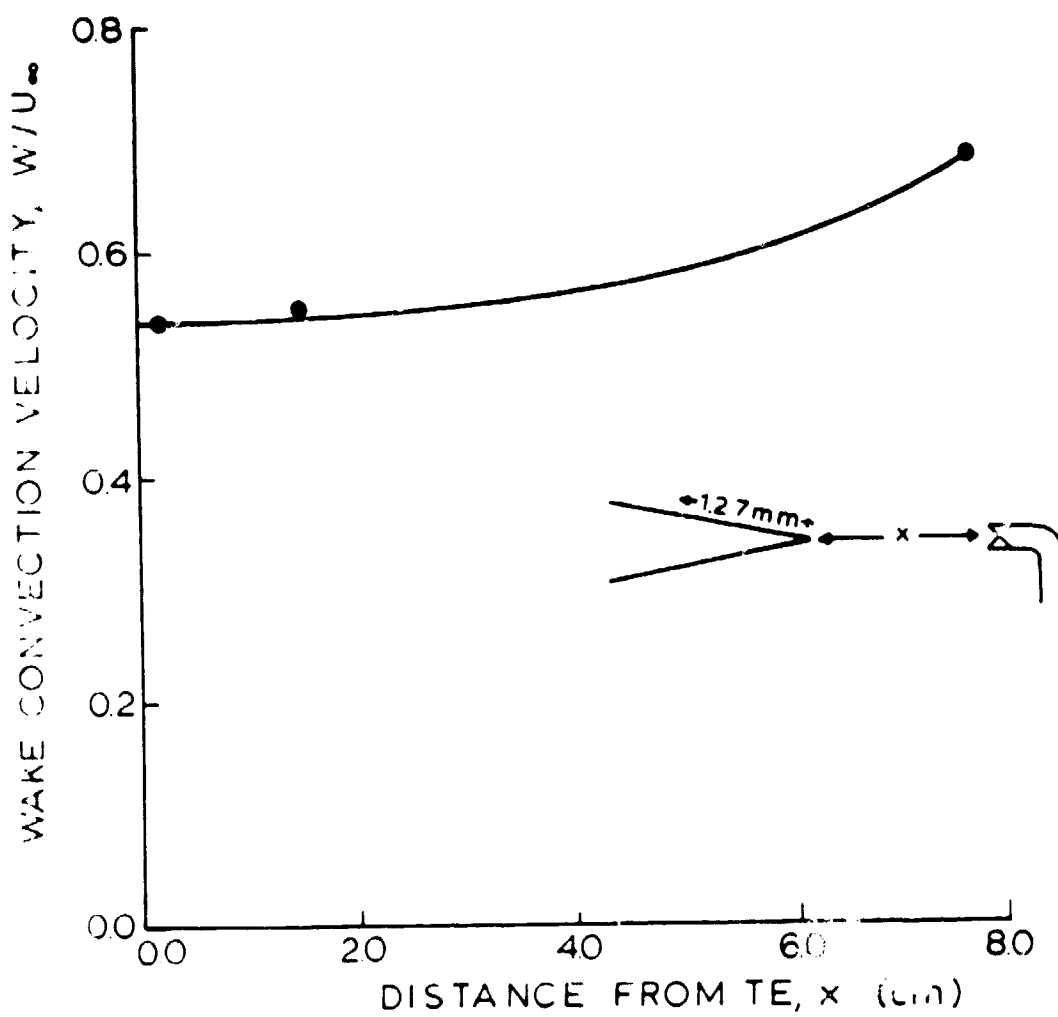


Figure 7.1 A plot of wake convection velocity W normalized on upstream velocity U_{∞} as a function of distance x from the trailing-edge as determined from a trailing-edge Kulite surface pressure transducer and a hotwire probe positioned in the wake.

ORIGINAL PAGE IS
OF POOR QUALITY

If, however, the Howe theory with the Kutta condition is used here with substitution of the appropriate values of the eddy convection speed V for the airfoil and W in the wake, we see from Figure 7.1 for W and from the value of $V = 0.55 U_\infty$ at the trailing-edge that there is a smooth transition from the convection velocity upstream to the convection velocity in the wake so that the factor $(1-W/V)^2$ is zero. That is, as has already been illustrated, the trailing-edge noise would be zero.

Of course, it could be anticipated that since the trailing-edge noise spectrum is due to a distribution of many eddy sizes in a finite sheared region, perhaps the effect of the reduction due to the Kutta condition is much more complicated than with the Howe two-eddy model. This might account for why the measured trailing-edge noise is finite but very much less than the no-Kutta condition theory would predict, see earlier Section 5.2.

5-2

8. DISCUSSION OF THE "CAUSALITY" APPROACH TO SOURCE IDENTIFICATION

The complicated nature of the equations for prediction of aerodynamic noise by shear flows such as turbulent boundary layer flow over a surface has led many workers to examine more simplistic views of the way in which the sound field is "caused" by source distributions. One such viewpoint known as the "causality" postulate has been proposed by Sieddon²³ in which he relates the sound to the surface dipole source strength in terms of the surface pressure field through manipulations of the equation

$$p(x,t) = \frac{x_1}{4\pi x^2 c} \int_S \left[\frac{\partial f_1}{\partial t} \right]_{t,y} ds \quad (8.1)$$

where p is the sound pressure at the observer position x at time t , c is the speed of sound, f_1 is the local resultant stress at each point y on the surface S and $t = t - |x-y|/c$ is the retarded time.

It is well-known, for instance see Lighthill's original work,¹⁷ that formulation of the sound field in terms of the local pressure fluctuations (rather than density) is a very complicated procedure in that identification of the sound in the presence of very strong local "incompressible-type" pressure fluctuations may be analytically and experimentally difficult. This case is no exception since a condition for equation 8.1 is that quadrupole source terms be weak or negligible.

But, here for the trailing-edge noise it is the quadrupole which is being modified by the effect of the edge. Thus the "causality" method is inapplicable and the full sophistication of the Howe, et al. theories must be used in interpreting the measured data.

9. CONCLUSIONS

From this study of the noise radiated by the turbulent flow over a model NACA 0012 airfoil, the following conclusions on the description of the sound pressure field, properties of the local pressure field and the influence of the Kutta condition in theoretical predictions can be made.

1. The mean-square sound pressure level of the trailing-edge noise depends on the upstream velocity U_∞ to the 5.07 power, that is $U_\infty^{5.07}$ for the sharp trailing-edge. Incorporating Reynolds number effects produces a $V^{4.97}$ power law for the mean-square sound pressure scaled on convection velocity V , which closely follows the theoretical prediction of a $V^{5.0}$ power law.
2. When scaled to large-bodied jumbo-jet aircraft in the "clean" configuration (flaps and landing gear retracted), two-dimensional trailing-edge noise is some 15-20 dB below measured sound levels for these aircraft. This suggests that two-dimensional trailing-edge noise is not a dominant factor in present noise reduction efforts related to these large-bodied aircraft. However, the measured two-dimensional trailing-edge noise did scale near full-scale sailplane data. This would be expected for such high aspect ratio (high span to chord length ratio) aerodynamically clean aircraft. Thus a lower bound has been established, set by two-dimensional flow conditions, which does establish an ultimate limit to noise reduction efforts related to jumbo-jet aircraft.

3. The directivity pattern of the trailing-edge noise, as measured for the sharp trailing-edge, follows the predicted $\sin^2(\bar{\theta}/2)$ law for the variation of the mean-square sound pressure with observer angular position $\bar{\theta}$.

4. The mean-square sound pressure levels predicted by no-Kutta theories are higher than the measured levels for the experiment. This finding suggests that it is necessary to apply the Kutta condition in potential flow modeling of the trailing-edge noise problem. In addition, this finding is in qualitative agreement with the Howe formulation of the Kutta condition reduction factor of $(1-W/V)^2$, when the value of convection velocity V on the surface of the airfoil and W in the wake for the experiment are supplied.

5. Surface pressures on opposite sides of the sharp trailing-edge airfoil are in phase over the entire measured spectrum at the trailing-edge and appear to tend to one value (one function of time) as the edge is approached. However, to interpret this as an indication of satisfaction of the Kutta condition is misleading since zero pressure differential is an altogether necessary requirement for the flow at the sharp trailing-edge in the absence of a finite wake. Thus the Kutta condition cannot be viewed as a "requirement" to be met by real flows, but rather as a strictly mathematical tool for removing singularities in potential flow problems.

6. A scattered field has been detected on the surface of the airfoil in the vicinity of the trailing-edge in agreement with current theories.

7. The Siddon "causality" postulate for aerodynamic source identification in its stated form which requires that quadrupole source terms be weak or negligible may not be applied to the trailing-edge noise problem where the influence of quadrupole source terms (undergoing modification by the edge) are important.

10. LIST OF REFERENCES

1. Bull, M. K. and A. S. W. Thomas. 1976. High Frequency Wall-Pressure Fluctuations in Turbulent Boundary Layers. *The Physics of Fluids*, Vol. 19, No. 4, pp. 597-599.
2. Chandramani, K. L. 1974. Diffraction of evanescent waves with Applications to Aerodynamically Scattered Sound and Radiation from Unbaffled Plates. *J. Acoust. Soc. Am.* 55, pp. 19-29.
3. Chase, D. M. 1972. Sound radiated by Turbulent Flow off a Rigid Half-Plane as obtained from A Wavevector Spectrum of Hydrodynamic Pressure. *J. Acoust. Soc. Am.* 52, 1011-1023.
4. Couvall, C. 1976. Langley Presses Noise Reduction Efforts. *Aviation Week*, Vol. 105, No. 24, pp. 63-68.
5. Crighton, D. G. 1972. Radiation from Vortex Filament Motion Near a Half-Plane. *Journal of Fluid Mechanics*, Vol. 51, pp. 357-362.
6. Curle, N. 1955. The Influence of Solid Boundaries on Aerodynamic Sound. *Proceedings of the Royal Society, Series A*, Vol. 231, pp. 505-514.
7. Duncan, T. and A. Young. *Experimental Fluid Mechanics*. Pergamon.
8. Pffowcs-Williams, J. E. and L. H. Hall. 1970. Aerodynamic Sound Generation by Turbulent Flow in the Vicinity of a Scattering Half-Plane. *Journal of Fluid Mechanics*, Vol. 40, Pt. 4, pp. 657-670.
9. Fink, M. R. 1975. Experimental Evaluation of Theories for Trailing Edge and Incident Fluctuation Noise. *AIAA Journal*, Vol. 13, No. 11, pp. 1472-1477.
10. Fleeter, S. 1979. Trailing Edge Conditions for Unsteady Flows at High Reduced Frequency. *AIAA Proceedings* 79-0152.
11. Goldstein, M. 1976. *Aeroacoustics*. McGraw-Hill, New York, New York.
12. Goldstein, M. 1978. *Journal of Fluid Mechanics*, 84(2), pp. 305-29.
13. Hardin, J. C. 1976, Airframe Self-Noise -- Four Years of Research. AGARD-VKI Lecture Series No. 80 on Aerodynamic Noise.
14. Hayden, R. E., Fox, H. L. & R. C. Chanaud. 1976. Some factors influencing Radiation of Sound from Flow Interaction with Edges of Finite Surfaces. NASA CR-145073.

15. Howe, M. S. 1975. Contributions to the Theory of Aerodynamic Sound, with Application to Excess Jet Noise and the Theory of the Flute. *J. Fluid Mech.* 71, 625-673.
16. Howe, M. S. 1977. A Review of the Theory of Trailing Edge Noise. NASA Contractor Report No. NAS1-14611-10.
17. Lighthill, M. J. 1952. On Sound Generated Aerodynamically; Pt. I, General Theory. *Proceedings of the Royal Society, Series A*, Vol. 211, pp. 564-587.
18. Manley, M. 1979. Experimental Study of Airfoil Trailing-Edge Noise: Instrumentation, Methodology and Initial Results. M. S. Thesis, Center for Acoustical Studies, Department of Mechanical and Aerospace Engineering, North Carolina State University, Raleigh, North Carolina.
19. McDonald, H. 1915. A Class of Diffraction Problems, *Proc. Lond. Math. Soc.* (2), 14, pp. 410-427.
20. Orszag, S. and S. Crow. 1970. Instability of a Vortex Sheet Leaving a Semi-infinite Plate. *Studies in Applied Mathematics* 49(2).
21. Schlichting, H. 1968. *Boundary-Layer Theory*. McGraw-Hill, New York, New York.
22. Shaw, L. 1978. Airframe Aerodynamic Noise - Total Radiated Acoustic Power Approach. *ASA Proceedings* (95).
23. Siddon, T. 1972. Surface Dipole Strength by Cross-correlation method. *JASA*, pp. 619-633.
24. Von Doenhoff, A. E. 1940. Investigation of the Boundary Layer about a Symmetrical Airfoil in a Wind-Tunnel of Low Turbulence. NACA Wartime Report.

11. APPENDICES

11.1 Results of Boundary Layer Rake Measurements

Tabulation and plots of the boundary layer parameters local convection velocity U_1 at the edge of the boundary layer, skin friction coefficient c_f , friction velocity U^* , wall stress τ_w , displacement thickness δ^* , momentum thickness θ , and form factor H determined from the boundary layer rake measurements as described in section 4.1 are given as a function of upstream velocity U_∞ for 0° , 5° , and 10° angles-of-attack.

Table 11.1 Boundary layer parameters for the NACA 0012 airfoil at 0° angle-of-attack from boundary layer rake measurements.
Rake at 0.238 cm from trailing-edge and 2.54 cm from airfoil centerline.

U_∞ m/s	V_1 m/s	c_f	U^* m/s	τ_w N/m ²	δ^* cm	θ cm	H
22.86	21.06	0.00225	0.7064	0.5964	0.4274	0.2748	1.566
38.10	35.45	0.00215	1.1623	1.6146	0.4003	0.2641	1.516
45.72	42.79	0.00200	1.3533	2.1890	0.4063	0.2702	1.503
53.34	50.14	0.00200	1.5855	3.0051	0.4089	0.2730	1.498
60.96	57.45	0.00200	1.8169	3.9457	0.4005	0.2678	1.496

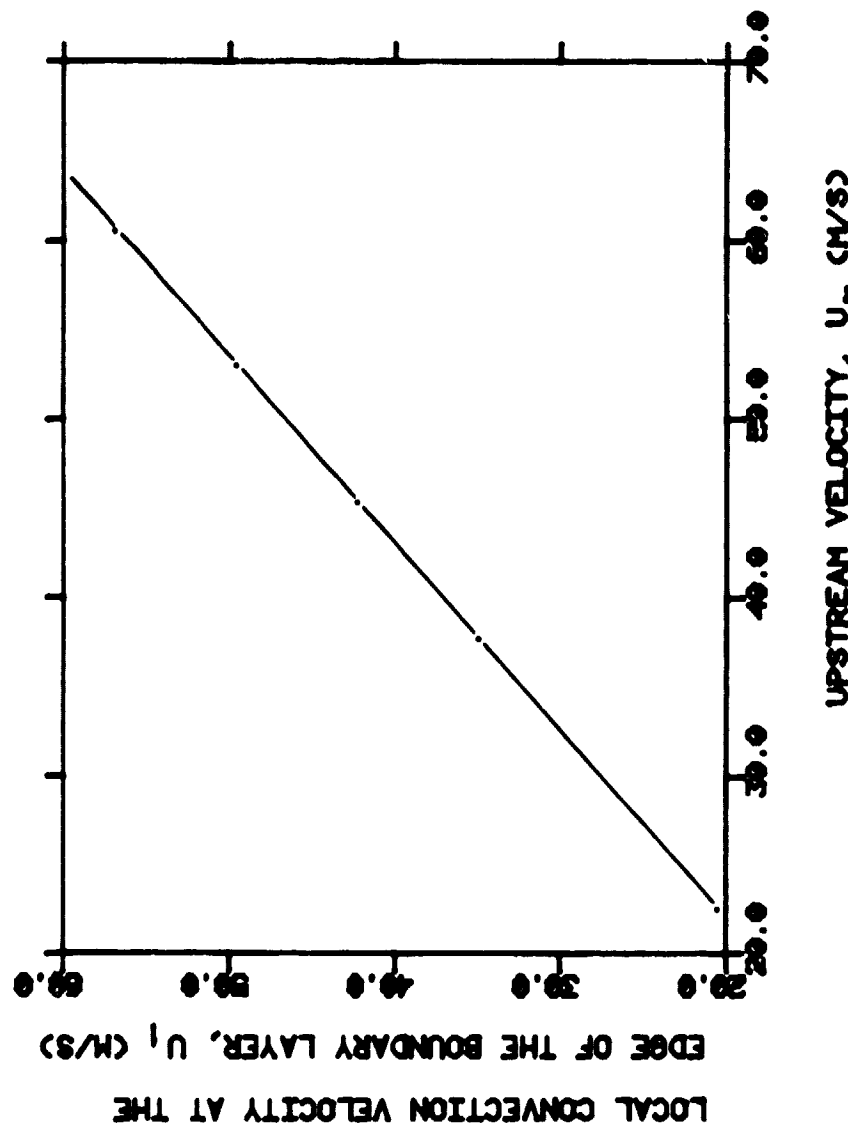


Figure 11.1 Local convection velocity at the edge of the boundary layer, U_1 , versus upstream velocity, U_∞ , from rake measurements at 0.238 cm from trailing-edge and 2.54 cm from airfoil centerline with airfoil at 0° angle-of-attack.

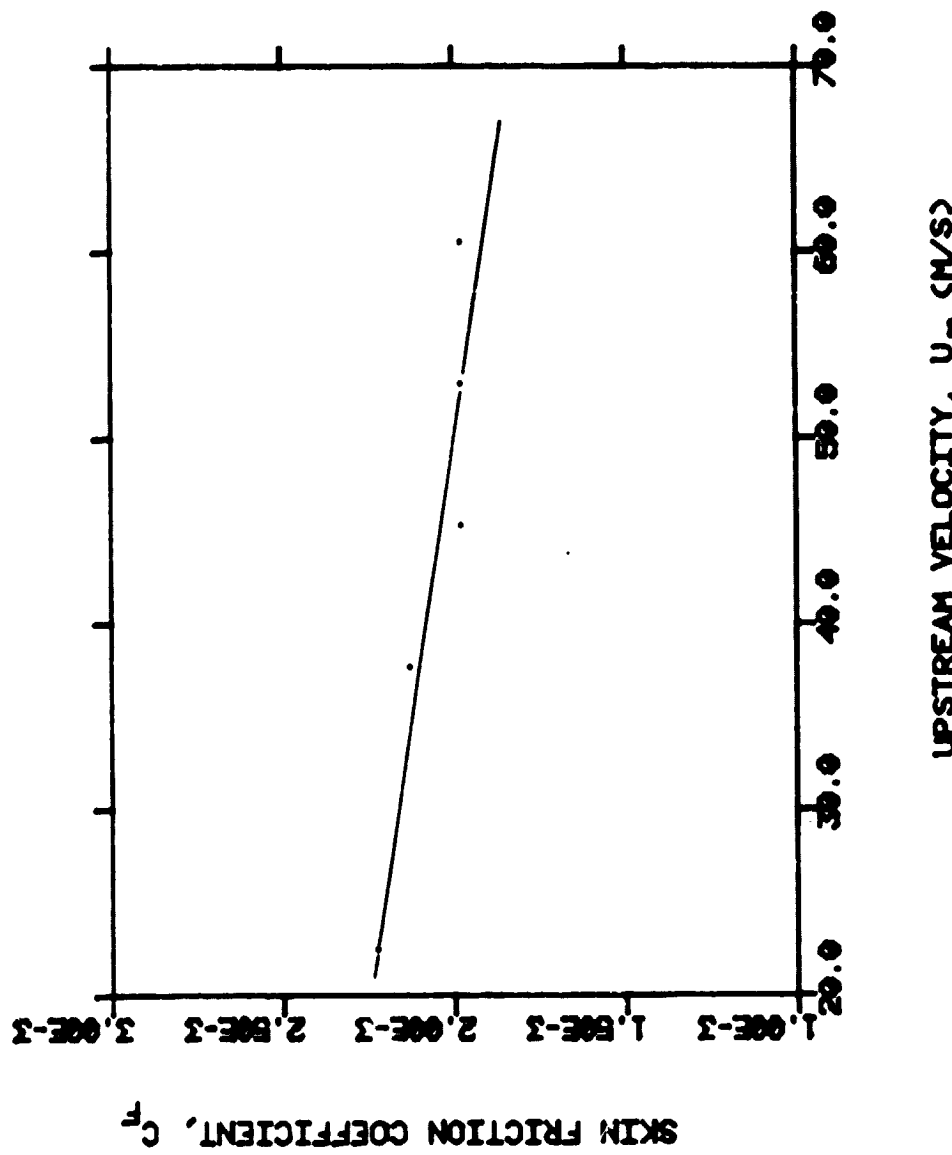


Figure 11.2 Skin friction coefficient, C_f , versus upstream velocity, U_∞ , from rake measurements at 0.238 cm from trailing-edge and 2.54 cm from airfoil centerline with airfoil at 0° angle-of-attack.

ORIGINAL PAGE IS
OF POOR QUALITY

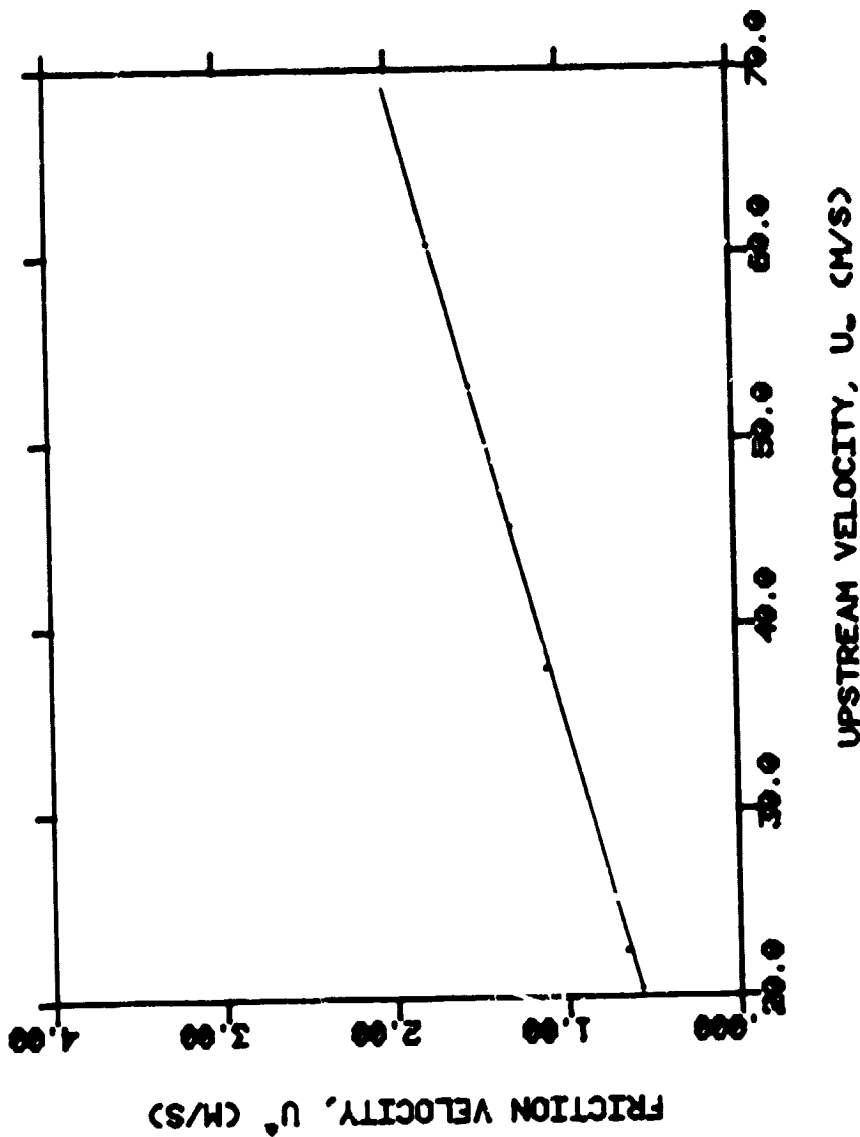


Figure 11.3 Friction velocity, U_s , versus upstream velocity, U_∞ , from rake measurements at 0.233 cm from trailing-edge and 2.54 cm from airfoil centerline with airfoil at 0° angle-of-attack.

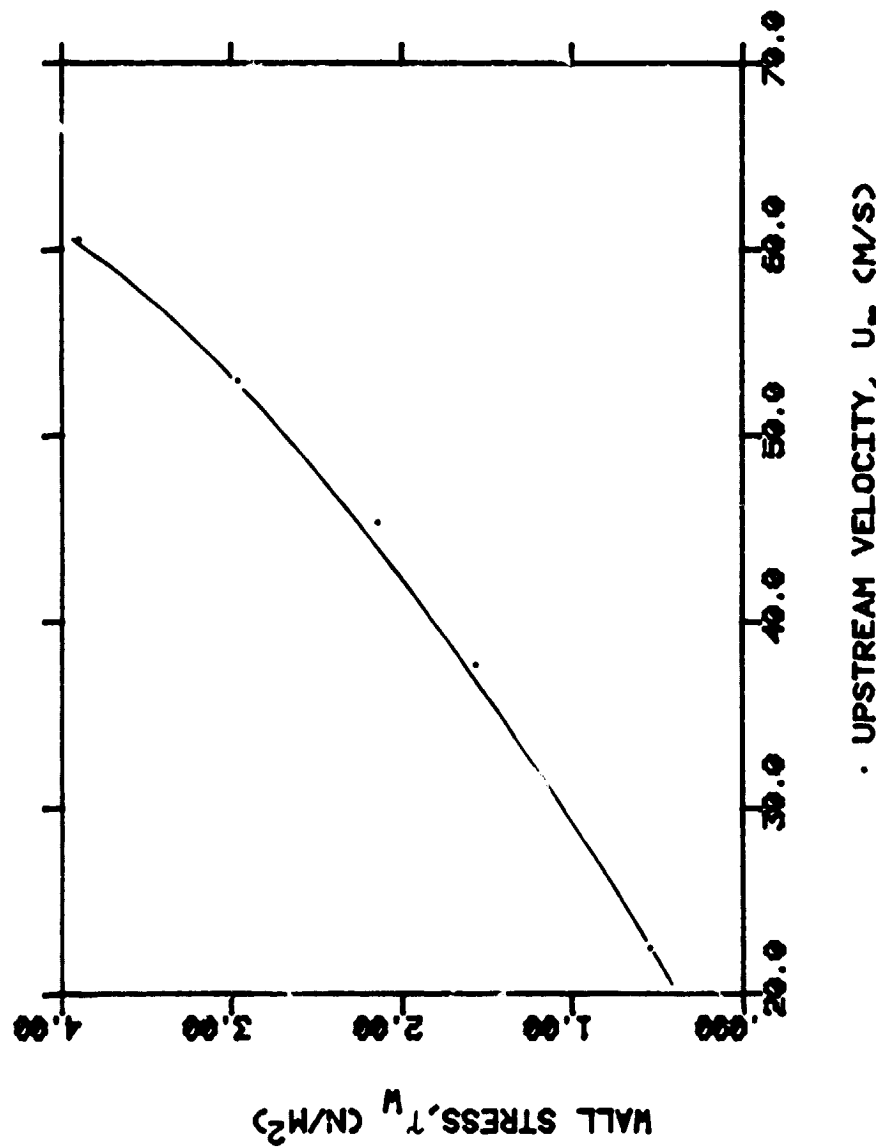


Figure 11.4 Wall stress, τ_w , versus upstream velocity, U_∞ , from rake measurements at 0.238 cm from trailing-edge and 2.54 cm from airfoil centerline with airfoil at 0° angle-of-attack.

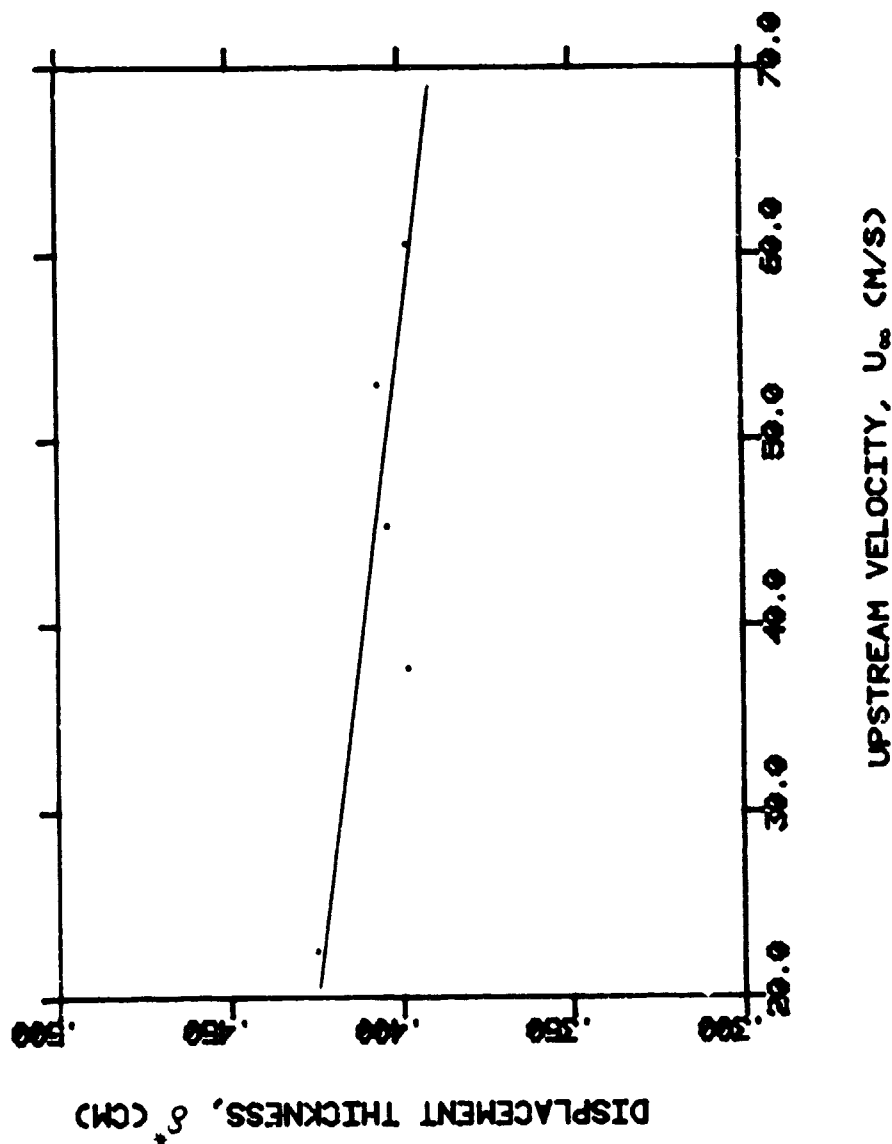


Figure 11.5 Displacement thickness, δ_* , versus upstream velocity, U_{∞} , from rake measurements at 0.238 cm from trailing-edge and 2.54 cm from airfoil centerline with airfoil at 0° angle-of-attack.

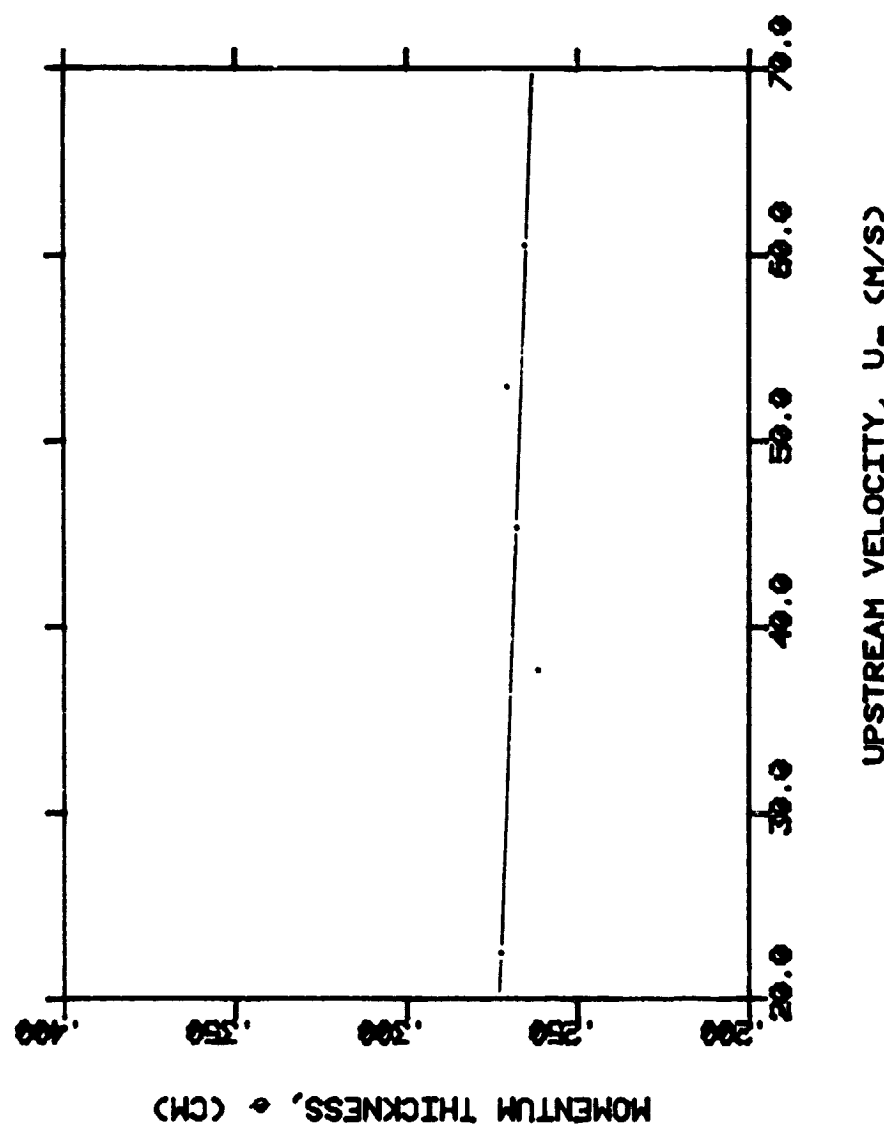


Figure 11.6 Momentum thickness, θ , versus upstream velocity, U_{∞} , from rake measurements at 0.238 cm from trailing-edge and 2.54 cm from airfoil centerline with airfoil at 0° angle-of-attack.

Figure 11.6

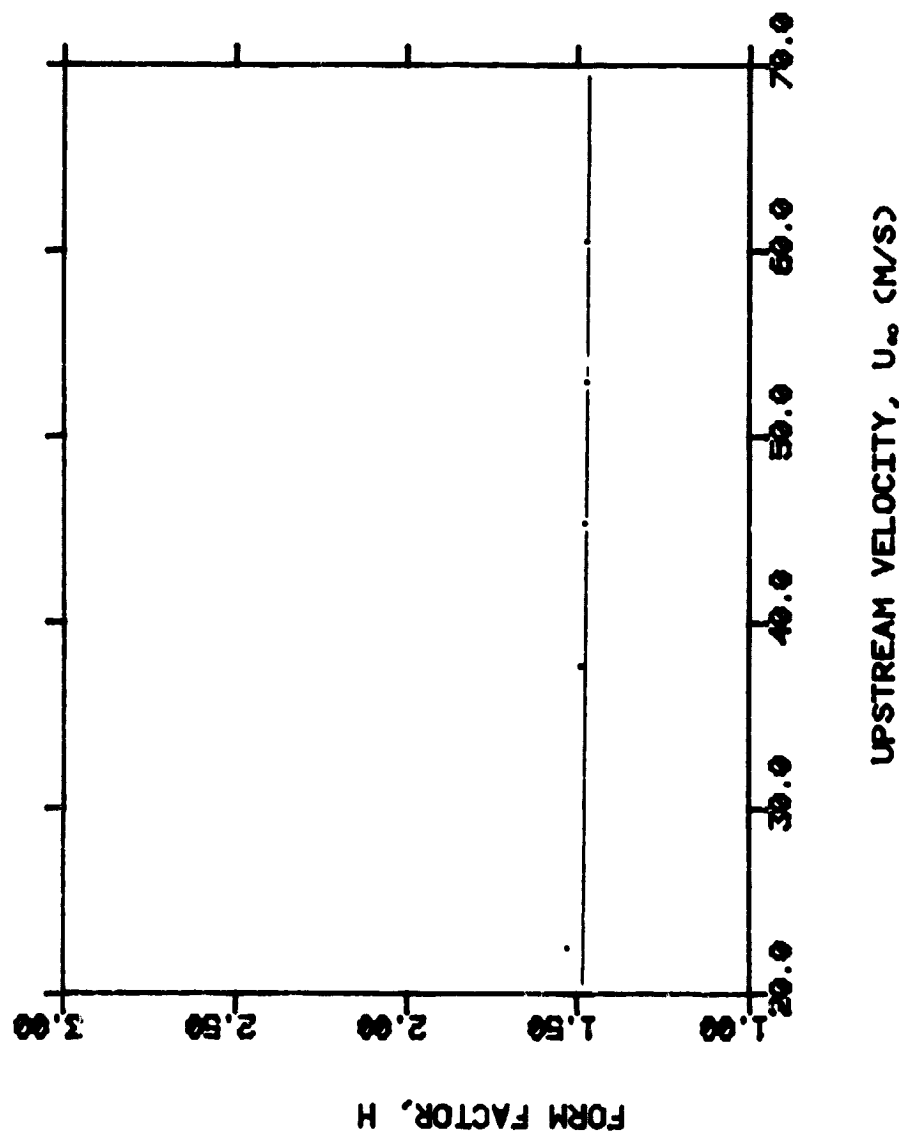


Figure 11.7 Form factor, H , versus upstream velocity, U_{∞} , from rake measurements at 0.238 cm from trailing-edge and 2.54 cm from airfoil centerline with airfoil at 0° angle-of-attack.

Figure 11.7

Table 11.2 Boundary layer parameters for the NACA 0012 airfoil at 5° angle-of-attack from boundary layer rake measurements.
Rake at 0.238 cm from trailing-edge and 2.54 cm from airfoil centerline.

U_∞ m/s	V_1 m/s	c_f	U^* m/s	τ_w N/m ²	δ^* cm	θ cm	H
38.10	35.69	0.00205	1.1427	1.5677	0.4362	0.2879	1.515
45.72	43.22	0.00220	1.3668	2.2426	0.4432	0.2941	1.507
53.34	50.26	0.00195	1.5694	2.9768	0.4301	0.2862	1.503
60.96	57.42	0.00195	1.7931	3.8596	0.4314	0.2886	1.495

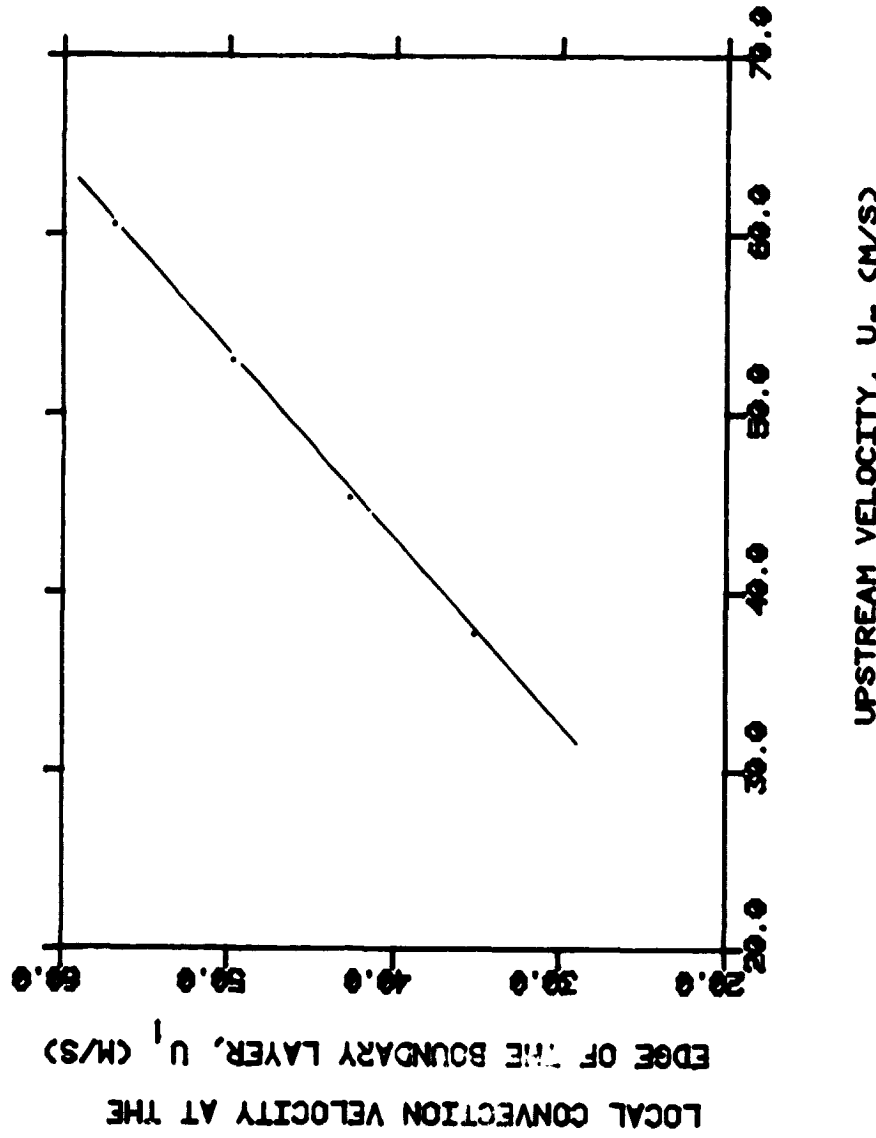


Figure 11.8 Local convection velocity at the edge of the boundary layer, U_1 , versus upstream velocity, U_∞ , from rake measurements at 0.238 cm from trailing-edge and 2.54 cm from airfoil centerline with airfoil at 5° angle-of-attack.

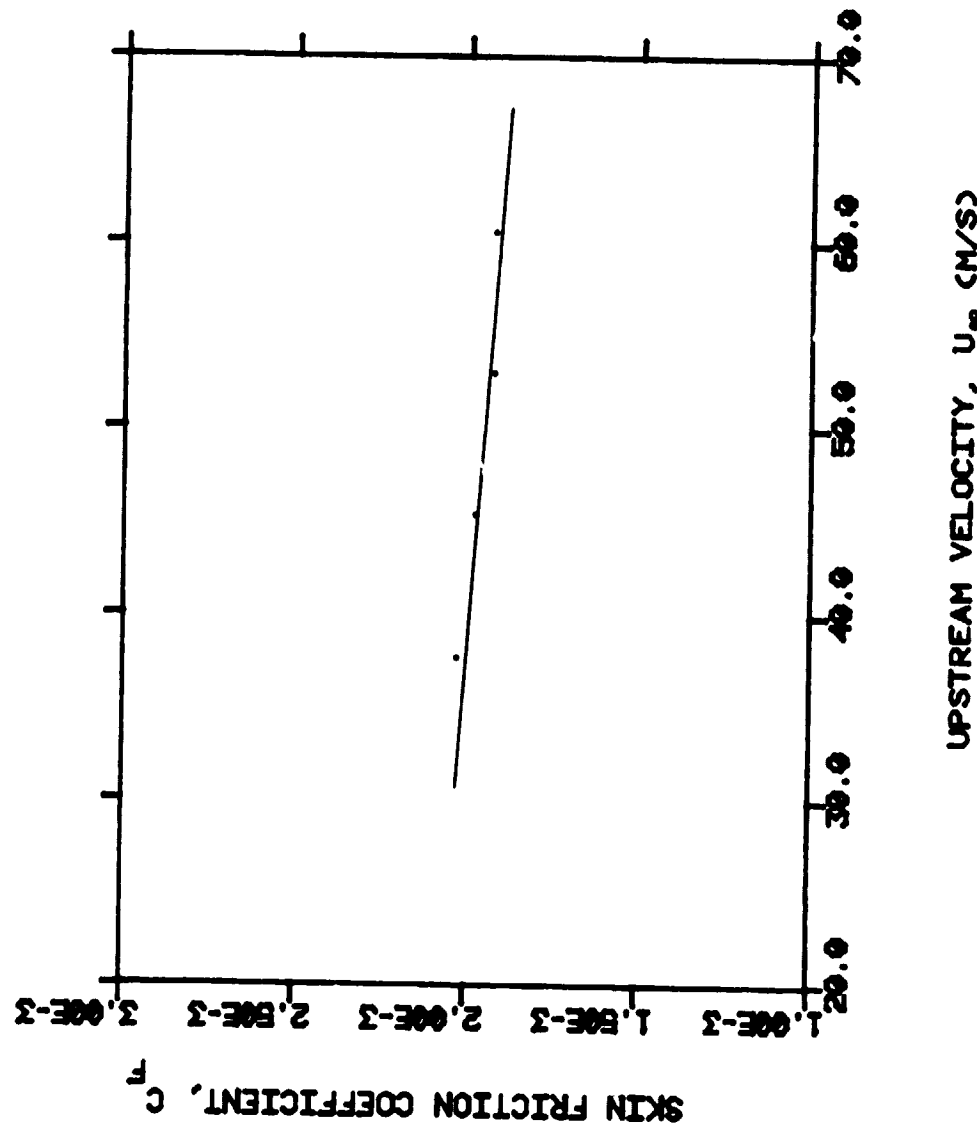


Figure 11.9 Skin friction coefficient, c_f , versus upstream velocity, U_∞ , from rake measurements at 0.238 cm from trailing-edge and 2.54 cm from airfoil centerline with airfoil at 5° angle-of-attack.

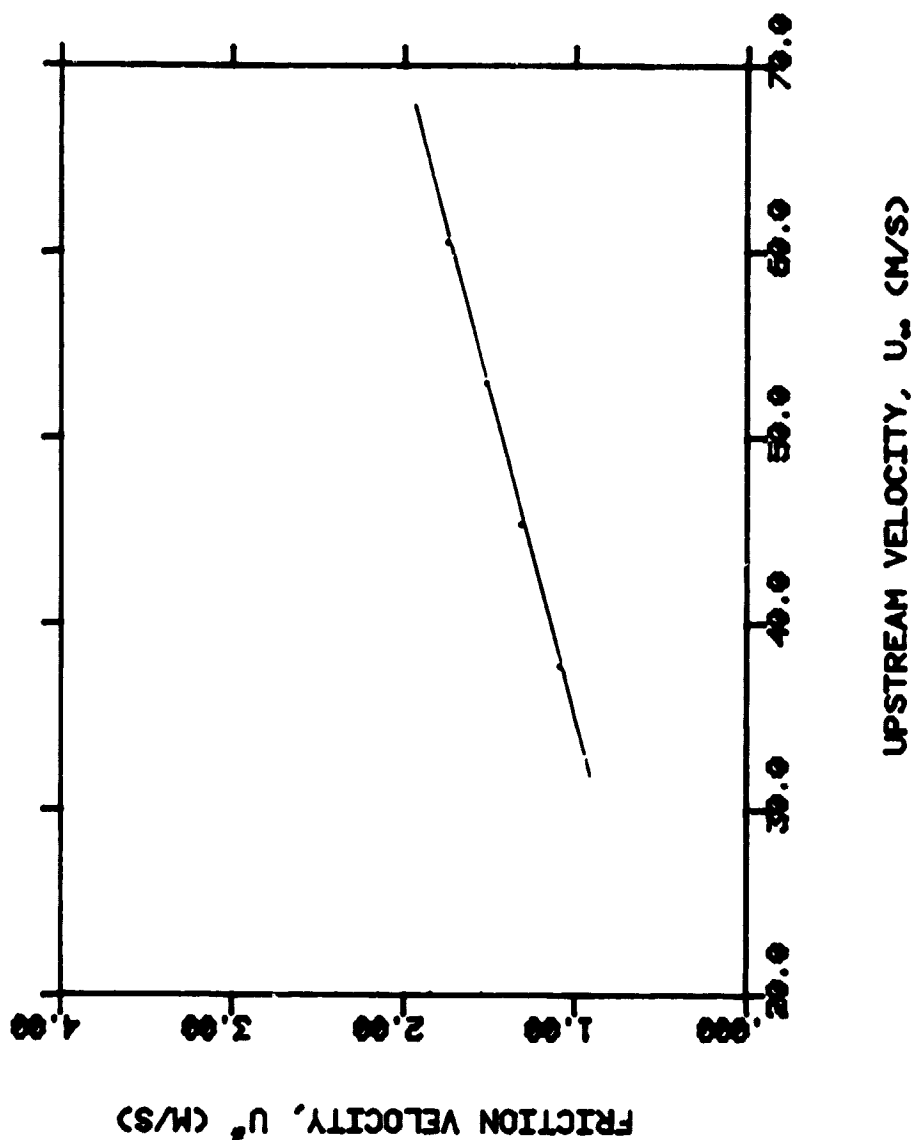


Figure 11.10 Friction velocity, U^* , versus upstream velocity, U^* , from rake measurements at 0.238 cm from trailing-edge and 2.54 cm from airfoil centerline with airfoil at 5° angle-of-attack.

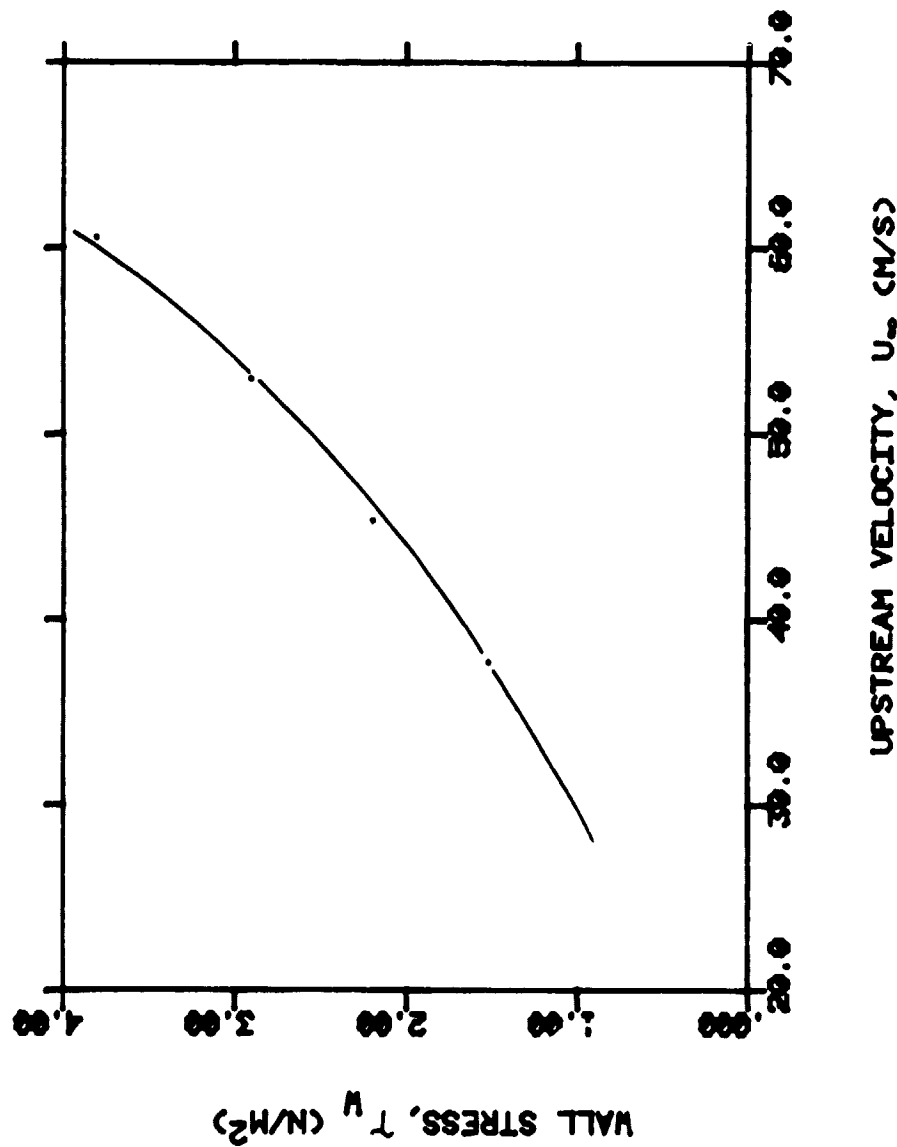


Figure 11.11 Wall stress, τ_w , versus upstream velocity, U_∞ , from rake measurements at 0.238 cm from trailing-edge and 2.54 cm from airfoil centerline with airfoil at 5° angle-of-attack.

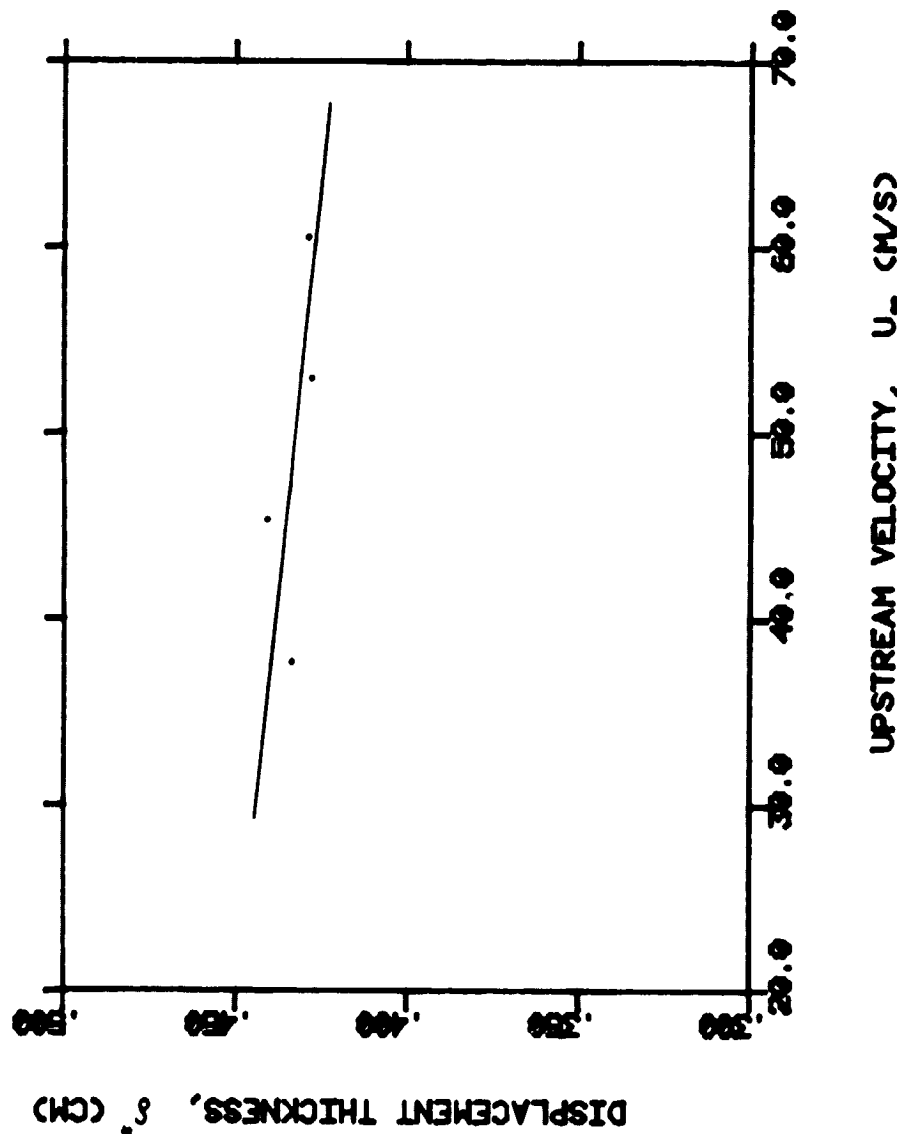


Figure 11.12 Displacement thickness, δ^* , versus upstream velocity, U_∞ , from rake measurements at 0.238 cm from trailing-edge and 2.54 cm from airfoil centerline with airfoil at 5° angle-of-attack.

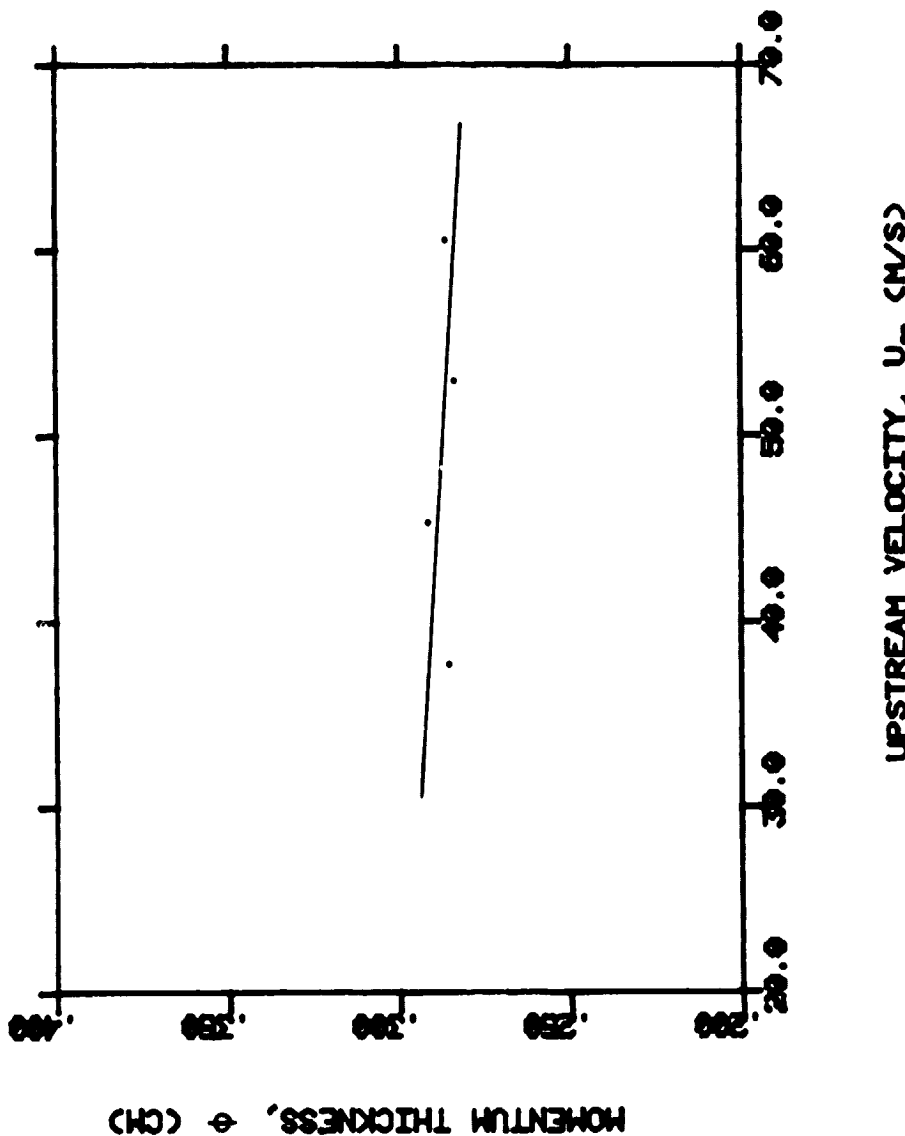


Figure 11.13 Momentum thickness, θ , versus upstream velocity, U_{∞} , from rake measurements at 0.238 cm from trailing-edge and 2.54 cm from airfoil centerline with airfoil at 5° angle-of-attack.

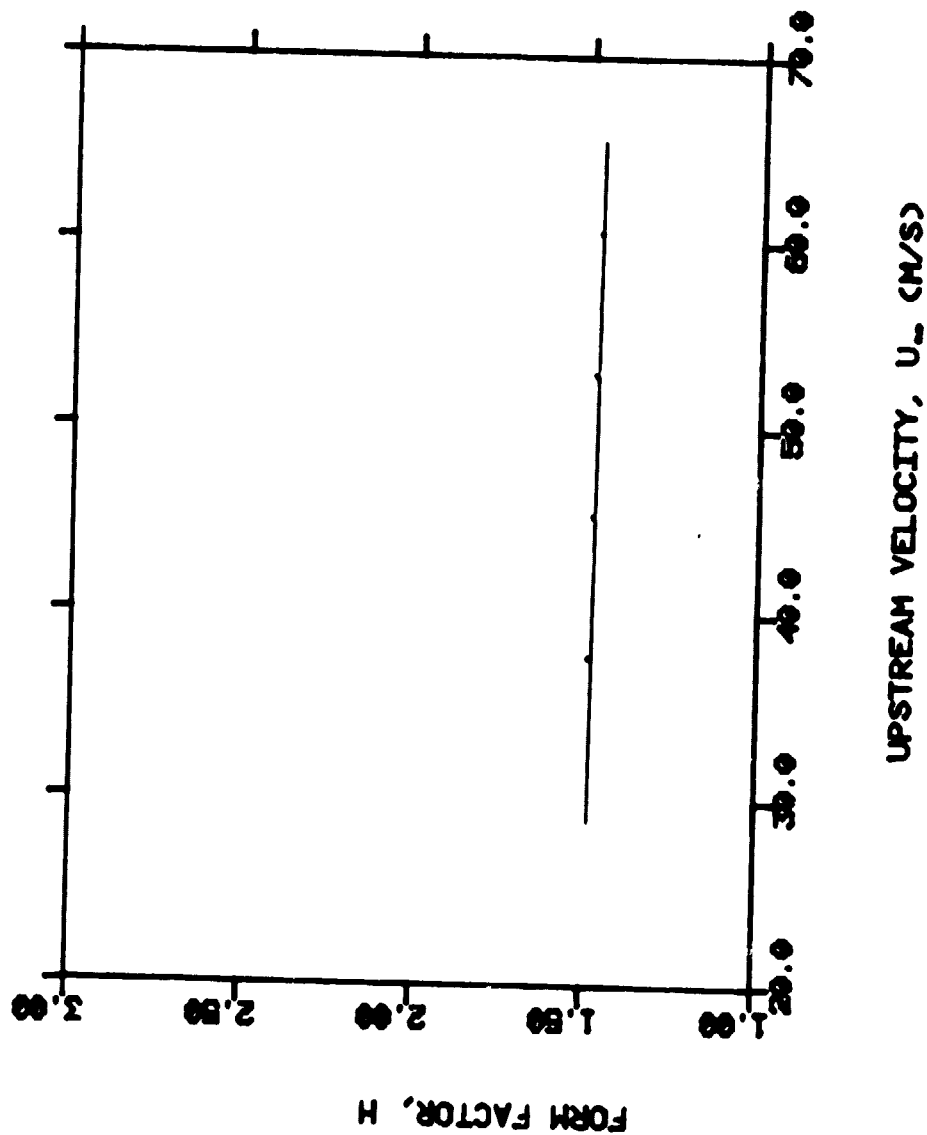


Figure 11.14 Form factor, H , versus upstream velocity, U_{∞} , from rake measurements at 0.238 cm from trailing-edge and 2.54 cm from airfoil centerline with airfoil at 5° angle-of-attack.

Table 11.3 Boundary layer parameters for the NACA 0012 airfoil at 10° angle-of-attack from boundary layer rake measurements.
Rake at 0.238 cm from trailing-edge and 2.54 cm from airfoil centerline.

U_∞ m/s	V_1 m/s	c_f	U^* m/s	τ_w N/m ²	δ^* cm	θ cm	H
38.10	35.69	0.00210	1.1566	1.6060	0.4848	0.3240	1.497
45.72	43.13	0.00200	1.3639	2.2330	0.4686	0.3157	1.484
53.34	50.54	0.00195	1.5780	2.9893	0.4662	0.3134	1.487
60.96	57.85	0.00190	1.7831	3.8170	0.4643	0.3137	1.480

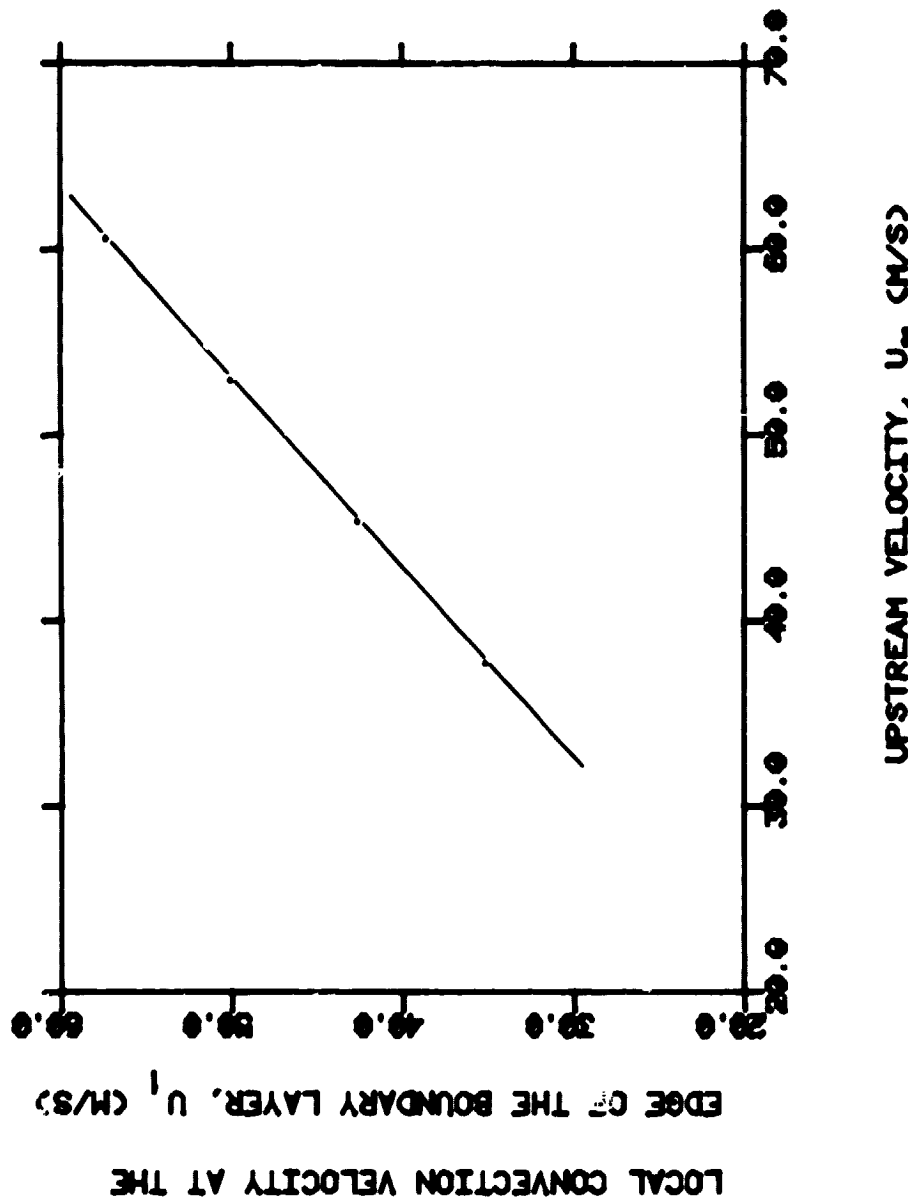


Figure 11.15 Local convection velocity at the edge of the boundary layer, U_1 , versus upstream velocity, U_{∞} , from rake measurements at 0.238 cm from trailing-edge and 2.54 cm from airfoil centerline with airfoil at 10° angle-of-attack.

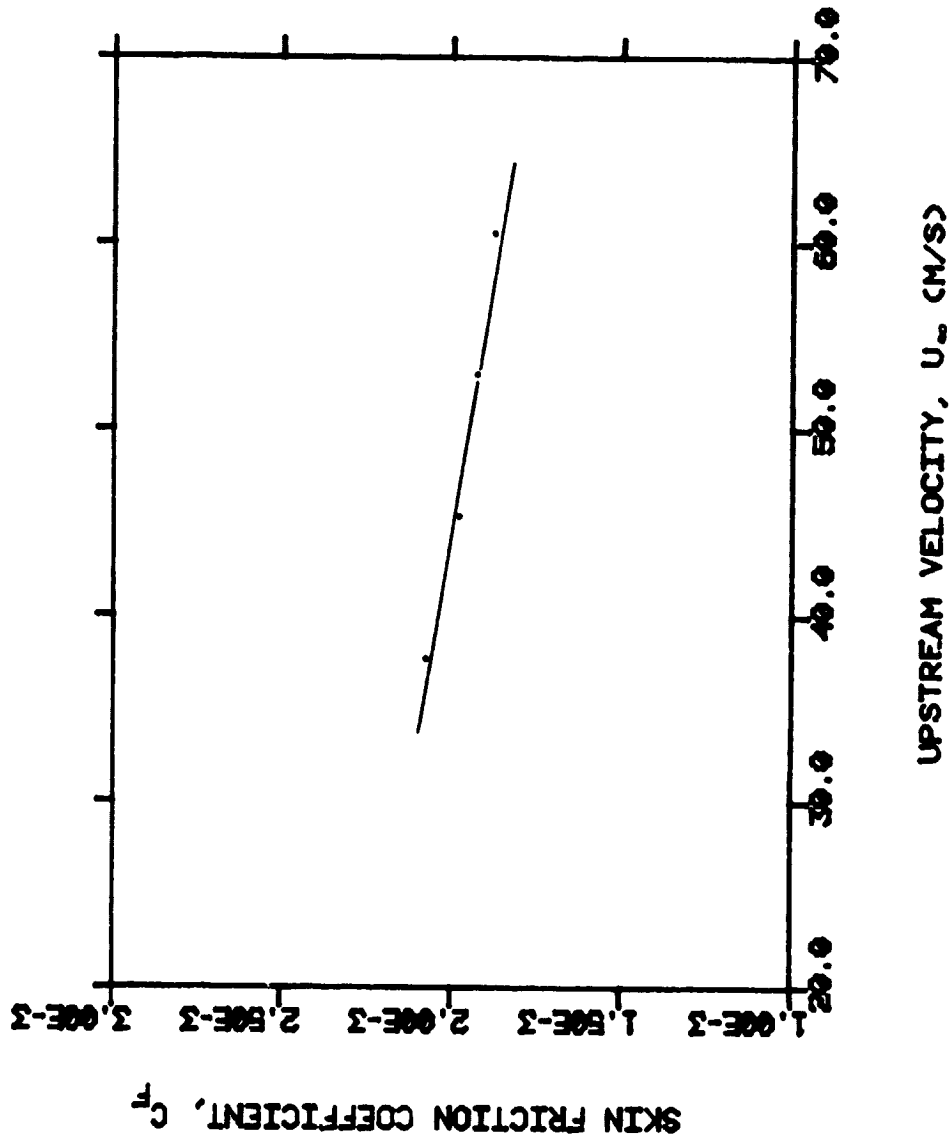


Figure 11.16 Skin friction coefficient, C_f , versus upstream velocity, U_∞ , from rake measurements at 0.238 cm from trailing-edge and 2.54 cm from airfoil centerline with airfoil at 10° angle-of-attack.

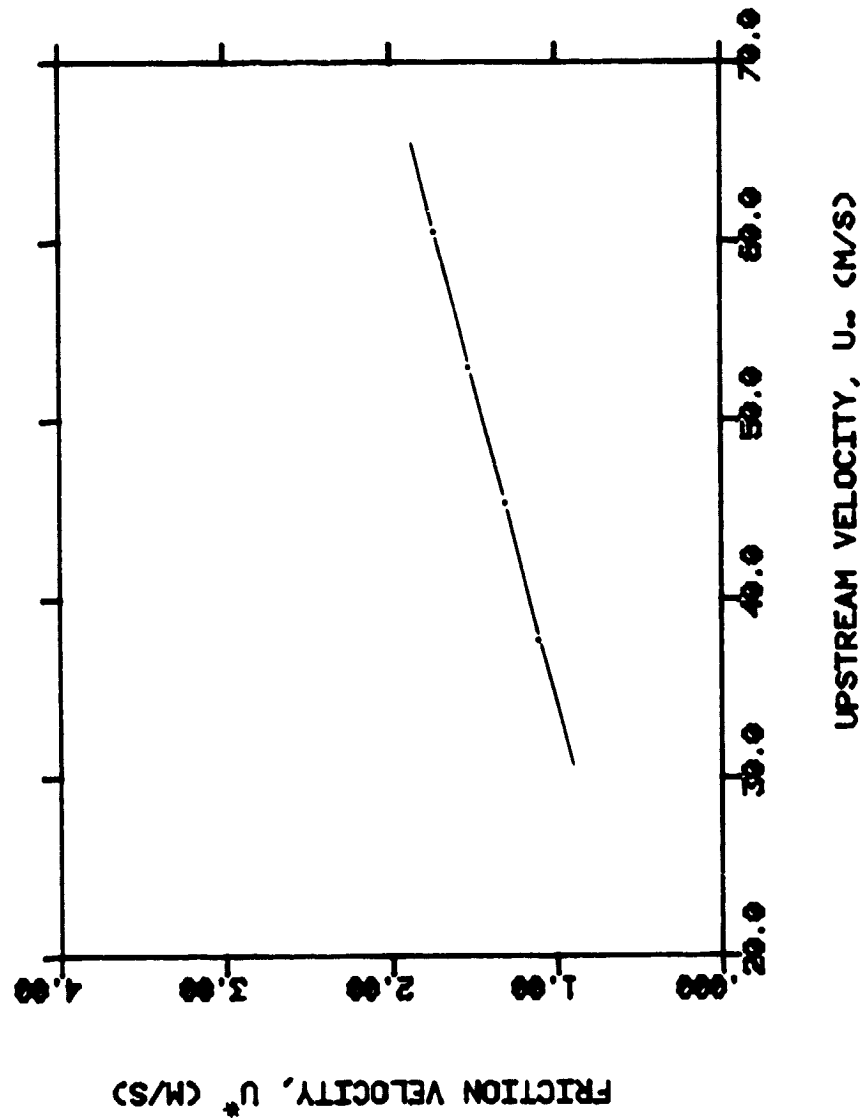


Figure 11.17 Friction velocity, U^* , versus upstream velocity, U_∞ , from rake measurements at 0.238 cm from trailing-edge and 2.54 cm from airfoil centerline with airfoil at 10° angle-of-attack.

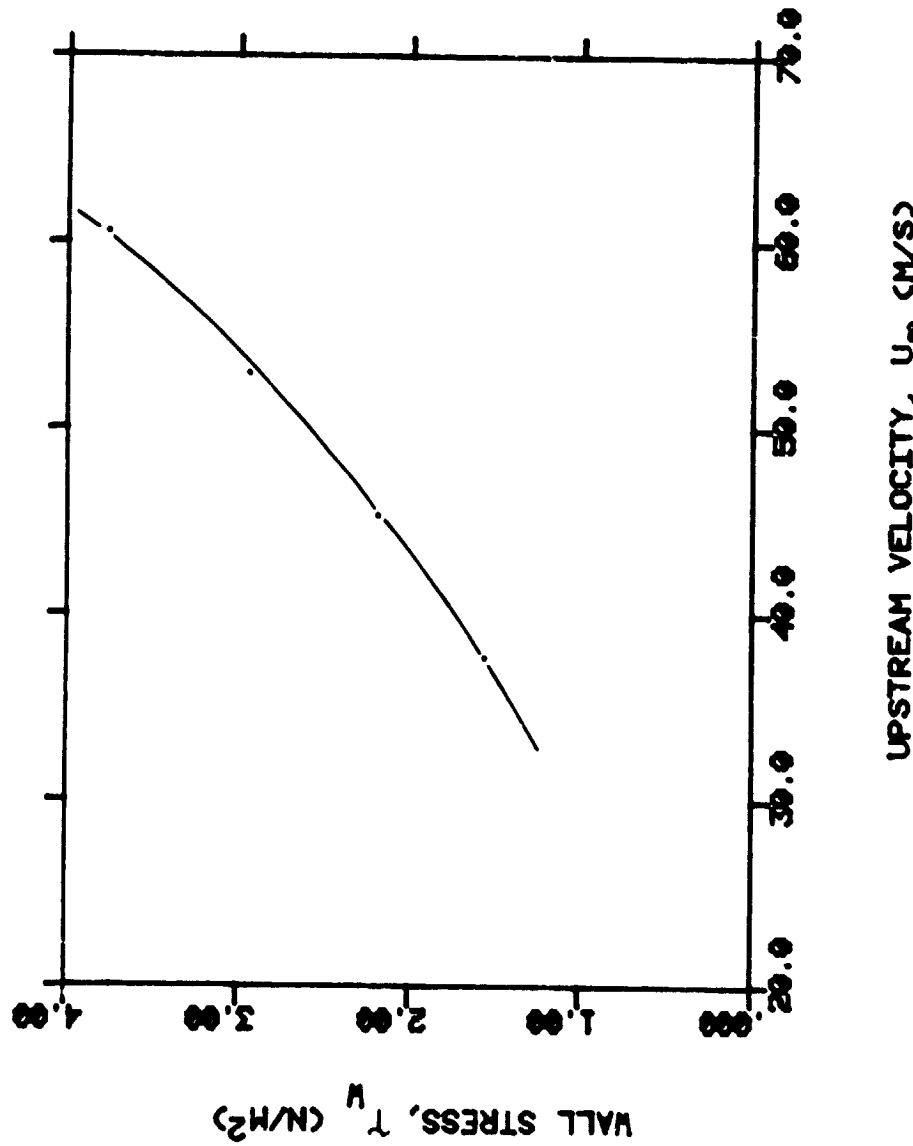


Figure 11.18 Wall stress, τ_w , versus upstream velocity, U_∞ , from rake measurements at 0.238 cm from trailing-edge and 2.54 cm from airfoil centerline with airfoil at 10° angle-of-attack.

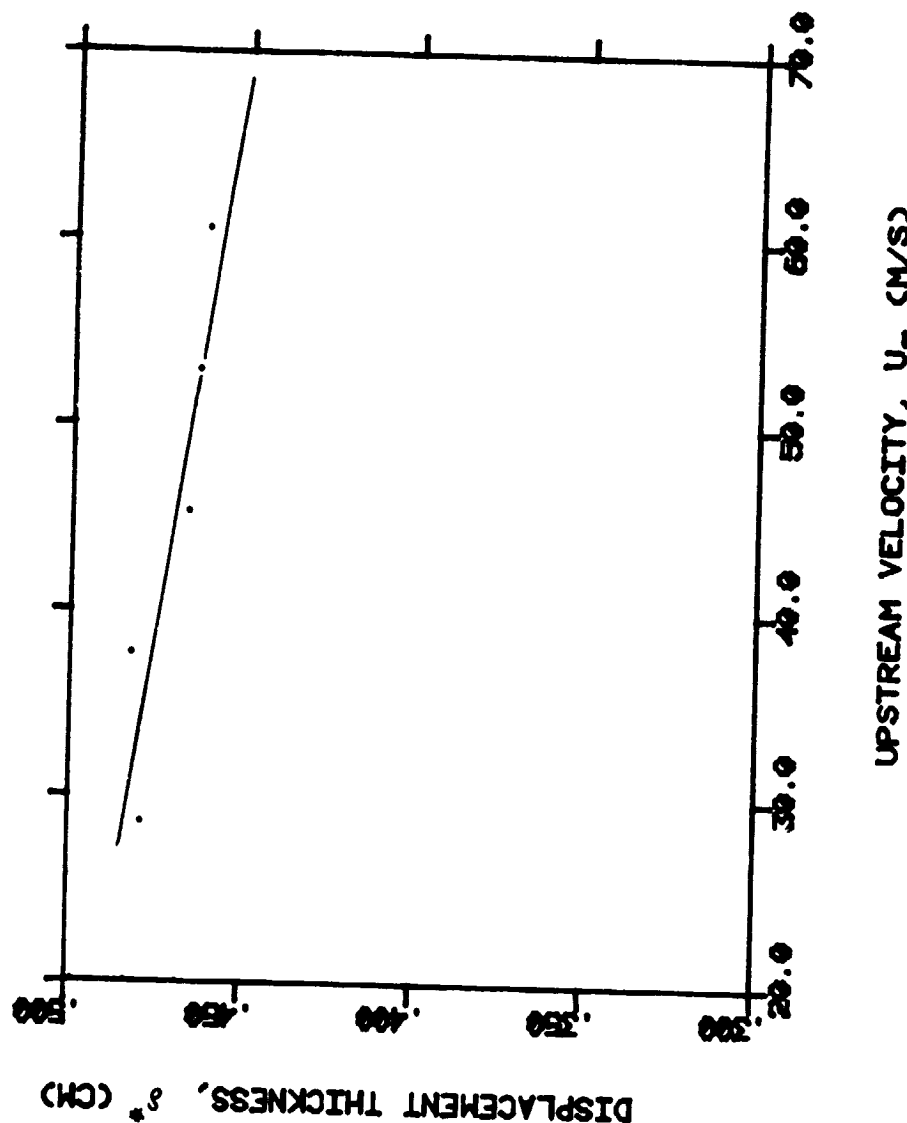


Figure 11.19 Displacement thickness, δ_+ , versus upstream velocity, U_{∞} , from rake measurements at 0.238 cm from trailing-edge and 2.54 cm from airfoil centerline with airfoil at 10° angle-of-attack.

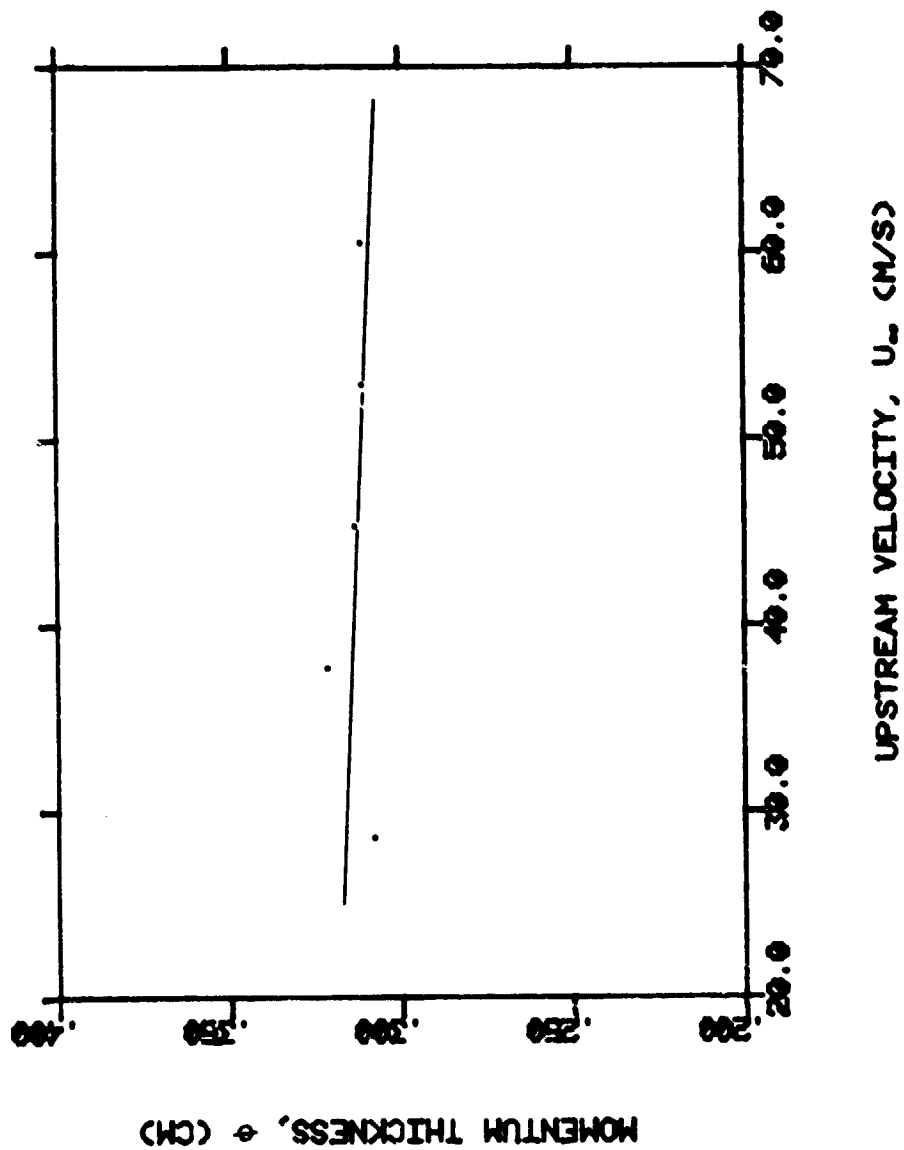


Figure 11.20 Momentum thickness, θ , versus upstream velocity, U_∞ , from rake measurements at 0.238 cm from trailing-edge and 2.54 cm from airfoil centerline with airfoil at 10° angle-of-attack.

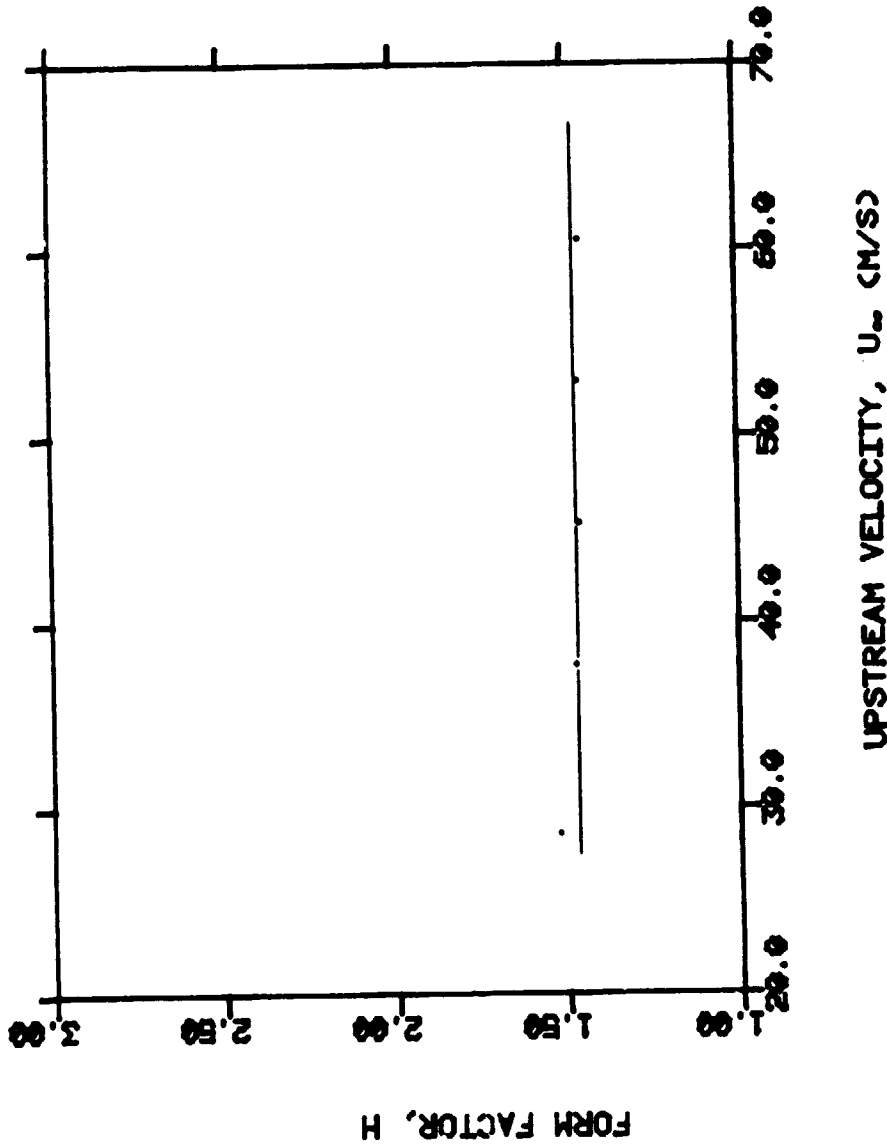


Figure 11.21 Form factor, H , versus upstream velocity, U_{∞} , from rake measurements at 0.238 cm from trailing-edge and 2.54 cm from airfoil centerline with airfoil at 10° angle-of-attack.

11.2 Results of Boundary Layer Preston Tube Measurements

Tabulation and plots of the boundary layer parameters wall stress τ_w , friction velocity U^* , and skin friction coefficient c_f determined from the boundary layer Preston tube measurements as described in section 4.2 are given as a function of upstream velocity U_∞ for the Preston tube chordwise positions of 0.238 cm, 2.54 cm, and 22.86 cm from the trailing-edge.

Table 11.4 Boundary layer parameters for the NACA 0012 airfoil at 0° angle-of-attack obtained from Preston tube measurements at 0.238 cm from the trailing-edge on the airfoil centerline.

U_∞ m/s	τ_w N/m ²	U^* m/s	c_f
22.86	0.7371	0.7803	0.0027
38.10	1.8667	1.2418	0.0024
53.34	3.5277	1.7069	0.0023
68.58	5.5380	2.1388	0.0022

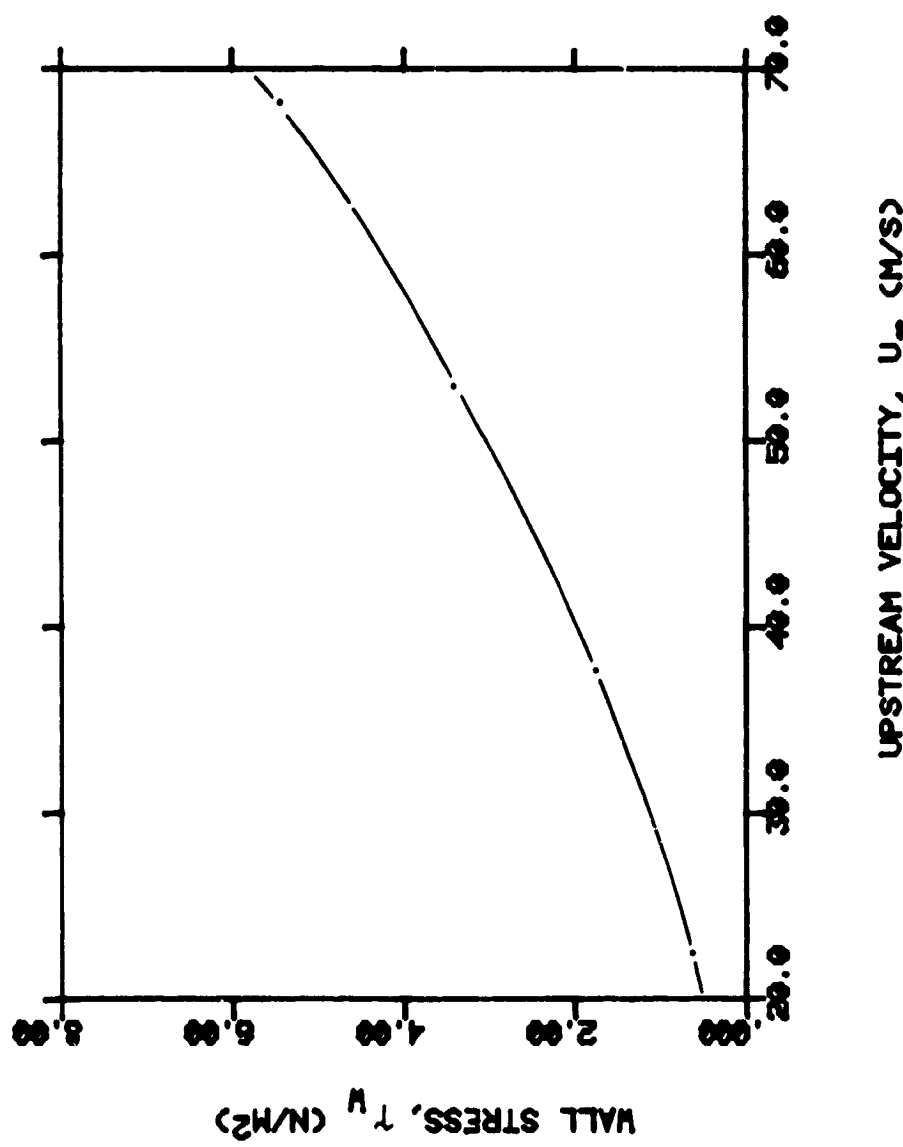


Figure 11.22 Wall stress, τ_w , versus upstream velocity, U_∞ , from Preston tube measurements at 0.238 cm from trailing-edge on airfoil centerline with airfoil at 0° angle-of-attack.

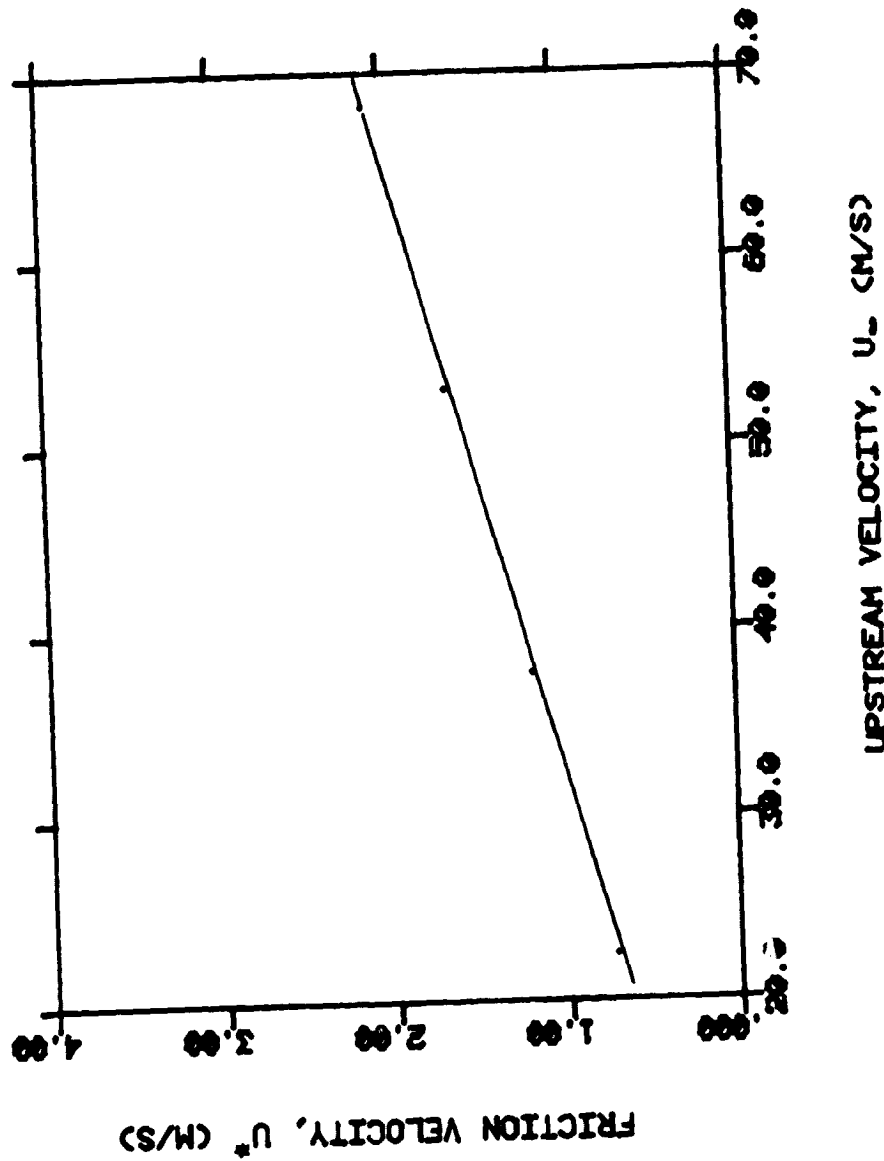


Figure 11.23 Friction velocity, U^* , versus upstream velocity, U_∞ , from Preston tube measurements at 0.238 cm from trailing edge on airfoil centerline with airfoil at 0° angle-of-attack.

ORIGINAL PAGE IS
OF POOR QUALITY.

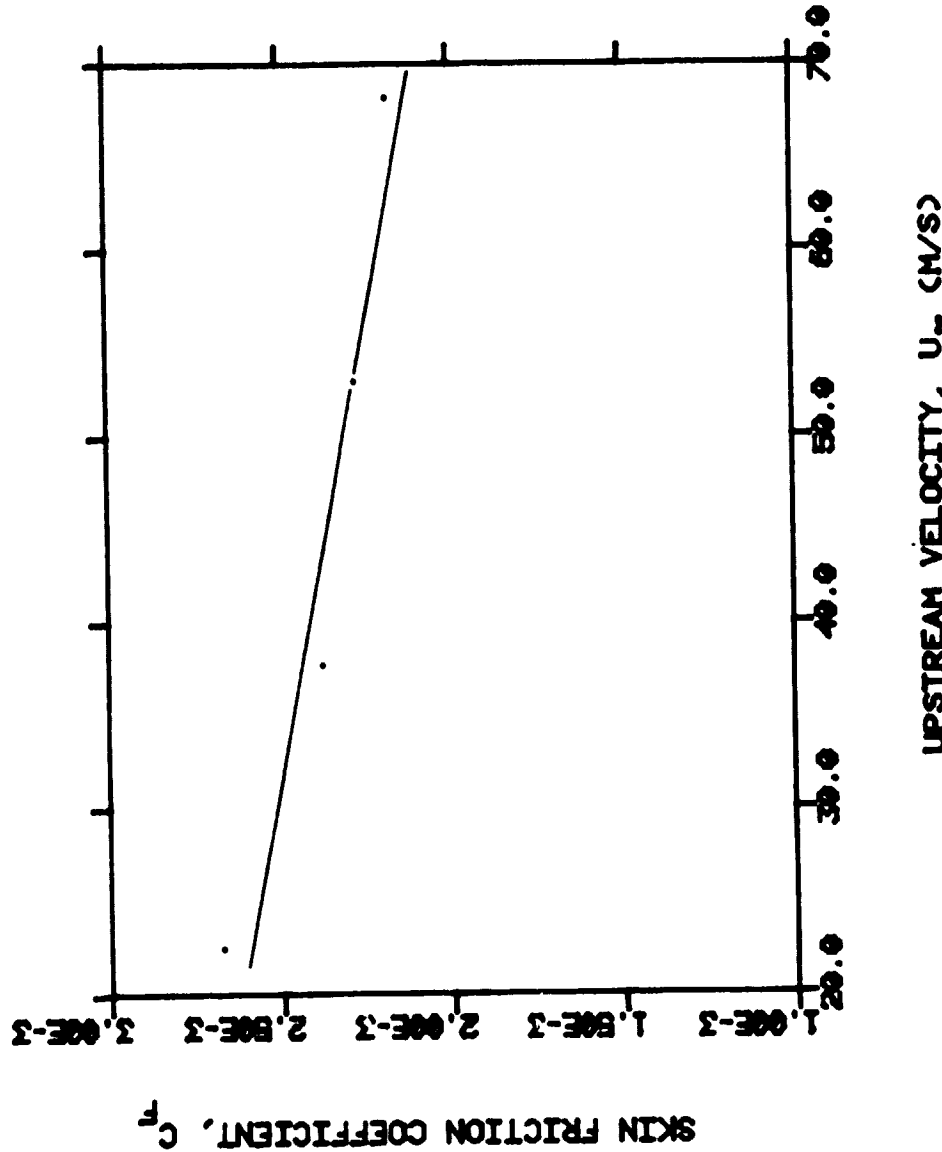


Figure 11.24 Skin friction coefficient, C_f , versus upstream velocity, U_∞ , from Preston tube measurements at 0.238 cm from trailing-edge on airfoil centerline with airfoil at 0° angle-of-attack.

Table 11.5 Boundary layer parameters for the NACA 0012 airfoil at 0° angle-of-attack obtained from Preston tube measurements at 2.54 cm from the trailing-edge on the airfoil centerline.

U_∞ m/s	τ_w N/m ²	U^* m/s	c_f
22.86	0.9238	0.8736	0.0031
38.10	2.3788	1.4018	0.0029
53.34	4.5231	1.9327	0.0027
68.58	7.2513	2.4472	0.0026

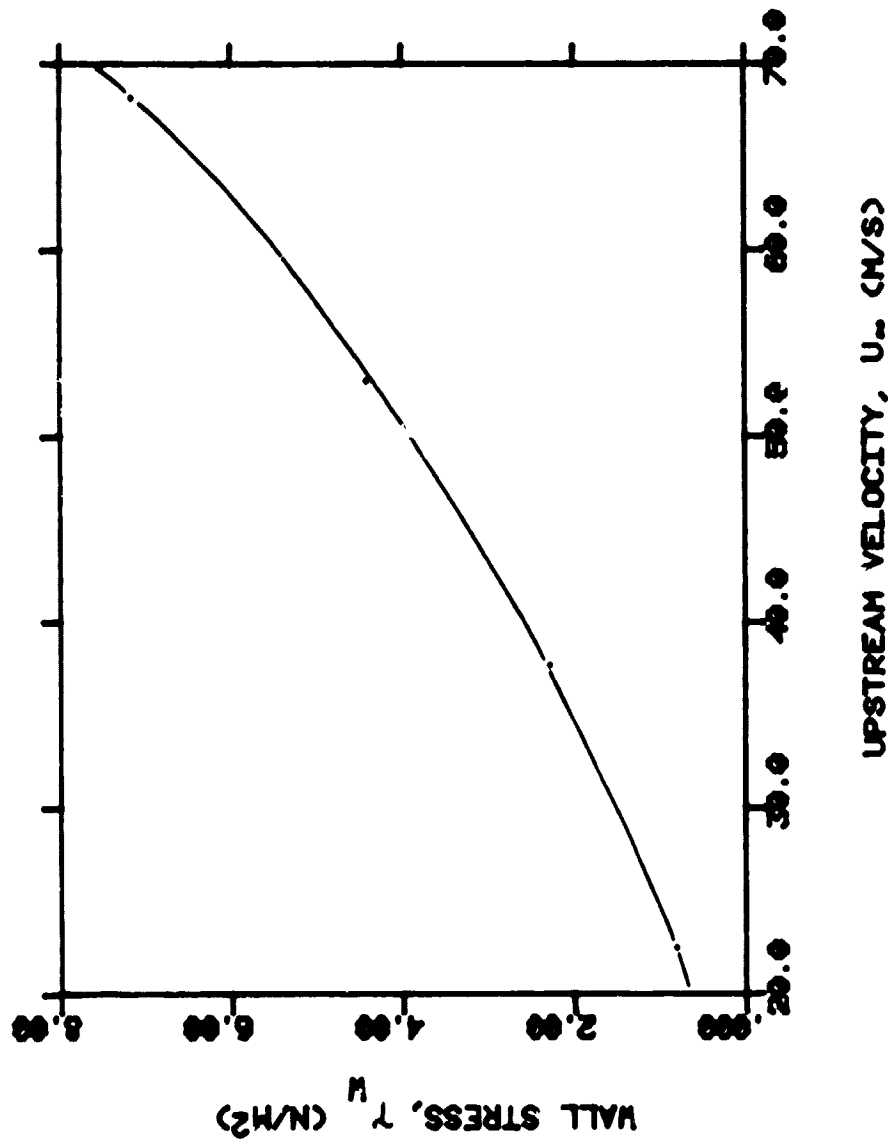


Figure 11.25 Wall stress, τ_w , versus upstream velocity, U_{∞} , from Preston tube measurements at 2.54 cm from trailing-edge on airfoil centerline with airfoil at 0° angle-of-attack.

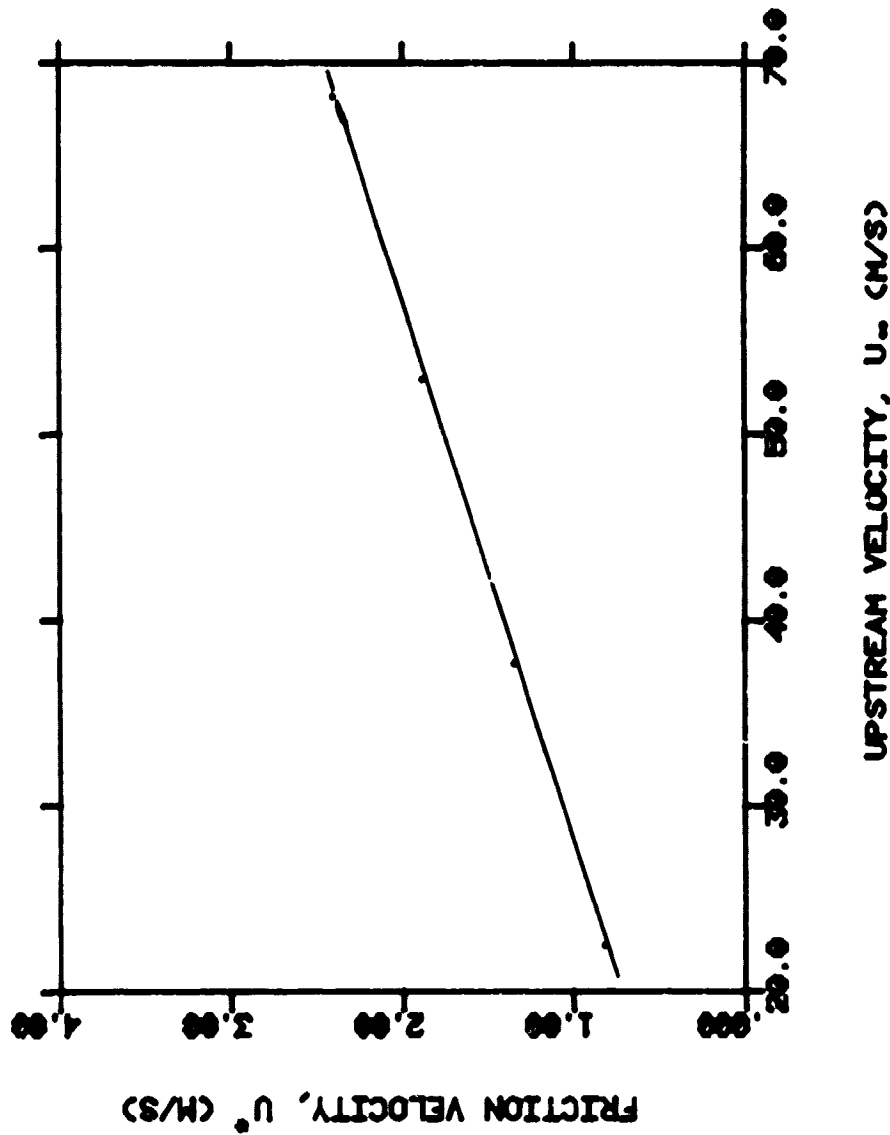


Figure 11.26 Friction velocity, u^* , versus upstream velocity, U_∞ , from Preston tube measurements at 2.54 cm from trailing edge on airfoil centerline with airfoil at 0° angle-of-attack.

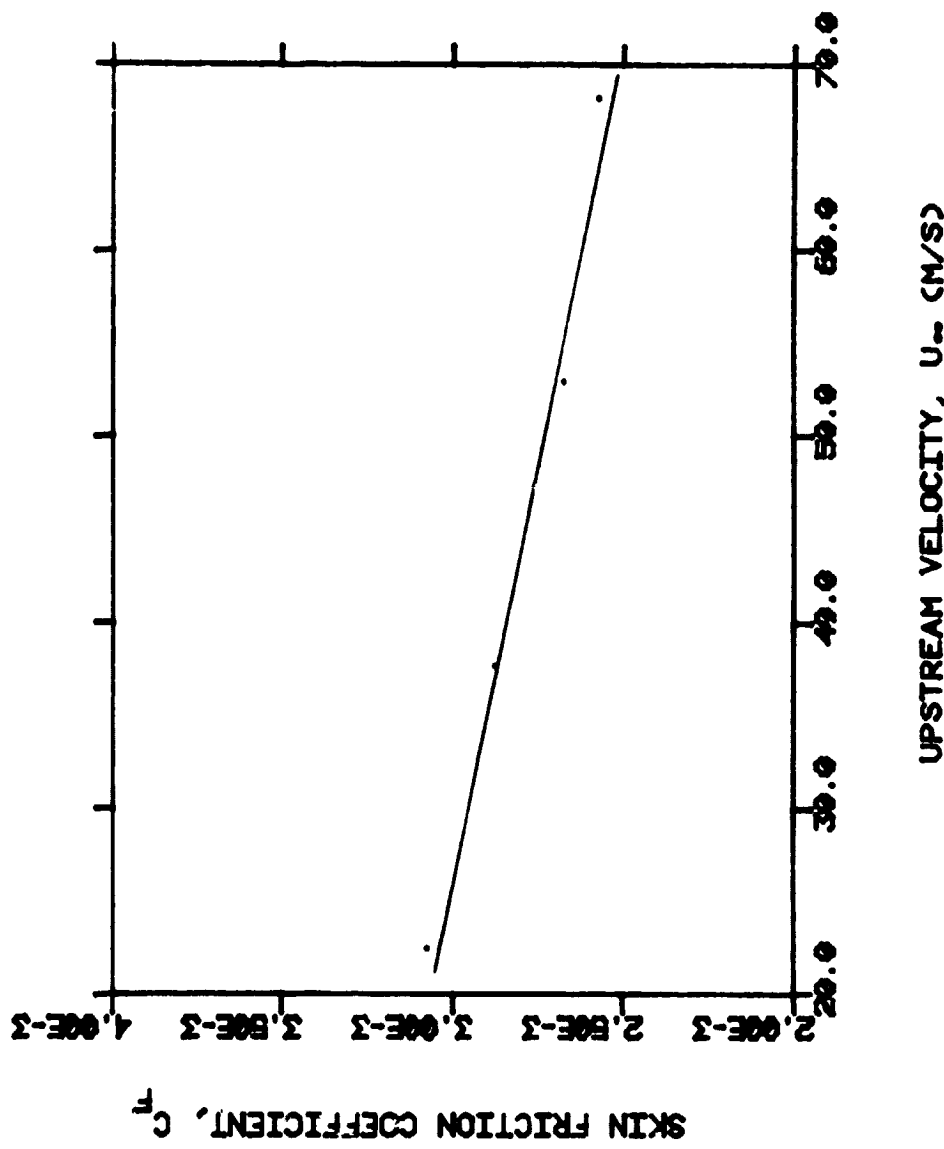


Figure 11.27 Skin friction coefficient, C_f , versus upstream velocity, U_∞ , from Preston tube measurements at 2.54 cm from trailing-edge on airfoil centerline with airfoil at 0° angle-of-attack.

Table 11.6 Boundary layer parameters for the NACA 0012 airfoil at 0° angle-of-attack obtained from Preston tube measurements at 22.86 cm from the trailing-edge on the airfoil centerline.

U_∞ m/s	τ_w N/m ²	U^* m/s	c_f
22.86	1.4694	1.1015	0.0039
38.10	3.6711	1.7413	0.0035
53.34	6.8493	2.3784	0.0033
68.58	10.726	2.9764	0.0031

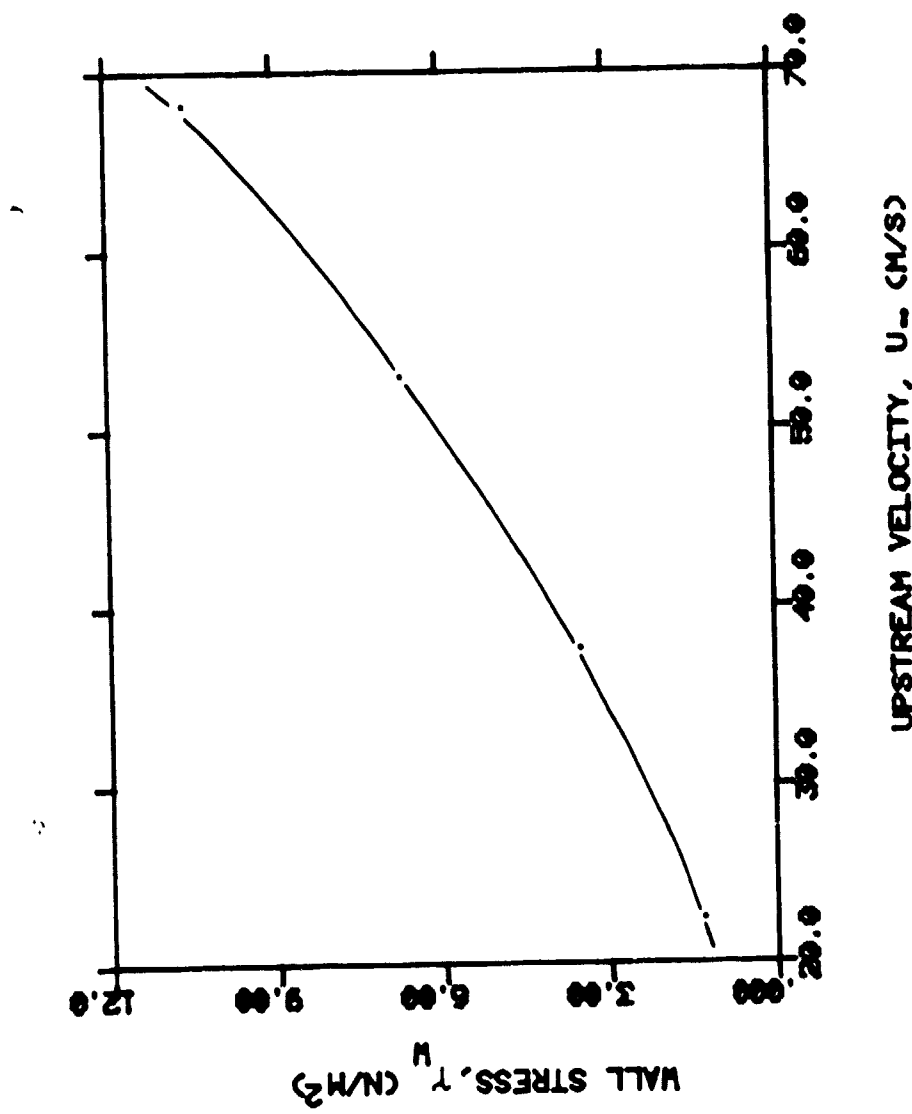


Figure 11.28 Wall stress, τ_w , versus upstream velocity, U_∞ , from Preston tube measurements at 22.86 cm from trailing-edge on airfoil centerline with airfoil at 0° angle-of-attack.

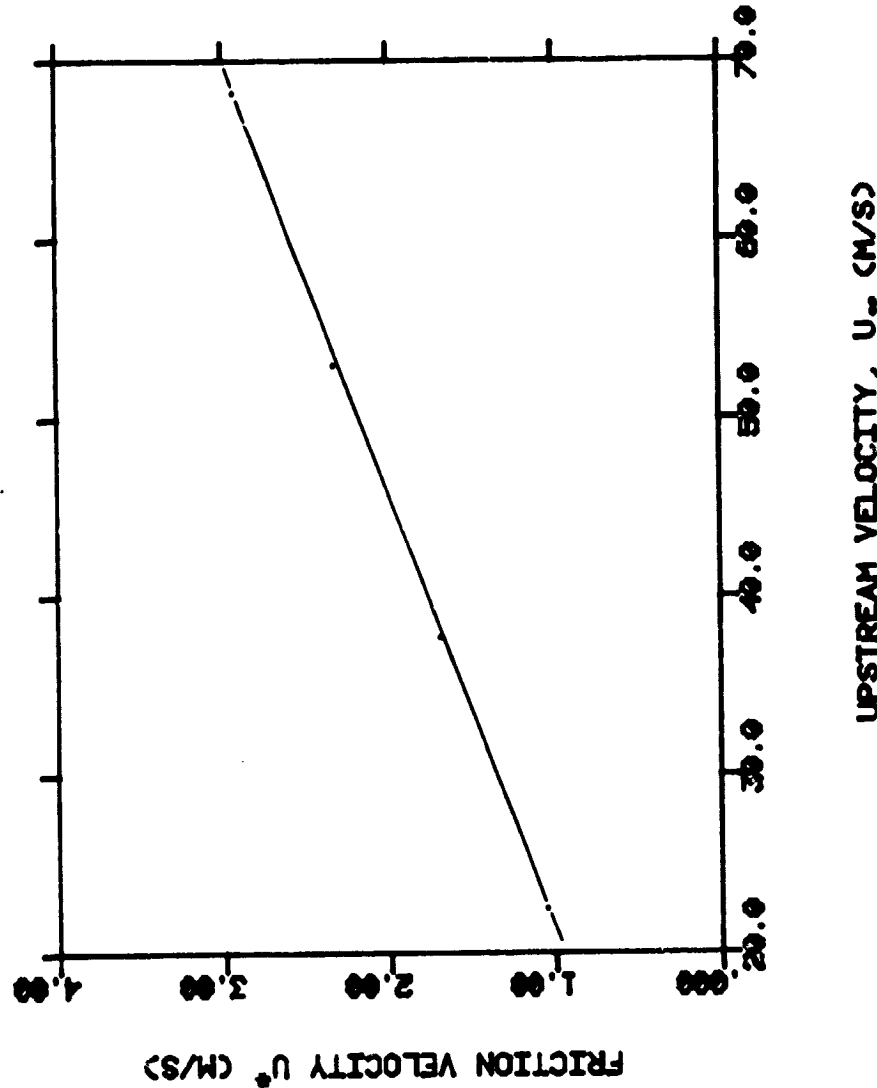


Figure 11.29 Friction velocity, U^* , versus upstream velocity, U_0 , from Preston tube measurements at 22.86 cm from trailing-edge on airfoil centerline with airfoil at 0° angle-of-attack.

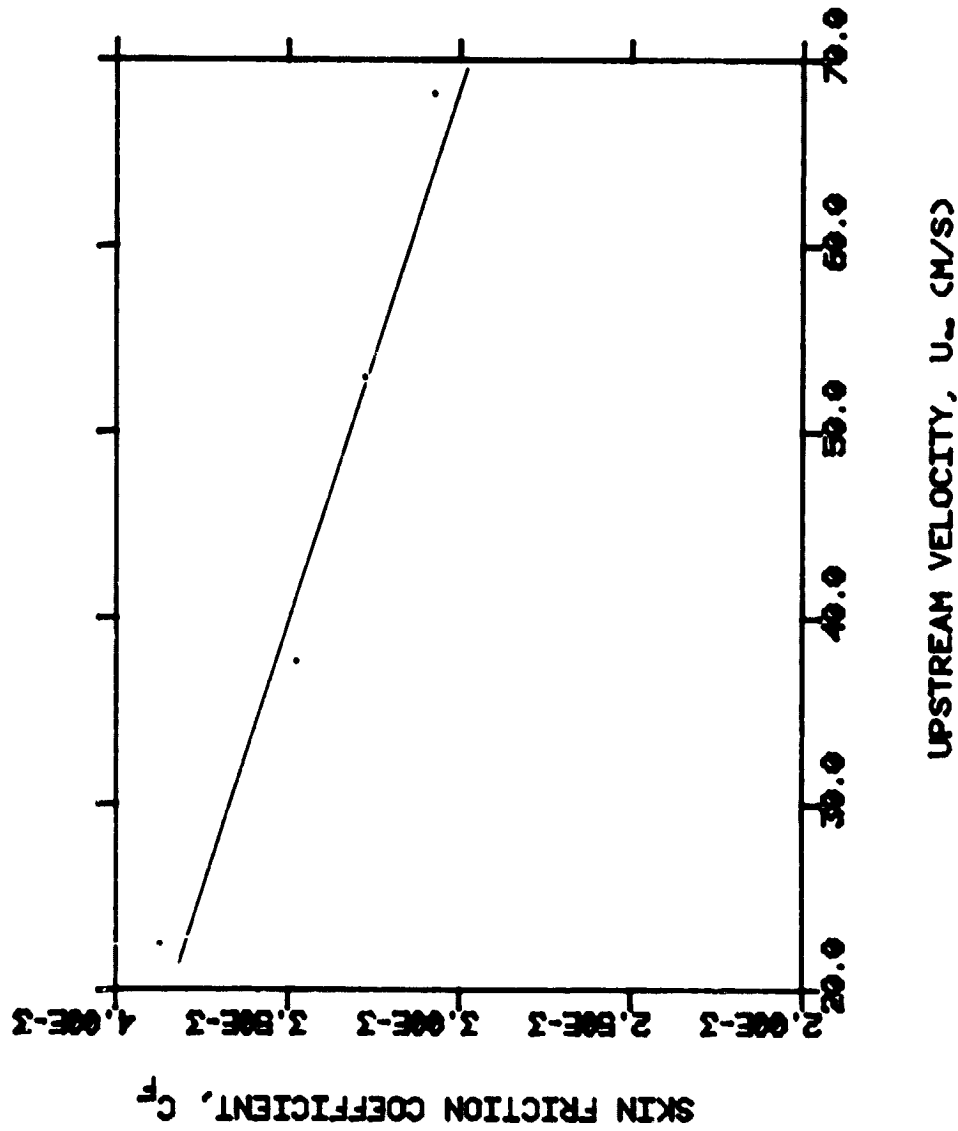


Figure 11.30 Skin friction coefficient, c_f , versus upstream velocity, U_∞ , from Preston tube measurements at 22.86 cm from trailing-edge on airfoil centerline with airfoil at 0° angle-of-attack.

11.3 Sound Power Law for a 0.9525 cm Diameter Rod

A 0.9525 cm diameter rod was immersed in the potential core (laminar region) of the rectangular jet in place of the airfoil. The resulting power law determination gave a $U_{\infty}^{6.0}$ relationship between the mean-square sound pressure and the upstream velocity U_{∞} as shown. This result closely follows the 6.0 power law prediction of the Curle⁶ theory for such limited-extent bodies as the rod. This close agreement between experiment and theory provides a calibration check on the accuracy of similar procedures for the airfoil case.

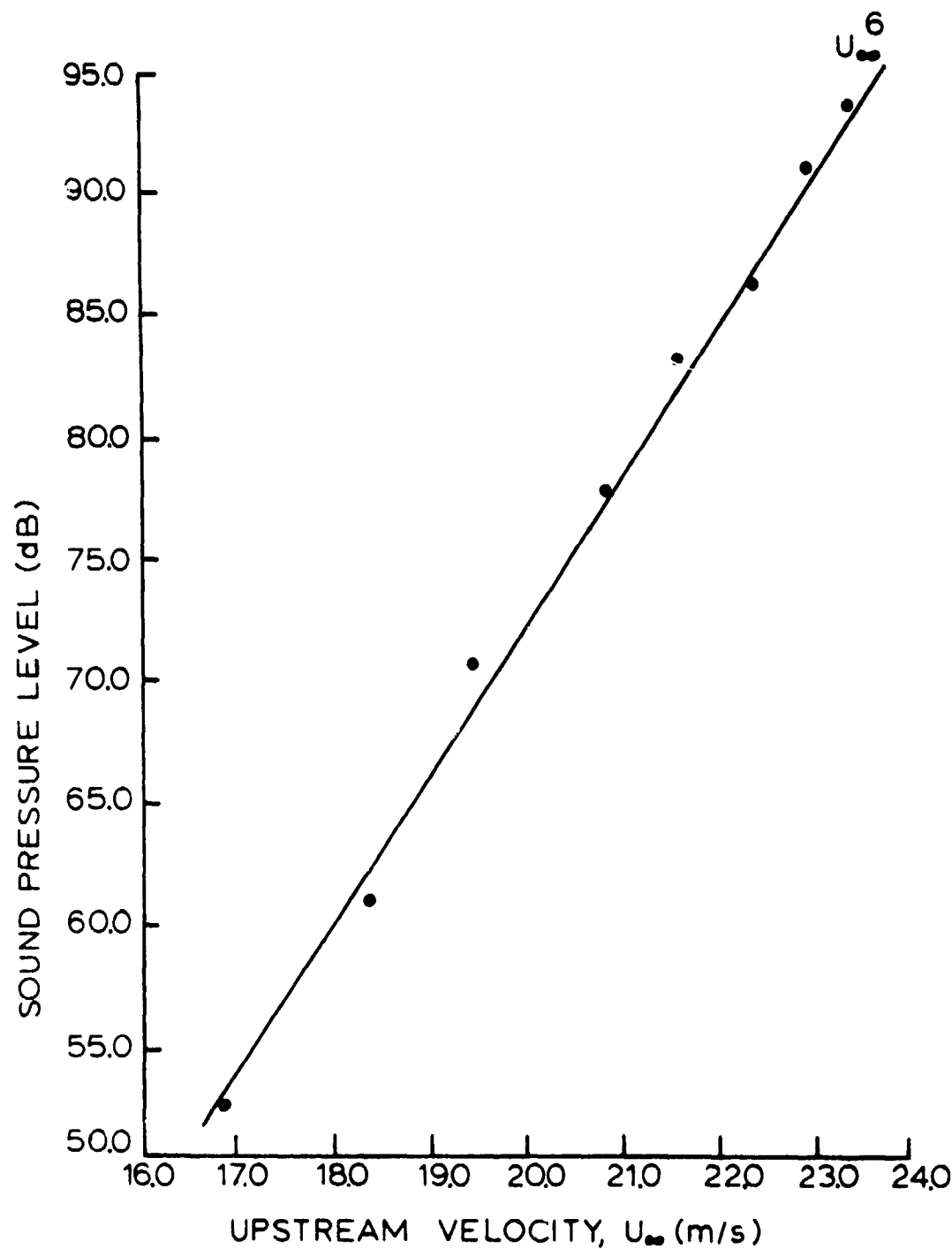


Figure 11.31 Variation in the overall sound pressure level (SPL) with upstream velocity, U_{∞} , for a 0.9525 cm diameter rod.